

UNIVERSIDADE DE LISBOA  
FACULDADE DE CIÊNCIAS  
DEPARTAMENTO DE FÍSICA



**Ciências**  
**ULisboa**

## **Integration of 3D printed sensors into orthotic devices**

Cláudia Teixeira Espadinha

**Mestrado Integrado em Engenharia Biomédica e Biofísica**  
Perfil em Engenharia Clínica e Instrumentação Médica

Dissertação orientada por:  
Professor Bram Vanderborght  
Professor Hugo Alexandre Ferreira

2020

# ACKNOWLEDGMENTS

Firstly, I want to thank you, professor Bram Vanderborcht for the opportunity you gave me by accepting me into your research group and for all the support during the whole year I spend there, I am really grateful for that.

Also, I would like to thank you, Kevin Langlois, for all the help you gave me through all this process. For always being available for any question, any advice or even for just a simple talk, without you, this report would not be possible, so thank you. Furthermore, I would like to thank all the people from the lab for the fantastic support, for all the conversations and laughs during lunchtime, or the daily “coffee train” that always made my day better.

Queria também agradecer ao programa ERASMUS+ pela oportunidade concedida, através do apoio financeiro imprescindível para a realização deste projeto.

Um especial agradecimento ao meu orientador, professor Hugo Ferreira pelo apoio e disponibilidade durante todo este processo, não só durante este último ano, mas durante todo o meu percurso académico.

E porque um percurso académico é muito mais do que estudos, queria deixar um especial agradecimento aos meus grandes amigos da faculdade, os meus “primeiro estranha-se, depois entranha-se”, obrigada pela companhia, apoio e motivação, obrigada por todos os risos e brincadeiras que tornaram tudo isto muito mais fácil. Deixo também um especial agradecimento à minha “colega de casa” e aos meus “dois terços”, sem vocês nada disto teria sido possível.

Para finalizar, não podia deixar de agradecer o apoio incondicional de toda a minha família, em especial aos meus pais por me terem sempre apoiado, por serem sempre o exemplo que eu tendo a seguir e por terem tornado todo este processo possível. À minha irmã, por ter sempre sido o extremo oposto que tende a balançar todas as minhas importantes decisões de vida e que, à sua maneira, sempre me apoiou. Queria também deixar um especial agradecimento à Titi, por toda a ajuda fornecida nestes últimos meses (para além do incondicional e constante apoio), que foi imprescindível para o término deste projeto.



# ABSTRACT

There has been an increasing interest on the research of exoskeletons in the last years, with novel designs and concepts emerging to develop the next generation of devices. One of many research areas, involved in the optimization of the exoskeletons' performance, is the integration of sensors, more specifically Electromyography (EMG) sensors and force sensors, into the exoskeleton's interfaces, being the interfaces, the exoskeleton's component responsible for the power transmission from the exoskeleton to the user's biological structures. The integration of sensors into the exoskeletons' interfaces can potentially improve the exoskeleton's control, comfort, safety, and ergonomics.

However, the integration of the sensors that are currently on the market into the exoskeletons' interfaces has complications such as the sensors' fixed geometry, lack of customisation and fabrication costs. One alternative to these conventional sensors is combining the 3D printing technology to the sensor's world and produce 3D printed orthosis embedded with 3D printed sensors, where an integrated manufacturing strategy can be adopted, allowing the production of customized interfaces.

Therefore, the goal of this project was to develop and test 3D printed EMG and force sensors to be integrated, in future work, into the cuffs of 3D printed orthotic devices. To help the design of these orthotic devices, an analysis of the deformation of the lower limb muscles, during the gait cycle will was also performed.

In this project a working 3D printed EMG sensor, along with a 3D printed capacitance-based force sensor were successfully produced, also an efficient reading system for the force sensor was developed. Besides the 3D printed sensors, an algorithm, able to detect possible deformations, and measure those same deformations, was developed. From the algorithm's results, it was possible to conclude the existence of variations in the muscle's limits due to changes in the gait cycle positions.

**Keywords:** 3D printing; EMG sensors; Capacitive sensors; Exoskeletons; lower limb muscles' deformation;



# RESUMO

Nos últimos anos tem-se vindo a registar um aumento do interesse, por parte da comunidade científica, pela área dos exosqueletos, onde novos modelos e conceitos são constantemente apresentados, com o objetivo de desenvolver a próxima geração de dispositivos. Uma das razões que pode vir a justificar este aumento de interesse, por parte da comunidade científica, é o aumento da esperança média de vida.

De acordo com a organização mundial de saúde, a percentagem de população mundial com mais de 60 anos aumentará de 11% para 22%, entre 2000 e 2050. Com o aumento da esperança média de vida, espera-se também um aumento da incidência de doenças associadas ao envelhecimento que, em muitos dos casos, podem levar a incapacidades motoras. Como tal, é necessário desenvolver dispositivos capazes de assistir indivíduos que se encontrem nestas situações. Uma possível medida a implementar, seria o desenvolvimento de exosqueletos dedicados à reabilitação, assim como dispositivos capazes de assistir indivíduos com deficiências locomotoras, no seu dia-a-dia.

Com a perspetiva do aumento da esperança média de vida, é também importante adotar medidas de prevenção, de modo a evitar complicações no futuro, ao nível do sistema locomotor, especialmente para pessoas com trabalhos mais físicos. Estas complicações poderiam ser potencialmente reduzidas com a aplicação de exosqueletos nos variados locais de trabalho, com vista a melhorar a postura e desempenho dos trabalhadores, auxiliando-os nas suas tarefas diárias.

Independentemente do objetivo para qual o exosqueleto está a ser desenvolvido, é essencial que o mesmo tenha uma boa estratégia de controlo. Existem várias estratégias de controlo, sendo uma delas o controlo baseado na força/torque aplicado pelo utilizador. Neste tipo de controlo, como o nome indica, a força/torque aplicado pelo exosqueleto é proporcional à leitura de sensores que se encontram entre o utilizador e o exosqueleto, que indiretamente interpretam a intenção do utilizador. Estes sensores são normalmente sensores de eletromiografia (EMG) e/ou sensores de força.

Para além de uma boa estratégia de controlo é também importante monitorizar as forças de interação entre o exosqueleto e o utilizador. A incorreta aplicação de forças, por parte do exosqueleto, pode levar à alteração do padrão natural de ativação dos músculos, sendo por sua vez contraproduativo no caso da fisioterapia, por exemplo. Por outro lado, forças que são incorretamente aplicadas podem também desencadear fadiga, desconforto e, em último caso, colocar em risco a segurança do utilizador. Como tal, a monitorização das forças aplicadas pelo exosqueleto é algo verdadeiramente importante, que pode ser executado através da implementação de sensores de força.

A partir da informação apresentada, é possível concluir que a integração de sensores de EMG e força nas interfaces dos exosqueletos é uma possível estratégia a adaptar, quando o objetivo é otimizar o desempenho dos mesmos. No entanto, não existem muitos casos de exosqueletos com este tipo de sensores incorporados. Uma das razões que pode vir a justificar este fenómeno é a geometria deste tipo de sensores, que se encontram atualmente no mercado, ser fixa e de difícil customização, o que influencia diretamente o design do exosqueleto. Para além da geometria dos sensores, na maioria dos casos, quando o objetivo é fabricar sensores de alta resolução, o processo de fabrico é constituído por múltiplas etapas, o que pode dificultar a escalabilidade de manufatura, aumentando o custo de fabrico, o que em última instância comprometerá o design e o processo de fabricação dos exosqueletos.

Com o objetivo de encontrar alternativas aos sensores convencionais, alguns desenvolvimentos têm sido feitos numa tentativa de incorporar a tecnologia de impressão 3D ao mundo dos sensores. Uma

das grandes vantagens desta simbiose é a possibilidade de poder, numa só etapa, produzir e integrar o sensor, sem limitações de design, no local desejado, neste caso na interface do exosqueleto.

Como tal, o objetivo deste trabalho seria o desenvolvimento de uma interface de um exosqueleto, impressa em 3D, com sensores de EMG e de força incorporados, também impressos em 3D. O exosqueleto que será utilizado provirá de um projeto em desenvolvimento pelo grupo Brussels Human Robotics Research Center, BruBotics, mais especificamente pelo projeto BioMot.

Neste projeto em específico, devido à complexidade do objetivo estipulado, apenas os sensores de EMG e de força, impressos em 3D, foram desenvolvidos e testados. Para além dos sensores, um estudo sobre a deformação dos músculos da parte inferior da perna, durante ciclo de marcha, foi também realizado, de modo a facilitar o futuro design da interface do exosqueleto.

Um sensor de EMG é constituído por dois eléctrodos condutores, isolados por um material não condutor, de modo a possibilitar a captação dos sinais eléctricos provenientes dos músculos, que, por sua vez, refletem a intenção do utilizador. Como tal, para produzir este tipo de sensores, utilizando técnicas de impressão 3D, mais especificamente, técnicas de impressão FDM (modelagem por deposição fundida), é preciso: um material condutor (neste caso semicondutores, devido à inexistência de filamentos condutores, para este tipo de impressão 3D) e um material não condutor. Para este projeto foram utilizados: o filamento semicondutor Proto-pasta conductive PLA (Protoplant, Inc., USA) e o filamento não-condutor Ultimaker TPU 95A (Ultimaker B.V., The Netherlands).

Com estes dois materiais foi possível, com algumas limitações, produzir um sensor EMG funcional, que poderá, possivelmente, vir a ser integrado num exosqueleto, em trabalho futuro. É necessário, no entanto realizar primeiro um estudo intensivo, de modo a compreender as restrições de funcionamento deste mesmo sensor.

Relativamente aos sensores de força, o seu design/modo de funcionamento, foi baseado num condensador de eléctrodos paralelos. De forma a produzir este tipo de sensor, é necessário um material semicondutor (dado, mais uma vez, a inexistência de materiais condutores para o tipo de técnica de impressão 3D que será utilizado) e um material não condutor. A ideia seria imprimir um sensor com duas finas placas semicondutoras, separadas por outra fina placa não condutora, denominado de dieléctrico.

Neste tipo de sensores, quando uma força é aplicada, a distância entre as placas semicondutoras diminui, induzindo um aumento da capacidade do condensador, sendo que este aumento será proporcional à força aplicada ao sensor, permitindo assim o seu registo. Com o objetivo de desenvolver este tipo de sensor, foi necessário primeiro desenvolver um sistema capaz de captar, e posteriormente transferir para um computador, as variações da capacidade do sensor de forma a possibilitar a sua posterior análise.

Para além do sistema de registo, foi também necessário testar vários tipos de materiais e as várias definições de impressão, de modo a seleccionar quais os mais adequados para a impressão deste sensor, dado que. Neste caso, os materiais e as definições de impressão mais adequadas, seriam as que conferissem ao dieléctrico a maior flexibilidade possível dado que, quanto maior a flexibilidade do dieléctrico, maior a variação da capacidade, e, como tal, maior resolução dos sinais captados.

Após o desenvolvimento de um sistema de registo, e da escolha dos materiais mais adequados ao objetivo deste projeto, um sensor capacitivo foi produzido. As placas condutoras foram impressas com o filamento PI-ETPU 95-250 Carbon Black (Palmiga Innovation, Sweden) e o dieléctrico com o filamento não condutor NinjaFlex 85A (Fenner Inc., USA). Ao contrário das placas condutoras, o dieléctrico foi impresso com um preenchimento concêntrico ocupando apenas 50% do espaço, conferindo deste modo uma maior flexibilidade ao sensor.

Com a produção do sensor completa, o mesmo foi testado. A partir dos resultados dos testes realizados, foi possível verificar um aumento da capacidade do sensor quando sujeito à aplicação de uma força, sendo que este aumento foi proporcional à magnitude da força aplicada. Apesar dos resultados terem sido bastante positivos, o sensor demonstrou ter uma elevada histerese, como tal, antes da implementação destes sensores em exosqueletos, os mesmos terão de ser rigorosamente testados, com vista a melhor compreender as suas limitações e modular, se possível, a resposta dos sensores tendo em conta a sua histerese, dependência do tempo de aplicação das forças, entre outros fatores.

Após o desenvolvimento dos dois tipos de sensores, foi crucial compreender qual o melhor local para os aplicar, de modo a otimizar a informação proveniente dos sinais, por eles captados. Seguindo esta ordem de pensamentos, um algoritmo foi desenvolvido de modo a melhor compreender a deformação da superfície da parte inferior da perna, e como tal dos músculos que a constituem, durante o ciclo de marcha. Esta informação é especialmente relevante aquando da implementação dos sensores de EMG, dado que os locais onde os mesmos devem ser colocados, correspondem à zona mais proeminente dos músculos que estão a ser avaliados, que naturalmente estão sujeitos a maiores níveis de deformação.

Para compreender quais os vários locais de deformação da parte inferior da perna, vários varrimentos de imagem (*scans*) de vários indivíduos, em várias fases do ciclo de marcha, foram obtidos, e comparados entre si, através do algoritmo desenvolvido, nestes *scans* as partes mais proeminentes dos músculos em estudo foram assinaladas com marcadores. O algoritmo desenvolvido tem a capacidade de identificar, com algum erro associado, os marcadores, alinhar os diversos *scans* das várias fases do ciclo de marcha, com base na localização espacial desses mesmos marcadores e segmentar transversalmente os *scans*, nas zonas mais proeminentes dos músculos. A análise da deformação é feita a partir do raio de curvatura deste segmento em zonas específicas previamente estipuladas.

Apesar do algoritmo precisar de alguns melhoramentos, de forma a possibilitar uma avaliação pormenorizada e exata da deformação da superfície da parte inferior da perna, foi possível concluir, a partir dos resultados de saída do algoritmo, que as maiores deformações ocorrem nos limites dos músculos e não nas zonas mais proeminentes dos músculos (apesar de existir um deslocamento espacial das mesmas zonas). Esta informação será bastante relevante para a construção da interface do exosqueleto, mais especificamente para a escolha dos materiais, mais rígidos ou mais flexíveis por exemplo, e onde os corretamente colocar, de modo a assegurar o constante contacto entre o utilizador e os sensores, enquanto a eficiência do exosqueleto é assegurada.

**Palavras-chave:** Impressão 3D; Sensores de EMG; Sensores capacitivos; Exosqueletos; Deformação dos músculos da parte inferior perna



# TABLE OF CONTENTS

ABSTRACT.....	v
RESUMO.....	vii
TABLE OF CONTENTS.....	xi
LIST OF TABLES.....	xvii
LIST OF ABBREVIATIONS.....	xix
Chapter 1 INTRODUCTION.....	1
1.1 Motivation.....	1
1.2 Exoskeletons.....	2
1.2.1 Key features to design an efficient exoskeleton.....	3
1.2.2 Exoskeleton’s control.....	5
1.3 Sensors.....	5
1.3.1 Electromyography sensors.....	6
1.3.2 Force and strain sensors.....	9
1.4 3D Printing methods.....	11
1.5 Examples of 3D printed sensors.....	12
1.5.1 3D printed capacitive sensors.....	12
1.5.2 3D printed resistive sensors.....	13
1.5.3 3D printed EMG sensors.....	14
1.6 Exoskeleton’s cuff design.....	15
1.6.1 Determination of the type of sensor to incorporate into the exoskeleton’s cuff.....	15
1.6.2 Integration of the 3D printed sensors into the exoskeleton’s cuff.....	16
1.7 Project framework.....	18
1.8 Aim.....	19
1.9 Outline.....	19
Chapter 2 Development of 3D printed EMG sensors.....	21
2.1 Experimental Protocol.....	21
2.1.1 Materials.....	21
2.1.2 Placement of the electrodes.....	23
2.1.3 Data collection.....	23
2.1.4 EMG analysis.....	24
2.2 Experimental Results.....	25
2.3 Conclusion.....	29
Chapter 3 Development of 3D printed force sensors.....	31

3.1 Development of the sensor's reading system.....	31
3.1.1 Experimental Protocol.....	33
3.1.2 Results.....	34
3.1.3 Conclusion .....	36
3.2 Construction of the 3D printed sensor .....	37
3.2.1 Assessment of non-conductive 3D printing filaments to be used as dielectric .....	38
3.2.2 Conclusion .....	43
3.3 Test the 3D printed sensor with the developed reading system .....	43
3.3.1 Experimental Protocol.....	43
3.3.2 Results.....	45
3.3.3 Conclusion .....	47
3.4 Additional tests .....	48
3.5 Final conclusions and Future work .....	48
Chapter 4 Study of the deformation of the lower Limb muscles .....	51
4.1 Experimental Protocol.....	51
4.1.1 Materials.....	51
4.1.2 Data Collection .....	52
4.1.3 Scan's treatment.....	53
4.1.4 Markers' Identification algorithm .....	54
4.1.5 Alignment of the scans.....	60
4.1.6 Segmentation of the lower limb .....	64
4.1.7 Data Analysis .....	66
4.2 Results.....	68
4.3 Conclusion .....	73
Chapter 5 Conclusion and Future Work.....	75
Chapter 6 Bibliography.....	77

# LIST OF FIGURES

Figure 1.1: Examples of the several types of exoskeletons (a) EksoVest [5]; (b) ReWalk exoskeleton [6] ; (c) Lokomat [12] .....	3
Figure 1.2: A myoelectric control system based on pattern recognition [35] .....	8
Figure 1.3: Representation of the effect of pressure-like and shear forces into a flexible material .....	9
Figure 1.4: Schematic representation of a capacitor with parallel electrodes, the darker parts represent the two conductive plates and the lighter part the dielectric. ....	9
Figure 1.5: (a) capacitive sensor, (b) sensor based on the intrinsic piezoresistivity properties of the material, (c) sensor based on contact resistance modulation, (d) piezoelectric/triboelectric sensor. [25].....	10
Figure 1.6: Examples of 3D printed capacitive sensors (a) M. Schouten et al.’s sensor [47]; (b) S. J. Leigh et al.’s sensor [48]; (c) P. Laszczak et al.’s sensor [53].....	13
Figure 1.7: Examples of 3D printed resistive sensors (a) S. J. Leigh et al.’s sensor [48]; (b) B. Shih et al.’s sensor [54]; (c) S. Harada et al.’s sensor [55] .....	14
Figure 1.8: G. Wolterink, R. Sanders, and G. Krijnen 3D-printed sEMG sensor [44].....	14
Figure 1.9: Position of the legs during a single gait cycle from right heel contact to right heel contact [58].....	17
Figure 1.10: (a) The entire structure of the BioMot gait exoskeleton [64]. (b) Customized physical interface attached to the ankle foot model of the FP7 BioMot exoskeleton [14]. (c) 3D printed, customized interface made with PLA and reinforced with a carbon fiber and epoxy resin composite [14].....	18
Figure 2.1 (a) CAD design of the 3D printed EMG sensor and respective measurements (b) 3D printed EMG sensor .....	22
Figure 2.2: (a) Representation of the exact location where the EMG electrodes should be placed (yellow cross) [65] (b) Representation of the arm muscles [30] .....	23
Figure 2.3: MNF calculations for EMG records corresponding to different levels of contractions, induced by the support of different weights, 1kg, 2kg and 3kg. The MNF values represented in blue correspond to the measures performed with the commercial EMG sensors and the MNF values represented in orange to the measures performed with the 3D printed EMG sensors. ...	26
Figure 2.4: MDF calculations for EMG records corresponding to different levels of contractions, induced by the support of different weights, 1kg, 2kg and 3kg. The MDF values represented in blue correspond to the measures performed with the commercial EMG sensors and the MDF values represented in orange to the measures performed with the 3D printed EMG sensors. ...	26
Figure 2.5: RMS mean calculations for EMG records corresponding to different levels of contractions, induced by the support of different weights, 1kg, 2kg and 3kg, and by the MVC. The RMS values represented in blue correspond to the measures performed with the commercial EMG sensors and the RMS values represented in orange to the measures performed with the 3D printed EMG sensors. ....	28
Figure 3.1: Resistor in series with a capacitor.....	32
Figure 3.2: Electronic system responsible for connecting the sensor to the reading system.....	33

Figure 3.3: Representation of the mean charging time values in respect to the capacitor's capacitance in conjugation with the linear tendency of the values .....	35
Figure 3.4: (a) Top view of the 3D printed sensor, (b) side view of the 3D printed sensor, (c) representation of the 3D printed sensor .....	38
Figure 3.5: Capacitance-based sensor with Ultimaker TPU 95A as dielectric.....	39
Figure 3.6: Capacitance-based sensor with silicone as dielectric.....	40
Figure 3.7: Capacitance-based sensor with NinjaFlex 85A as dielectric. (a) Capacitive sensor with 50% cross 3D dielectric's infill. (b) Capacitive sensor with 50% gyroid dielectric's infill. (c) Capacitive sensor with 50% concentric dielectric's infill. (d) Capacitive sensor with 30% concentric dielectric's infill. ....	42
Figure 3.8: Filtered signal with a lowpass, 2nd order butterworth filter with a cut off frequency of 0.06Hz. (a) Signal from the first experiment. (b) Signal from the second experiment. (c) Signal from the third experiment. ....	46
Figure 4.1 Markers' ideal locations, for subject number 4, each marker has its respective label. (a) Anterior view (b) Posterior view.....	53
Figure 4.2: (a) Scan, from subject number one, imported to Autodesk Meshmixer program. (b) Scan, from subject number one, after the "cleaning", in the Autodesk Meshmixer program. (c) Scan results, from subject number one, after resizing the scan's mesh in the ZBrush 2019 program. ....	54
Figure 4.3: Vertices' representation of the STL file, from subject number one.....	54
Figure 4.4: (a) One of the defined segments of the scan from subject number one, (b) Schematic of the organization of the vertices, in one segment, in a counter clockwise direction. ....	55
Figure 4.5: (a) Distance of every vertex to the centroid of the segment they belong, after filtering, from a scan, the orange spots correspond to possible markers that were identified by the first identification method. (b) and (c) Identified markers of a part of the scan, from subject number one.....	57
Figure 4.6: (a) Schematics of the second angle. (b) Identified markers of a part of the scan, from subject number one. The blue dots correspond to the markers identified by the first identification method and the orange dots the markers identified by the second identification method. ....	58
Figure 4.7: (a) Schematics of the fundamentals the third identification method is based on. (b) and (c) Results of the application of the third identification method, being the blue spots, the vertices identified as possible markers (scan from subject number one). ....	59
Figure 4.8: (a) Schematics of the fundamentals the fourth identification method is based on. (b) and (c) Results of the application of the fourth identification method, being the blue spots, the vertices identified as possible markers (scans from subject number one).....	59
Figure 4.9: Representation of a plane formed by the three tibia markers and respective normal vector (scan from subject number one).....	61
Figure 4.10: Schematic of the rotation angle, $\theta$ .....	63
Figure 4.11: Schematic of the rotation angle, $\gamma$ .....	64
Figure 4.12: a) Example of the result of the disproportion between the scans of the same subject in the three different positions (segments from the scans of subject 1). b); c) and d) Example of the	

result of the misalignment of the scans with the z-axis (segments from the scans of subject 2). .....	66
Figure 4.13: Schematics of the algorithm used to identify potential deformation locations (scan from subject 1).....	67
Figure 4.14: Example of the deformations that are going to be analysed (segments from the scans of subject 2).....	68
Figure 4.15: Segments at the lateral gastrocnemius markers' height from the different gait cycle phases. The yellow dots correspond to the zeros of the 1 <sup>st</sup> derivative function and the red ones to the zeros of the 2 <sup>nd</sup> derivative function. a); b) and c) segments from the scans of subject 1.d); e) and f) segments from the scans of subject 2. g); h) and i) segments from the scans of subject 3. j); l) and m) segments from the scans of subject 4.....	69
Figure 4.16: Segments at the three markers' height from the three different gait cycle phases ( the blue segments corresponds to the mid stance phase, the orange segments to the heel off position and the yellow ones to the heel strike position). The blue dots correspond to the zeros from the 1 <sup>st</sup> derivative of the heel strike position distances' function, the greens to the zeros from the 1 <sup>st</sup> derivative of the heel off position distances' function and the purples to the zeros from the 1 <sup>st</sup> derivative of the mid stance position distances' function (the segments were aligned by the respective centroids). a); b) and c) segments from the scans of subject 1.d); e) and f) segments from the scans of subject 2. g); h) and i) segments from the scans of subject 3. j); l) and m) segments from the scans of subject 4.....	70



# LIST OF TABLES

Table 2.1: Comparison between the main characteristics of the capacitance-based and resistance-based force sensors. The values in green represent the desirable behaviour to the respective characteristics and the orange the opposite. ....	16
Table 3.1: Printing settings, used to print the 3D printed EMG sensor.....	22
Table 3.2: Linearization of the MNF and MDF values calculated for the EMG recording of the second experiment.....	27
Table 4.1: Measurement of the parameters. ....	34
Table 4.2: Experimental results for the capacitance.....	36
Table 4.3: Mechanical properties of Ultimaker TPU 95A .....	39
Table 4.4: Mechanical properties of NinjaFlex 85A.....	40
Table 4.5: Mechanical properties of REC RUBBER .....	41
Table 4.6: Comparison between the old printing settings, used to print the previous sensors, with the new printing settings, also the printing settings used to print the two conductive electrodes... ..	42
Table 4.7: Printing settings to 3D print the capacitance-based force sensor .....	44
Table 4.8: Weight's measurement.....	45
Table 4.9: Mean capacitance in each stage of the experiment .....	47
Table 4.10 - Relative difference, in percentage, between the 1 <sup>st</sup> stage and the other stages. The results in this table are colorized according to their value in comparison to all the other values in the table. The colour blue corresponds to the lowest values and the colour red to the highest values. ....	47
Table 4.11 - Mean capacitance in each stage of the experiment, calculated by the equation presented in figure 4 obtained in the calculus section of the set up development experiment.....	47
Table 5.1 Radius of curvature of the location where the three chosen deformation were. For every segment, the p-value from the Kruskal-Wallis test is presented. For every subject nine segments were analysed, three for each gait cycle position, and three for each marker. The results in this table are colorized according to their value in comparison to all the other values in the table. The colour red corresponds to the lowest values and the colour green to the highest values. ....	71
Table 5.2: Results from the multiple comparison test (at a level of significant of 10%). The values in green represent the populations that present values significantly different from each other, the values in orange represent the opposite. ....	72



# LIST OF ABBREVIATIONS

- ARV** - Average rectified value
- CNS** - Central nervous system
- DLP** - Digital light processing
- EBM** - Electronic beam melting
- EMG** - Electromyography
- FA-I** - Fast adapting receptors type I
- FA-II** - Fast adapting receptors type II
- FDM** - Fused deposition modelling
- LGD** - Lateral Gastrocnemius Down
- LGU** - Lateral Gastrocnemius Up
- LOM** - Laminating object manufacturing
- MDF** - Median frequency
- MGD** - Medial Gastrocnemius Down
- MGU** - Medial Gastrocnemius Up
- MNF** - Mean frequency
- MVC** - Maximal voluntary contraction
- PDT** - Pain detection threshold
- PLA** - Polylactic Acid
- PNS** - Peripheral nervous system
- PTT** - Pain tolerance threshold
- RMS** - Root mean square
- SA-I** - Slow adapting receptors type I
- SA-II** - Slow adapting receptors type II
- SENIAM** - surface ElectroMyoGraphy for the Non-Invasive Assessment of Muscles
- SLA** - Stereolithography
- SLS** - Selective laser sintering
- SLM** - Selective laser melting
- TD** - Tibia Down
- TES** - Triboelectric sensor
- TiD** - Tibialis Anterior Down
- TiU** - Tibialis Anterior Up

**TM** - Tibia Middle

**TPU** - Thermoplastic poly-urethane

**TU** - Tibia Up

**u.m** - units of measure

# Chapter 1

## INTRODUCTION

### 1.1 Motivation

Since the beginning of times, the human species has struggled to conform to the universal truth that life is time-limited. Some may say that the important discoveries have been especially driven by times of war, in order to gain an edge over the enemy, however, another source of motivation, behind some of the most important breakthroughs is the constant thought of “how to cheat death?”, “How to gain time from a life that is time-limited?”. With these questions in mind, the world has been evolving, vaccination, anaesthesia, medical imaging, are just some examples of, how the human species, in some extend, was able to indeed cheat death, and live longer.

However, an important question rises with the increase of the average life expectancy, “Is it worth to live longer, if your physical and mental skills can no longer keep up with the ageing process?”. With this idea in mind, scientists all over the world have been investigating solutions to fight the degeneration of the physical and mental capabilities, associated with ageing, making the extra lived years, worth living.

One of the research fields, most concerned with maintaining the humans’ physical skills through the ageing process, is the exoskeleton’s research field, which has been registering an increasing interest, in the latest years, with novel designs and concepts emerging to develop the next generation of devices. These types of robots are able to assist people with motor disabilities, in a perpetual or in a therapeutic way. It is important to mention that nowadays, in a larger number of cases, the motor disabilities are generated by diseases associated with ageing, as strokes and diabetes, being just some examples.

Also, due to the increase of the average life expectancy, it is also important to adopt preventive measures to avoid diseases related to motor disabilities in the latest years of life, especially for people with more physical jobs. These issues could be potentially alleviated by the use of human augmentation devices [1], which, as well, is one of the main focus on the exoskeletons’ research field.

Although this is a research field in expansion, some specific departments still have a long way to go. One of these departments, in need of a great development, is the exoskeletons’ controllers department since it is in the controllers that the users’ intention, along with the interaction forces between the exoskeleton and the user are registered, and used to mimic the users’ motion intentions, in a comfortable, safe and ergonomic way.

There are several control strategies, possible to use to control the exoskeletons. One type of control strategy, that shows real promises, is the direct force (or torque) based control strategy. In this type of control strategy, the force/torque applied by the exoskeleton is proportional to the readings of the sensors that are incorporated into the exoskeletons, these sensors can be electromyography (EMG)

sensors, or force sensors that are placed in between the user and the exoskeletons, it can also be a combination of the two [1].

However, although the integration of EMG and force sensors, into the exoskeletons' interface, is a step towards the optimisation of the exoskeleton's performance, there are few cases of exoskeletons with this type of sensors incorporated. One of the reasons for this phenomenon is the fixed geometry and lack of customisation of the sensors that are currently on the market, which influences the exoskeleton's design. Also, in most cases, the fabrication process of this type of sensors has too many steps (time-consuming), which leads to a lack of manufacturing scalability and an increase of the fabrication costs, when the goal is to achieve high-resolution structures [2], which will, ultimately, compromise the design and fabrication process of the exoskeletons.

Therefore, to achieve the final goal of having an exoskeleton mimicking the user's motion intentions, in a comfortable way, it is necessary first to investigate and develop better solutions to replace the sensors that are nowadays being produced and commercialized.

In an attempt to find some alternatives to the conventional sensors, there has been an increase interest in research towards the 3D printing technology, since it allows a fully integrated manufacturing strategy with a customized interface, creating the opportunity to develop better physical interfaces. Also, with the application of this new technique, a whole new set of research opportunities, will also appear.

With all the presented information in mind, the goal of this project is to develop 3D printed EMG and force sensors that can be incorporated into the exoskeletons' interfaces, also a study on the deformation of the lower limb muscles, during the gait cycle will be performed, to help redesign the exoskeletons' cuff, since a customised interface, can also be one possible path to achieve the optimization of the exoskeletons' performance.

## **1.2 Exoskeletons**

H. Kawamoto and Y. Sankai define exoskeletons as an external structure which covers the human body parts and has joint parts corresponding to those of the human body [3].

Depending on the exoskeletons' main application purpose, it is possible to divide them into three different categories: exoskeletons for human performance augmentation, assistive devices for individuals with disabilities and therapeutic exoskeletons for rehabilitation [1].

The exoskeletons for human performance augmentation, are meant to be applied to healthy individuals, with the purpose of increasing their physical capabilities like endurance or strength. They are specifically meant to be applied in construction sites, warehouses, emergency relief operations or even military bases and excursions where lifting heavy objects/tools or carry heavy loads over vast distances is an essential part of the job [1], [4]. One example of this type of exoskeletons is the EksoVest [5], represented on Figure 1.1 example a.

The other two types of exoskeletons are supposed to be applied to individuals with specific needs. In some situations, the individuals suffer from neurological or musculature disorders like strokes or spinal cord injuries, that can lead to motor impairments affecting, permanently or not, the ability to walk or perform some specific movements. In these situations, the assistive devices for individuals with disabilities allow the users to complete movements they could not complete on their own [1], [4]. One example of a device used by spinal cord injury patients is the ReWalk exoskeleton [6], shown in Figure 1.1, example b.

The last type of exoskeletons are the therapeutic exoskeletons for rehabilitation. R. R. Fabrizio Margheritini *et al.* defines the purpose of rehabilitation as the possibility to bring back the patient's physical, sensory, and mental capabilities that were lost due to injury, illness, and disease, and support the patients to compensate for deficits that cannot be treated medically [7]. Usually, rehabilitation is performed by a specialized therapist and depending on the patient and on his type of injury, the rehabilitation procedure can take up to several months, with daily sessions. This leads to very expensive therapy costs [8] and also, because the therapy relies mainly on the therapist's experience, it is really difficult to achieve the required repetition and high-intensity training every time [9].

The application of robots into rehabilitation could replace the physical training efforts of the therapists, allowing a more intensive repetitive motion with better control over the introduced forces, required for the different exercises, which will, ultimately, decrease the therapy costs while increasing its efficiency [10], [11].

Depending on the purpose of the applied exercise and the stage of rehabilitation, the therapeutic exoskeletons for rehabilitation can assist, resist or perturb the user's movements [1]. Lokomat [12] is one example of a therapeutic exoskeleton for rehabilitation present on the market (Figure 1.1, example c).



Figure 1.1: Examples of the several types of exoskeletons (a) EksoVest [5]; (b) ReWalk exoskeleton [6] ; (c) Lokomat [12]

### ***1.2.1 Key features to design an efficient exoskeleton***

When designing an exoskeleton, it is important to have some aspects in consideration: the autonomy of the energy supply, the safety and wearability of the exoskeleton and its interaction with the user [13].

#### ***Power supply***

The exoskeletons' power supply is considered to be one of the main complications when designing portable exoskeletons, since the energy required by the exoskeleton to properly function is proportional to its weight. Increasing the weight of the exoskeletons leads to a decrease on the overall functionality [1], so it is important to have the exoskeletons' structure, as well as the actuators and the controllers as light as possible [13].

Furthermore, the energy generated by the power supply is not transmitted in its totality by the exoskeleton to the user, for example, the mechanical power lost associated to soft tissue compression and hardness compliance of the physical interfaces can rise to 50% [14], [15]. Thus it is imperative,

when designing exoskeletons' interfaces, to have these aspects in consideration, in order to optimize the exoskeletons' efficiency.

One potential strategy to adopt to mitigate the power transmission's problem is to increase the interfaces' stiffness and to design them to interact with bony prominences of the body, instead of soft tissues [14].

An example of a scientific research being developed towards this direction is the work produced by K. Langlois *et al.*. In their research, a customised interface, based on a 3D scan of a healthy individual, 3D printed in polylactic acid, PLA, and reinforced with carbon fibres was developed and tested, the results revealed a positive outcome regarding the reduction of the relative motion between the interface and, in this case, the limb of the tested subject, when compared to a generic interface [14]. However, it is important to state that the increase of the power transmission's efficiency was not tested, although the results seem to corroborate the suggested hypothesis.

### ***Comfort and safety parameters***

Besides taking into consideration the power supply and the weight of the structure, it is critical to guarantee that the robot is comfortable, ergonomic and safe to the user. These factors are directly influenced by the actuation and control of the exoskeleton, as well as, by its kinematic design [16].

It is possible to define kinematics as the branch of mechanics dedicated to the study and description of the bodies' motion, without taking into consideration the forces that originated that same motion [17]. A defective kinematic design can lead to undesired interaction forces between the exoskeleton and the user, which can result into fatigue to the user [17], alteration of the natural muscle activation patterns, which can be counterproductive during, for example, physical therapy, and finally safety hazard, as well as discomfort [18].

Normally, the guideline used to maintain the safety of the user is to avoid the application of pressures above the ischemic level, in other words, avoid pressures above the level at which the capillary vessels are unable to conduct blood ( $\approx 30$  mmHg or  $\approx 4$  kPa). However, a recent study showed that capillary closure depends on other factors besides the pressures at the skin level, depends for example on the time duration the pressure is applied, as well as the body part exposed to that same pressure. According to this study, for the lower limb, the pain detection threshold, PDT, which can be associated to discomfort, ranges from  $16.3 \pm 11.2$  to  $34.1 \pm 21.0$  kPa and the pain tolerance threshold, PTT, ranges from  $42.7 \pm 11.6$  to  $90.5 \pm 18.0$  kPa [19].

Since the interaction forces between the exoskeleton and the user are vital for the proper functioning of the exoskeleton, it is essential to measure and quantify them. The quantification of the human-robot interaction can be achieved by the application of two distinct methods: by making an estimation of the applied forces or by directly measuring them.

To achieve an exact estimation of the interaction forces, a dynamic and friction model of the exoskeleton's behaviour must be calculated, which is notably difficult to obtain. In opposition, measuring directly the forces applied by the exoskeleton is a more straightforward and simpler measurement technique. To apply this last technique S. M. M. de Rossi *et al.* suggests the use of a thin, distributed pressure sensor, to be inserted between the user and the cuff/orthosis, covering the whole interaction area [20].

In conclusion, monitoring the interaction forces between the exoskeleton and the user could be a strategy to potentially improve the user's comfort and safety and, potentially facilitate the understanding of the power transmission and its efficiency, allowing the optimizing of the exoskeletons'

performance. Furthermore, the exoskeletons' cuff should be formed by high stiffness materials and designed to interact with bony prominences of the body.

### ***1.2.2 Exoskeleton's control***

Besides sensing the interaction forces, it is also important to have some form of mechanical sensor to control the position, force or torque applied by the exoskeleton to the user. According to A. J. Young and D. P. Ferris, the two most common forms of control are: the position-based control and the direct force (or torque) based control [1].

The first form of control is useful when the user has little ability to interact with/or control the exoskeleton, since it applies a set of predefined joint angle trajectories [1]. The second form of control can be applied based on two different strategies: by performing an open-loop form of control, where a pre-specified force or torque is applied based on the assumed phase of a specific motion (this control technique is difficult to optimize when multiple movements/conditions are required) or by the application of a force/torque that is proportional to the readings of a specific sensor. The sensor can be an electromyography sensor, EMG sensor, placed over a relevant muscle, or a force sensor placed between the user and the exoskeleton [1].

The advantage of using EMG sensors over force sensors is that with the use of force sensors, the user must be able to initiate the movement before the exoskeleton is able to assist it, limiting the number of areas where the exoskeletons can be applied. However, because the EMG signals reflect the human's motion intention in real time, the exoskeleton can assist the patient at all time. Also, the EMG signals reflect the contraction force and speed of each muscle [21], [22].

Although the use of EMG recordings to control the exoskeletons has great advantages, it also has some drawbacks: the EMG signals aren't stable over time and it is difficult to obtain the same EMG signal for the same motion, even with the same person, since they depend on a variety of factors such as the placement of the sensors, fatigue of the muscles and sweat. Also, because there are many muscles involved in every joint motion, it is not easy to predict with accuracy to which motion each signal corresponds [21], [22].

Despite the downsides of using EMG signals to control exoskeletons, there have been a number of studies basing their control strategies on EMG readings, some examples are [8], [21], [23]. Furthermore, there is an exoskeleton currently on the market using this type of control strategy, the HAL® Therapy [24].

In conclusion, the cuffs/orthoses of the exoskeleton could be personalized with their contact areas sensorized, either for measuring the interaction forces between the user and the exoskeleton, either for controlling the exoskeleton according to the user's will.

## **1.3 Sensors**

As previously mentioned, when designing an exoskeleton, it is important to incorporate a measurement system able to access the intention of the user, to better control the exoskeleton, and also to measure the interaction forces between the user and exoskeleton itself.

Several authors from different studies have been developing sensors to be integrated into the most variety of fields (prosthetics, human-machine-interfaces, clinical rehabilitation) to access the interactions between the user and the surrounding environment [25]–[28]. Despite the variety of applications for the developed sensors, all the studies adopted the same strategy to develop them. They developed sensors able to mimic the human's skin sensory ability. For this reason, the same approach will be

applied in this project to decide which type of sensors are going to be used to measure the interaction between the user and the exoskeleton.

There are seven types of skin receptors: pain, cold and warm receptors and four mechanoreceptors responsible for measuring the innocuous mechanical stimuli, more specifically, measure forces on different time-scales, dynamic or static, and with different receptive field sizes [25].

The mechanoreceptors are divided into two groups: the slow adapting receptors (SA-I, SA-II) and the fast adapting receptors (FA-I, FA-II). The SA-I measures static forces with high resolution and are used to describe object shapes and textures, the SA-II measures skin stretch, and it is crucial for proprioception. Regarding the fast adapting receptors, the FA-I measures the position and slip changes of objects in a person's hand which will translate in an adjustment of the grip forces, while FA-II measure high-frequency vibrations over large areas [25].

It was contemplated, in the previous subchapter, that it would be favourable for the exoskeletons' efficiency to have a monitoring system able to quantify the interaction forces between the user and the exoskeleton. Therefore, combining this information with the skin receptors' information, it is possible to conclude that the most suitable sensors to be incorporated into the exoskeleton's interface are the sensors mimicking the four mechanoreceptors.

Consequently, the type of sensors that can be incorporated into the interface are: the sensors able to measure static forces applied along the normal direction in regard to the contact area, mimicking the SA-I receptors, the static strain sensors, to simulate the stretching of the skin, which is monitored by the SA-II receptors, and the dynamic force sensors, to mimic the FA-I and -II mechanoreceptors.

Regarding the sensors responsible for accessing the user's intentions, the EMG sensors are the most suitable ones.

### ***1.3.1 Electromyography sensors***

To understand the human's motion, is to understand the muscles way of working, how the nervous system communicates with them, and how this communication transforms thoughts into actions.

The nervous system is divided into two different systems: the central nervous system (CNS), constituted by the brain and spinal cord, and the peripheral nervous system (PNS), formed by the sensory receptors, nerves, ganglia and plexuses [29]. The CNS is mainly responsible for processing information, initiating responses, and integrating mental processes, the PNS is responsible for detecting stimuli and transmitting information to/from the CNS.

Based on the last function of the PNS, it is also possible to divide the PNS into two subcategories: the sensory/afferent division and the motor/efferent division. In the first division, the nerves transmit information from the sensory receptors to the CNS and, in the second division, the nerves transmit information from the CNS to the effector organs (muscles or glands) [29]. This information is transmitted through the nerves as electrical signals, called action potentials.

Each nerve is constituted by a set of neurons, in this case, motor neurons, and each neuron is connected to a set of muscle fibres. The muscle fibres with the connective tissue constitute the muscles. The information is originated in the CNS and passed to the motor neurons, as action potentials. When the action potentials reach the end of the neurons the information is passed to the muscle fibres through synapses. Because the plasmatic membrane of the muscle fibres, like the neurons, is excitable, when an action potential reaches the muscle fibre, the membrane's potential difference changes momentarily from -90 mV to +30 mV, this will initiate the contraction of the muscle fibres that can last more than 100 ms [30].

Since the action potential is an electrical signal and the skin is a moderately conductive tissue, as well as the tissue between the muscle fibres and the skin, it is possible to measure it by placing a metal surface or even a conductive material directly over the skin [31]. The metal surface is the EMG transducer and the technique of capturing the bioelectrical signals, originated in the skeleton muscle, the electromyography, EMG.

To register the EMG signals, if the bipolar measurement principle is in use, it is only necessary three transducers. Two of the transducers, are placed over the same muscle, with the purpose of calculating the difference between the measured potentials in each transducer. The third one, is placed in a neutral location, where the EMG signals are normally constant, to be a reference point.

After the signal is captured, it goes to the amplifier. Besides amplifying the signal, captured by the electrodes, the amplifier is also used to eliminate the noisy signals originated from the power line supply [32]. However, it is important to understand that the amplifier has also an impact in the fidelity of the EMG signals, especially in the signal-to-noise ratio and in the distortion of the signals [33].

The frequency spectrum of the EMG signal, collected with commonly used sensors, ranges from 0 to 400 Hz [34], however not all the totality of the captured signal is generated by the muscle fibres, there are also other sources of electrical signal contributing for the final signal. For this reason, it is necessary to properly filter the signal, after the amplification.

The movement artefact noise in conjugation with the baseline noise, which includes the power line noise, the cable motion artefacts, the noise associated with the amplification system and the electrode-skin interface, are low frequency noise sources, therefore it is necessary to filter the signal with a high pass filter. The location of the filter's corner frequency should be around 20 Hz, however it differs from author to author and also changes with the purpose of the recordings [34],[31].

The low pass filter should be set where the amplitude of the noise components surpasses the EMG signal, which corresponds usually to a low-pass corner frequency in the range of 400-450 Hz [34]. Besides the low-pass and high-pass filters there should be a third filter, a 50 Hz notched filter because of the outer net interference [31].

After filtering the signal, it has to be sampled and then converted from analog to a digital signal, A/D conversion. According to Nyquist theorem the signal must be sampled at least twice the frequency of its highest harmonic, which in this case means 400-450 Hz. This avoids loss of information and the phenomenon called "aliasing". The sampling recommendation is 1000 samples per second [31]. The A/D conversion transforms the sampled voltages into "levels" represented in the binary code, being the highest value the correspondent of the specific input range of the A/D converter.

After the amplification, application of the filters and digitalization of the EMG signal, it is ready to be analysed. From this stage the signal will be treated differently according to the purpose of their capture. If the signal is destined to be used to control an exoskeleton, then the digitized signal is sent to the controller. In the controller the data is segmented, so it is easier to extract pre-selected features. The pre-selected features will work like a signal pattern used to classify the signals into pre-defined categories. The output command, that is sent to the exoskeleton, will reflect the selected category [35]. All the process, starting with the information being originated in the CNS until it arrives to the exoskeleton is represented in Figure 1.2.

If the signal is used to study a specific muscle behaviour and, for that reason, to be analysed offset, then it is just required the segmentation of the signal, and from each segment, also known as epoch, extract some specific features.

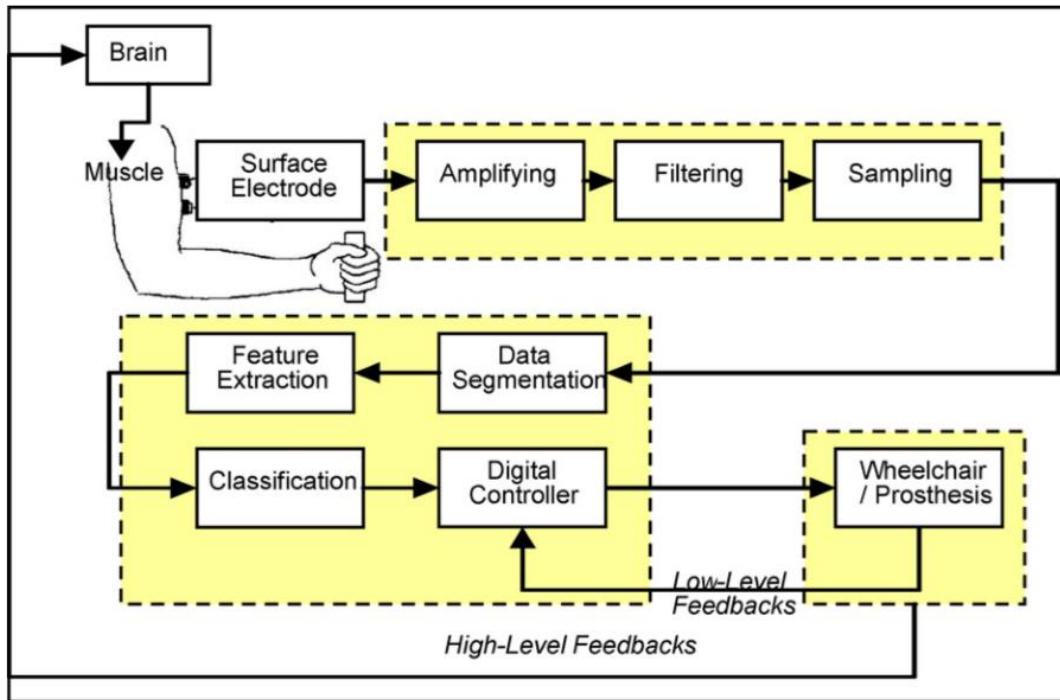


Figure 1.2: A myoelectric control system based on pattern recognition [35]

There are several types of features that can be used to access the EMG signals, they can be either spectral features or amplitude features. The most used spectral features are the mean and median frequency (MNF and MDF). These features are most used to access fatigue since it has a high impact in these parameters, in opposition to the exercise intensity, more precisely, to the different levels of voluntary muscle contraction, which almost does not alter the frequency spectrum [36]. The spectral features are indicators of spectral compression [37] and are affected by the spectral shape, epoch duration, degree of overlapping, type of windowing and other smoothing or interpolation procedures [38], also, the muscles' temperature influences these type of features [39].

It is important to calculate both features, since they both have their specific advantages, for example, the MNF values usually have lower associated standard deviation values, when compared to the MDF values, however MDF values are less affected by random noise and are more affected by fatigue [40].

Regarding the amplitude features, usually the chosen ones to access the signals' amplitude are the average rectified value (ARV) and the root mean square (RMS) value. In the case of the first feature, the ARV, it is associated to the area under the rectified signal, while the RMS is associated to the mean power of the signal within a specific time window [37]. This type of parameters, in opposition to the spectral features, are affected by the intensity of the muscles' exercise, in other words, affected by the level of muscular contraction [36].

According to literature [37], [39], [41], [42] it is expected for both MNF and MDF values to decrease with the increase of muscular fatigue, which implies that for the same period of time, the variation of the MNF and MDF values will be as higher as the level of fatigue, which is directly proportional to the muscular contraction level. In respect to the RMS values, the reported tendency is for the RMS values to increase with the increase of the contraction level [36], [43], [44].

### 1.3.2 Force and strain sensors

The force sensors are usually designed to measure pressure-like forces, which, by definition, are forces that act along the normal direction to a contact surface. In contrast, strain sensors assess pressure-like forces in simultaneous with shearing forces (forces that act in any tangential direction to the surface) by the local deformation of a certain material which the sensor is made of [25], [45] (Figure 1.3).

Both static and dynamic force sensors, as well as, the static strain sensors measure mechanical quantities. Usually, these type of sensors convert the mechanical quantities into resistance or capacitance variations [2], so it is essential first to understand the physical concepts they are based on.

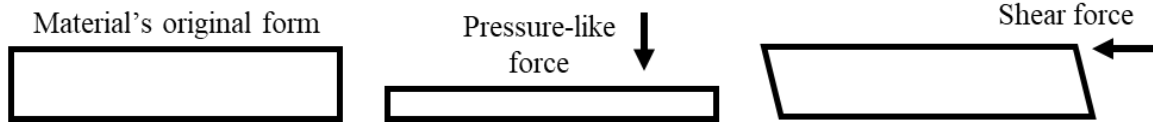


Figure 1.3: Representation of the effect of pressure-like and shear forces into a flexible material

#### Capacitance

According to C. K. Alexander and M. N. O. Sadiku a capacitor is a passive circuit element, designed to store energy in its electrical field. It consists of two conducting plates separated by an insulator, or dielectric (representation in Figure 1.4).

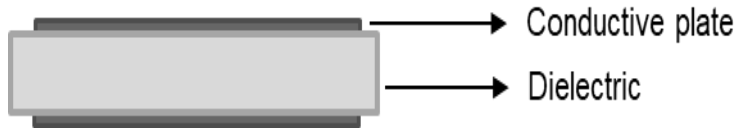


Figure 1.4: Schematic representation of a capacitor with parallel electrodes, the darker parts represent the two conductive plates and the lighter part the dielectric.

When a voltage source,  $v$ , is applied to the capacitor, the source deposits a positive charge,  $q$ , on one plate and a negative charge on the other, since  $v$  and  $q$  are directly proportional, it is possible to define capacitance,  $C$ , as the ratio of the charge on one plate of the capacitor to the voltage difference between the two plates, measured in farads (F), Equation 1.1 [46].

$$q = Cv \quad [1.1]$$

Although the capacitance is a proportional ratio, it also depends on the physical dimensions of the capacitor. In the case of a parallel-plate capacitor, Figure 1.4, the capacitance,  $C$ , is directly proportional to the surface area of each plate,  $A$ , times the permittivity of the dielectric material,  $\epsilon$ , and inversely proportional to the distance between the plates,  $d$ , Equation 1.2 [46]. In some cases, is important to define  $\epsilon$  as the multiplication of the vacuum permittivity,  $\epsilon_0$ , and the relative dielectric constant,  $\epsilon_r$  [47].

$$C = \frac{\epsilon A}{d} = \frac{\epsilon_0 \epsilon_r A}{d} \quad [1.2]$$

Since the electrical current,  $i$ , is the time rate of change of charge, measured in amperes (A) [46], it is possible to define two new equations, Equation 1.3 and 1.4, based on Equation 1.1.

$$i = C \frac{dv}{dt} \quad [1.3]$$

$$v(t) = \frac{1}{C} \int_{t_0}^t i(\tau) d\tau + v(t_0) \quad [1.4]$$

## Resistance

Resistance can be defined as the physical property or ability to resist the flow of electric charge or current. Resistance,  $R$ , depends on the material's properties and geometry, more precisely depends on the length,  $l$ , cross-section area,  $A$ , (or the height,  $h$ , and width,  $w$ ) and resistivity,  $\rho$ , of the material [46], Equation 1.5.

$$R = \frac{\rho l}{A} = \frac{\rho l}{wh} \quad [1.5]$$

Usually, when a mechanical stress is applied to a conductive material, in most cases, the changes in the resistivity,  $\rho$ , are neglectable, since the changes in resistance are mainly due to the geometry changes ( $l$  and  $A$ ), however, the same does not happen to the semi-conductive materials, since the structure of the semi-conductor is modified as the pressure is applied, changing the resistivity of the material, this effect is known as piezoresistive effect [48].

## Static force sensors

Measuring the static forces or pressure with a sensor array is the same as measuring the normal force distribution across a surface area [25], and it can be done by using capacitive or resistive sensors.

Usually, when designing capacitive sensors to access static forces, the capacitors with parallel electrodes are the most popular ones, since their capacitance changes almost linearly, with the distance between the electrodes, Equation 2.2. These type of sensors have great sensitivity for detecting static forces and a low-power consumption, however, they are susceptible to electromagnetic interference so they must be shield, Figure 1.5 example a, [25], [26].

The second type of sensors, the resistive sensors, can be made in two different ways: based on the intrinsic piezoresistivity properties of the materials, Figure 1.5 example b, or in a contact between a conductor and an electrode, Figure 1.5 example c. In the second case, also known as contact resistance modulation, a contact area between a conductor and an electrode changes with the application of a force. Increasing the force applied to the sensor, will increase the contact area between the conductor and the electrode, which will lead to a change in the contact resistance [25].

## Static strain sensors

Like the static force sensors, the measurement of the static strain can also be achieved by using resistive and capacitive based sensors.

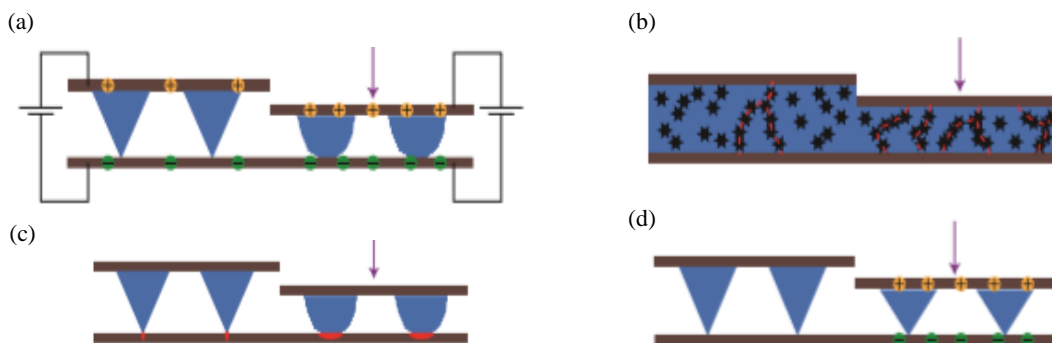


Figure 1.5: (a) capacitive sensor, (b) sensor based on the intrinsic piezoresistivity properties of the material, (c) sensor based on contact resistance modulation, (d) piezoelectric/triboelectric sensor. [25]

The resistive sensors are usually based on the variation of a certain parameter of the resistance equation, Equation. 2.5. They can be designed to only change the output values, the measured resistance, when there is a variations in the geometry of the sensor (cross-section area,  $A$ , and the length,  $l$ ), or they can be designed to only change when there is a change on the resistivity of the material (changes in the geometry of the sensor are neglectable), basically sensors based on the piezoresistive effect [25].

It is also possible to measure the static strain, with stretchable capacitors, since the dielectric thickness and the electrode area can change [25].

### ***Dynamic force sensors***

To measure dynamic forces, piezoelectric and triboelectric sensors are the most appropriated ones and unlike the previous sensors, they have the particularity of producing voltage in response to a mechanical deformation, Figure 1.5 example d [25].

According to X. Wang, in the piezoelectric materials there is a production of electrical charges in certain materials under mechanical force due to the occurrence of electrical dipole moments. They are widely used to convert mechanical stresses and vibrations into electrical signals [26].

In the case of the triboelectric sensor (TES), the contact electrification is used to generate a voltage signal in response to a physical contact without the need of an external power supply [26], [49].

## **1.4 3D Printing methods**

Applying sensors to the exoskeleton's structure has significant advantages, however, it has some setbacks as well. One of the complications is the integration of the sensors that are currently on the market into the exoskeletons, since, in most cases, the exoskeletons' design and functionality has to be compromised for the sensors to be integrated. Also, the traditional manufacturing methods have several drawbacks: the fabrication process has too many steps that are time-consuming, which leads to a lack of manufacturing scalability and an increase of the fabrication costs, if the goal is to achieve high-resolution structures [2].

Trying to solve these problems, there has been an increasing interest towards 3D printing technology. This technology provides the possibility to directly print the desired sensors, print models for casting the sensors or even printing research platforms to be integrated with sensors that are already being commercialized [2]. With 3D printing technology, it is possible to have a fully integrated manufacturing strategy with a customized interface, which will ultimately translate in a more efficient exoskeleton. Also, the number of fabrication steps can be reduced leading to a reduction on the fabrication time [50].

The operating principle behind the 3D printing technique is the deposition of a specific material or ink in successive layers, on top of each other, to form a 3D object. There are several 3D printing techniques: some of them use lasers to solidify resins, stereolithography (SLA), digital light processing (DLP), selective laser sintering and melting (SLS and SLM), or powders, electronic beam melting (EBM), to cut existing materials, laminating object manufacturing (LOM) or even to melt thermoplastic materials, Fused deposition modelling (FDM) [48], [51].

The most used 3D printing technique is the FDM technique since it uses low cost materials, has an open source system, and can print several materials simultaneously. In this 3D printing technique, a filament, more specifically a thermoplastic material, is passed through a heated nozzle and the nozzle will melt the material. The extrusion head, where the nozzle is inserted, moves in the x- and y-axes direction placing the melted material in the desired location to make a layer. After the thermoplastic

material is placed in the desired location, it cools down and returns to its original state. Every time a layer is completed the platform lowers in the z-axis direction, this process is repeated until the 3D object is achieved [52]. Although it is an exceptional technique, it also has some limitations, it has a low printing resolution when compared to other printing techniques, and the printing speed is also very low [2].

To produce pressure/force and strain sensors, as well as EMG sensors it is necessary to combine conductive and non-conductive materials together. To that end, three major techniques are used: hybrid approaches, conductor infusion or infused conductors and multi-material printing [50].

The first printing technique, the hybrid approach, combines printed and non-printed parts, one example is the integration of regular wires into 3D printings. The advantage of using this particular technique is that the conductors can be made from any material, the downside is it doesn't allow the user to have full freedom in the design and requires extensive mechatronic equipment to combine wire routing with 3D printing [50].

In the second printing technique, the conductor infusion technique, channels are printed with non-conductive materials and infilled with conductive ink. It allows great freedom of design as long as the channels are supported with soluble materials and the material, which the channels are made of, are impermeable to the fluids that are going to be infused later on in the fabrication process. However, dissolving the support material is not always easy, especially for narrow channels and the actual infusion even more [50].

The last technique, the multi-material printing technique, prints the conductive and non-conductive filaments all together at the same time. It allows the most freedom of design and straightforward fabrication, however, there are limited materials that can be used and even fewer that can combine with each other, also the conductive properties of the conductive materials have relatively high resistivity [50].

## **1.5 Examples of 3D printed sensors**

There have been some developments on the 3D printing field, and the sensors field is no exception. In the later years, some research papers have been published, showcasing 3D printed capacitive sensors, as well as, resistive sensors, showing big promises to the sensors future although using different 3D printing techniques. Therefore, the following subchapters will report some research examples that have been developed regarding the 3D printed force and strain sensors, along with an example of 3D printed EMG sensor.

To the author's knowledge, there were no developments regarding the contact resistance modulation sensors and the piezoelectric and triboelectric sensors 3D printed.

### ***1.5.1 3D printed capacitive sensors***

In the work of M. Schouten, R. Sanders, and G. Krijnen *et al.*, a flexible capacitor was designed to be 3D printed with the FDM printing technique, combining regular and conductive thermoplastic poly-urethane (TPU) materials to produce a force sensor, Figure 1.6 example a. With the chosen dimensions for the electrodes and dielectric, it is possible to do a parallel plate approximation, which allows the application of the Equation 2.2. With this approximation, it is possible to establish a relationship between the variance of the measured capacitance and the applied force [47].

S. J. Leigh *et al.* were also able to produce a capacitive sensing device for a customized 3D printed Human-Interface-Devices (HIDs) to be printed with FDM printing techniques, Figure 1.6 example b. The primary purpose of their work was to develop a conductive thermoplastic composite, which they labelled as ‘carbomorph’ and demonstrate how it can be applied, by a low-cost 3D printer (FDM technique), to print electronic sensors able to sense mechanical flexing and capacitive changes [48].

Although these two studies showed excellent results and applicability, the presented sensors are only able to measure pressure variations. Ideally, a sensor that could measure pressure and strain simultaneously would be more complete and better to quantify the interaction forces between the user and exoskeleton.

With this idea in mind, Laszczak *et al.* developed a capacitance-based sensor to be used as an interface between a stump-socket and a lower-limb amputation with the goal of measuring the pressure and shear stress simultaneously, Figure 1.6 example c. The sensor was produced with a hybrid approach, where only the dielectric is 3D printed, the electrodes were made out of copper [53].

The sensor was constituted by three separated electrodes on the top,  $E_x$ ,  $E_y$  and  $E_z$  and one single electrode on the bottom that was common to the other three,  $E_{com}$ . To separate the top and bottom electrodes a 3x3 array filleted pillars was designed and 3D printed. With this arrangement, three capacitors are formed. The electrode  $E_z$  is completely overlapped by the  $E_{com}$ , in opposition to  $E_x$  and  $E_y$  that are only partially overlapped. If the force applied in the electrodes is perpendicular to the sensor, there is only a shift in the distance between plates,  $d$ , so every capacitor will register the same variation of capacitance (Equation 2.2), however, if the force is not perpendicular, the overlapping area,  $A$ , between  $E_x$  or  $E_y$  with  $E_{com}$  will change, so every capacitor will register different changes in capacitance, with the three different values is possible to know the direction and the magnitude of the applied force (Equation 2.2).

Although it is a promising sensor design, only the dielectric was 3D printed, so maybe it is possible to apply the M. Schouten *et al.* and S. J. Leigh *et al.* printing technique, a multi-material printing technique using FDM technique, to their sensor design.

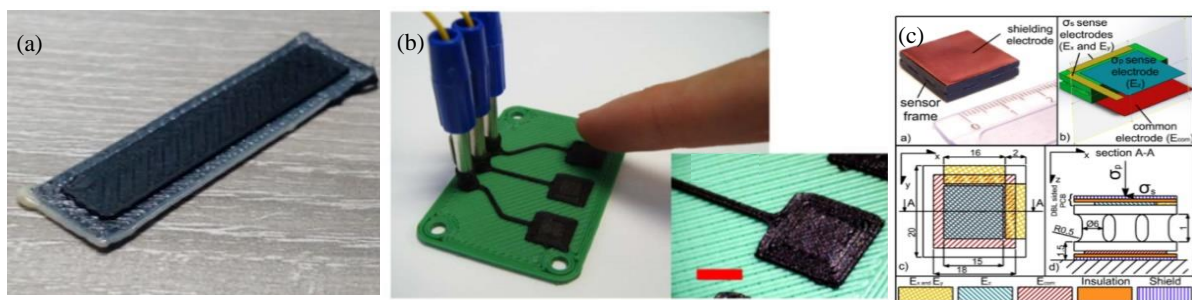


Figure 1.6: Examples of 3D printed capacitive sensors (a) M. Schouten *et al.*'s sensor [47]; (b) S. J. Leigh *et al.*'s sensor [48]; (c) P. Laszczak *et al.*'s sensor [53]

### 1.5.2 3D printed resistive sensors

When S. J. Leigh *et al.* developed the conductive thermoplastic composite, the ‘carbomorph’, they also test it for mechanical flexing. By using the piezoresistive nature of the ‘carbomorph’, they were able to measure the flexion of the fingers. To do it, they embedded the sensors, made from the conductive thermoplastic material, into an ‘exo-glove’ interface, above the fingers’ articulations, and register the resistance variations measured in the sensors, Figure 1.7 example a. All the ‘exo-glove’ structure was 3D printed, using a multi-material printing technique [48]. A. Dijkshoorn *et al.* also referred 3D printed sensors with the same base of principle and construction.

Using a polyject technique, B. Shih *et al.* designed two different sensors, a uniaxial strain sensor and a multilayer integrated strain and pressure sensor, Figure 1.7 example b. In contrast to the previous example, in this study, the resistivity was considered constant, limiting the output variations to be only due to the changes in the sensor's geometry. However, it wasn't completely successful since there were some changes in the resistivity, leading to the important to conclusion: when the material is conductive because it has carbon particles incorporated, the variations in resistivity can't be negligible [54].

A more complete sensor was developed by S. Harada *et al.*, a three-axis tactile force sensor, Figure 1.7 example c. In this sensor, an arrange of electrodes were specially designed to incorporate four strain sensors, two temperature sensors and a fingerprint structure, per cell. The fingerprint was applied in the top of a membrane and the four strain sensors were uniformly placed around it, allowing the determination of the touch and slip/friction force applied, [55]. To print these sensors, they used a screen printing technique on a flexible substrate, which allowed them to print electrodes with a height inferior to 30 $\mu$ m, which is not possible with nowadays FDM printing techniques, however, maybe applying the same principle as the resistive S. J. Leigh *et al.*'s sensors to this sensor design, could produce a 3D printed resistance-based pressure-like force and strain sensor.

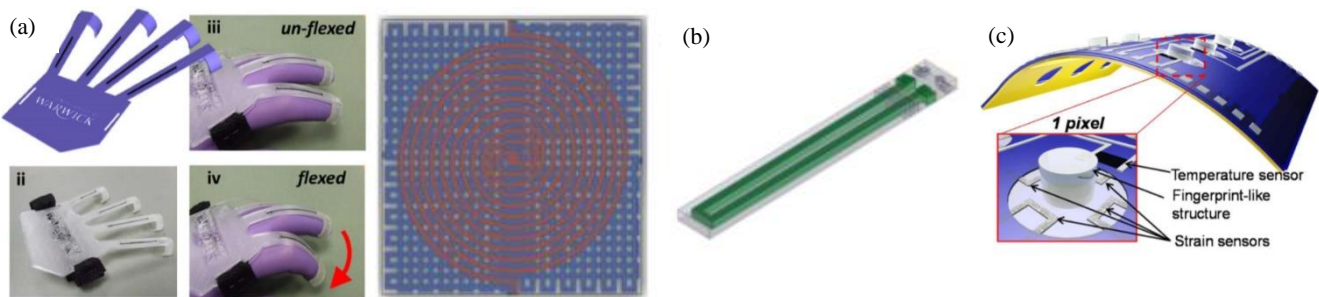


Figure 1.7: Examples of 3D printed resistive sensors (a) S. J. Leigh et al.'s sensor [48]; (b) B. Shih et al.'s sensor [54]; (c) S. Harada et al.'s sensor [55]

### 1.5.3 3D printed EMG sensors

To the author's knowledge, there is only one study where an EMG sensor was developed by using an FDM technique, the G. Wolterink, R. Sanders, and G. Krijnen 3D-printed sEMG electrode. To produce these sensors, they 3D printed, in one go, two conductive parts, with a conductive TPU, connected by a non-conductive TPU material. The conductive parts are the transducers of the sensor allowing the application of the bipolar measurement principle. The ground was printed separately. With the new sensors, they were able to have the same results as the ones achieved with the commercial ones [44], which shows excellent prospects to the application of 3D printing techniques to the EMG field.



Figure 1.8: G. Wolterink, R. Sanders, and G. Krijnen 3D-printed sEMG sensor [44]

## 1.6 Exoskeleton's cuff design

As referred in the previous subchapters, to improve the exoskeletons' performance, EMG and force and/or strain sensors, should be incorporated into the exoskeletons' cuff. The EMG sensors to enhance the exoskeletons' control efficiency, and the force and/or strain sensors to monitor the interaction forces between the user and the exoskeleton, to assure the user's safety and comfort, and to improve the exoskeletons' control as well. The next phase, described in this subchapter, is to choose which type of force/strain sensor is the most suitable for this project, and understand the implications of integrating the two types of 3D printed sensors into the exoskeleton.

### *1.6.1 Determination of the type of sensor to incorporate into the exoskeleton's cuff*

From the three categories presented in the subchapter "Force and strain sensors", it would be logical to choose a sensor showcased in the dynamic force sensors' category, which means selecting a piezoelectric or a triboelectric sensor, however, to the authors knowledge, there is no published research describing the development of such sensors fabricated with 3D printing techniques. Also, the materials required to produce this type of sensors have specific characteristics, which, is cannot be possible to find in materials destined to be printed by FDM printers. Due to the two presented reasons, both types of sensors were not considered to be suitable for the purpose of this research.

Since the dynamic force sensors are no longer a possible choice, the decision is between static force sensors and static strain sensors. Although it was presented in the previous subchapter 3D printed sensors that could access both pressure and strain simultaneously, their design was based on force sensors, which implies first to study the pressure effect on the 3D printed sensors and only after change their geometry so they are able to measure strain as well. In consequence to what was mentioned, for a matter of simplicity and due to the time available, only force sensors were chosen to be incorporated into the exoskeleton's cuff.

From this stage the characteristics of the capacitance-based and resistance-based force sensors must be studied, in order to understand which are the advantages and disadvantages of each type of sensor and determine which one is the most suitable for the purpose of the project.

The capacitance-based force sensors are more sensitive to pressure variations and require less energy to work, also, they perform better in terms of accuracy and repeatability when compared to the resistance-based sensors, however they are also susceptible to electromagnetic interference, which the resistance-based sensors are not. In the other hand, the resistance-based sensors display a larger hysteresis and their performance is more likely to change with environmental factors like temperature or humidity. However, the resistance-based sensors have a simpler readout mechanism. Regarding the response time, the capacitance-based sensors are faster and show a higher linearity when compared to the resistance-based sensors, in opposition the last sensors can be fabricated to be more flexible and stretchable, which depending on the application can be useful [25], [26],[56], [57]. This information is summarized in Table 1.1.

Comparing all the qualities of each type of sensor, the chosen sensor, to be incorporated into the exoskeleton's cuff, along with the EMG sensor was the capacitance-based force sensor.

Table 1.1: Comparison between the main characteristics of the capacitance-based and resistance-based force sensors. The values in green represent the desirable behaviour to the respective characteristics and the orange the opposite.

	Capacitance-based force sensor	Resistance-based force sensor
Pressure sensitivity	Higher	Lower
Power-consumption	Lower	Higher
Electromagnetic interference	Susceptible	Not Susceptible
Linearity	Higher	Lower
Sensitivity to environmental factors	Lower	Higher
Flexibility	Lower	Higher
Time-response	< 10 ms	< 20 ms
Readout mechanism	More complex	Simpler
Repeatability of measurements	Higher	Lower

### 1.6.2 Integration of the 3D printed sensors into the exoskeleton's cuff

With the sensors selected, the next crucial decision is where to place them and understand if the cuff's design will be influenced by the optimal sensor's location. Starting with the force sensors, their main purpose is to measure the interaction forces between the user and the exoskeleton so they will not affect the cuff's design. However, with the placement of the EMG sensors the same will not happen.

To properly work, the EMG sensors should be placed in the most prominent part of the muscles, which corresponds to areas with elevated levels of biological tissue deformation. This imposes a great challenge since the conclusion from the "1.1.1 Key features to design an efficient exoskeleton" sub-chapter was: to increase the efficiency of the power transmission, there should be an increase of the interface's contact stiffness while interacting with bony prominences, and not with soft tissues. Therefore, the placement of the EMG sensors will affect the exoskeletons design and probably the choice of the materials to fabricate them.

To achieve the balance between having a robust interface, but at the same time flexible enough to ashore the correct placement of the sensors at all times, while maintaining the user comfortable and safe, it is necessary to carry out an intensive study to comprehend how the muscles' behave, and how for each specific individual the overall limb's geometry changes with the tasks the exoskeleton is supposed to assist.

In the case of this project, the plan was to use the exoskeleton already developed in the BioMot project [14], and redesign its cuff to have incorporated EMG and force sensors. Since this exoskeleton is a lower limb exoskeleton, the lower limb muscles must be studied, and their deformation, produced during the gait cycle, analysed. This analysis has two main goals, the first one to decide which muscles are the most suitable for the EMG sensors to be placed and the second one to understand where the biggest deformations are, in order to help the cuffs design and choice of materials.

#### *Gait cycle*

According to M. W. Whittle, *et al.* gait cycle, can be defined as the time interval between two successive occurrences of one of the repetitive events of walking [58]. Usually, the chosen event is the contact of one of the heels with the ground [4], [14], [58], [59], so, for this reason, in this study, the starting event of the gait cycle, will also be the contact of the heel with the ground.

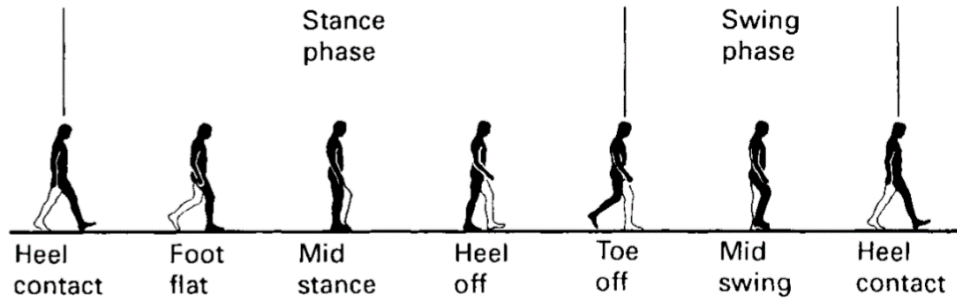


Figure 1.9: Position of the legs during a single gait cycle from right heel contact to right heel contact [58]

The gait cycle can be split into two phases: the stance phase and the swing phase. What differentiates the two phases is the contact, in the case of the first phase, or the lack of it, in the case of the second phase, with the ground. Both phases can also be divided into specific periods, Figure 1.9.

As referred previously, the gait cycle is initiated with the contact of the heel with the ground, which is also known as heel strike. The heel strike is followed by the foot flat position, which, as the name implies, is the moment when the foot is fully touching the ground.

After the foot flat position is the mid stance position, characterised by the body's centre of gravity being at its highest position, following the mid stance position is the heel off position where the heel loses contact with the ground, the stance phase terminates with the toe off position where the foot is taken entirely of the ground [58], [59].

With the toe off position, the swing phase is initiated, during this phase, the leg behaves just like a pendulum, the middle of this stage is called mid swing [60].

Several muscles constitute the lower limb, and each one plays a different role in the human's locomotion, more specifically in the control of the foot, ankle, and knee.

The ankles' motion is basically confined into two categories: the dorsiflexion and plantar flexion motions. The dorsiflexion is when an upward travel of the foot happens, in contrast to the plantar flexion, which occurs when the ankle performs a downward motion [59]. The muscles responsible for the dorsiflexion motion are the: Tibialis anterior, Extensor digitorum longus and the Extensor hallucis longus, regarding the plantar flexion motions the number of muscles responsible for this motion increases, however, 93% of the theoretical plantar flexor torque is performed by the soleus and the Medial and Lateral Gastrocnemius [29], [59].

The muscles that control the plantar flexion motion are active in the stance phase, while the dorsiflexors muscles are active during the swing phase and in the loading response part of the stance phase, which corresponds to the period between the heel strike and foot flat positions [59]. Because these two types of muscles are active in different phases of the gait cycle, it is important when choosing the muscles to place the EMG sensors, that there is at least one of each type, since choosing different muscles that actuate in different moments of the gait cycle leads to a better understanding of the gait cycle itself.

As referred previously, the sensors that were chosen to access the muscles' activity, were the surface EMG sensors. This sensor's choice restricts the number of muscles that can be used to describe the gait cycle, since they can only properly access superficial muscles. From this information in conjunction with the information about the ankle's motion, the muscles that are going to be studied are: the Tibialis anterior, and the Medial and Lateral Gastrocnemius. In the case of the Tibialis anterior, the

choice was also based on its cross-section, since it is the one with largest cross-section between the three dorsiflexion muscles [59].

The activity of the Tibialis anterior begins moments before the toe off position and reaches its activity peak moments after the heel contact or heel strike position. The Medial and Lateral Gastrocnemius are activated with the foot flat position. From the foot flat position to the heel off position the muscle contract first eccentrically, which translates into the muscle's elongation, and after isometrically, which means the length of the muscles is maintained during the contraction. The heel off position is the result of the concentric contraction of the gastrocnemius, resulting in a shortening of the muscles, this stage corresponds to the highest activity moment. From this moment to the toe off position moment, the muscle's activity decreases until it reaches a quiescent stage, which is maintained until the next foot flat position [58], [60], [61].

In conclusion, for this project, the EMG sensors will be placed over the Tibialis anterior and the Lateral and Medial Gastrocnemius, so their deformation along the gait cycle must be meticulously studied.

## 1.7 Project framework

This project was developed in the Brussels Human Robotics Research Center, BruBotics, in collaboration with the PhD student Kevin Langlois.

The BruBotics Research Center of Vrije Universiteit Brussel [62] combines eight research groups with the main goal of improving the quality of life and working conditions of people through human robotics. One of the eight research groups is the Robots & Multibody Mechanics research group [63], where the investigation covers mainly two different domains: the physical Human-Robot Interaction and the cognitive/social Human-Robot Interaction. Focusing on the first research domain, the physical Human-Robot Interaction domain, the majority of advancements, made in this laboratory, have been

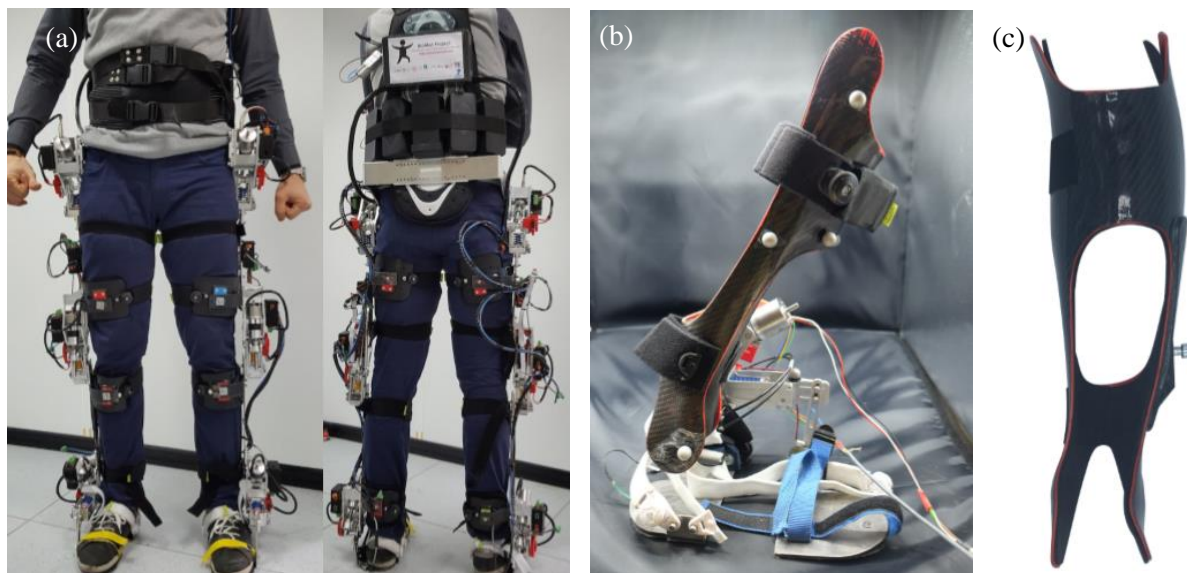


Figure 1.10: (a) The entire structure of the BioMot gait exoskeleton [64]. (b) Customized physical interface attached to the ankle foot model of the FP7 BioMot exoskeleton [14]. (c) 3D printed, customized interface made with PLA and reinforced with a carbon fiber and epoxy resin composite [14].

towards the development of prototypes for rehabilitation and assistive exoskeletons, human-augmentation devices and bionic prostheses.

One of the projects, in current development, concerning the rehabilitation of the lower limb through the implementation of assistive exoskeletons, is the FP7 BioMot project [64] (Figure 1.10 example a). In this project, a novel modular powered lower-limb gait exoskeleton was developed. Since, this exoskeleton is a modular exoskeleton it can be used as a full lower-limb orthosis, a single-joint orthosis in any of the three joints, or a combination of any two joints.

Using this modularity property of this exoskeleton, K. Langlois *et al.* developed a customised interface, 3D printed with polylactic acid, PLA, reinforced with carbon fibres and epoxy resin, to be applied in the ankle foot model of the FP7 BioMot project [14] (Figure 1.10 example b and c). This Mater thesis' project will be, in some way, the continuation of K. Langlois *et al.* described idea.

## 1.8 Aim

The purpose of any research is to answer the questions imposed by science, therefore, the question that started this particular scientific quest was:

Is it possible to produce a 3D printed orthosis, embedded with 3D printed EMG and force sensors? And, will it improve the exoskeletons' performance?

To give an answer to this main question, some other questions had to be answered first:

1. Is it possible to produce working 3D printed EMG sensors?
2. Is it possible to produce working 3D printed force sensors?
3. Does the development of an algorithm, to study the deformation of the lower limb muscles, during the gait cycle, will help redesign the 3D printed exoskeleton's cuff?

The goal of this project will be to answer these three questions.

## 1.9 Outline

**Chapter 2: Development of 3D printed EMG sensors** - This chapter will provide the necessary information to design and 3D print an EMG sensor, which includes the dimensions and geometry of the sensors, the type of materials and which printing settings to use to print the EMG sensors. Besides the design and the fabrication process, it will also be shown how to access the EMG sensors and what are the expected results from this test.

**Chapter 3: Development of 3D printed force sensors** - To achieve the final design of the capacitance-based force sensor, it was mandatory first to develop a read-out mechanism. For this reason, this section of the project is divided into three parts: the setup development, to read the sensor, the construction of the actual 3D printed sensor and the testing of the sensor, along with the developed reading system. In the second subchapter, some considerations will be presented to facilitate the selection of the materials to use and the printing settings to print the sensors. The final subchapter will present a method to test the developed sensor and what are the expected results from it.

**Chapter 4: Study of the deformation of the lower Limb muscles** - In this stage, an algorithm will be presented with the primary purpose of analysing the deformation of the lower limb muscles, to help in future work the design of a more effective cuff for exoskeletons. The algorithm will be described along with all the steps required to achieve it and what are the expected results.

**Chapter 5: Conclusion and Future Work** - In the closing chapter, some final considerations will be taken about the work developed in this project. Also, the future work will be discussed.



# Chapter 2

## DEVELOPMENT OF 3D PRINTED EMG SENSORS

As it was determined in the “Introduction” chapter, one of the aims of this project is to produce a 3D printed EMG sensor, to be integrated into a 3D printed exoskeleton’s cuff, in order to optimize the exoskeleton’s control. Therefore, the goal of this chapter is to develop a 3D printed EMG sensor and access its efficiency in comparison to a regular commercialized one.

The following information will be sectioned into three main sections: the experimental protocol, the experimental results, and conclusions.

In the first section, the experimental protocol, all the materials, required to produce and test the 3D printed sensors, will be described along with the optimal 3D printing settings to produce the printed sensors. Besides the materials, a methodical explanation, will be given to describe the correct location to place the sensors, and the experimental procedure to access them. Along with the experimental procedure, there will also be an explanation on how to access, and what are the essential features to extract from the EMG signals, for correctly take the important conclusions.

In the second section, the experimental results will be compared and discussed to allow the proper conclusions to be taken, which will be displayed in the last section. In the conclusion’s section, besides the main conclusions, the experimental protocol will be reviewed, and some future work ideas will be exposed.

### 2.1 Experimental Protocol

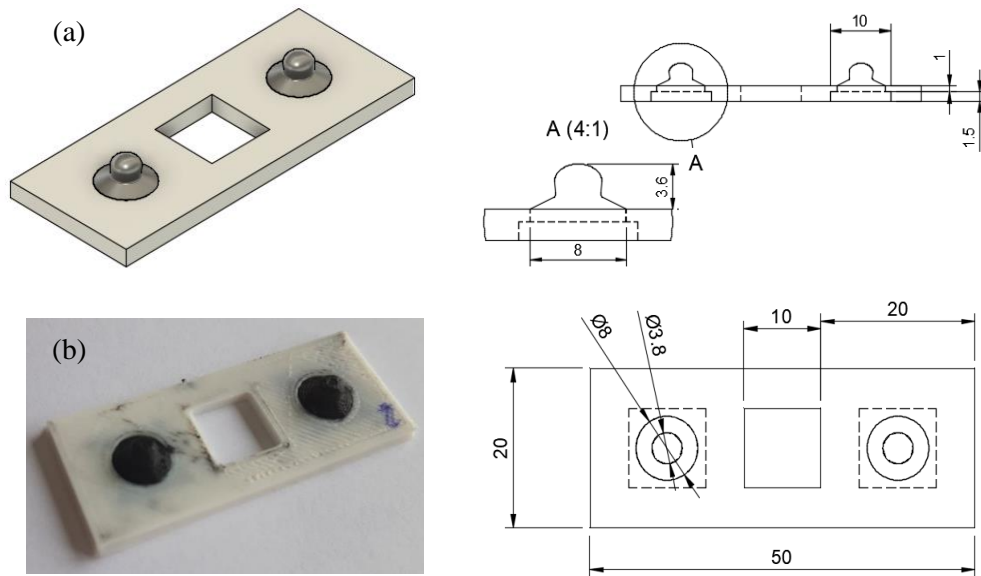
In the following section the experimental protocol is going to be presented, this includes the materials and methods required to produce the EMG sensor, as well as the experiments’ description used to access it.

#### 2.1.1 *Materials*

To perform this experiment, it is necessary first to design and produce the 3D printed EMG sensor (Figure 2.1), that requires:

- Conductive filament: Proto-pasta conductive PLA (Protoplant, Inc., USA)
- Non-conductive filament: Ultimaker TPU 95A (Ultimaker B.V., The Netherlands)
- 3D printer: Ultimaker 3 (Ultimaker B.V., The Netherlands)
- Fusion 360 (Autodesk Ink., United States of America)

- Ultimaker Cura 4.1.0 (Ultimaker B.V., The Netherlands)



The sensor's printing settings are presented in Table 2.1.

Table 2.1: Printing settings, used to print the 3D printed EMG sensor.

	Ultimaker TPU 95A	Proto-pasta conductive PLA
Layer height	0.2 mm	0.2 mm
Wall line count	4	3
Top layer	2	0
Bottom layer	2	“9999999”*
Infill density	100%	100%
Printing temperature	225°C	230°C
Build plate temperature	60°C	60°C
Print speed	20 mm/s	20 mm/s
Fan speed	100%	100%
Prime Blob	Enabled	Enabled
Build plate adhesion type	Skirt	Skirt
Prime tower	Enabled	Enabled
Nozzle type	AA 0.4	BB 0.4

\*It means that every printed layer is assumed to be a bottom layer.

To perform the experience, it is necessary:

- 4 Cleartrace™ RTL electrodes (CONMED, United States of America)
- ME6000 Biomonitor (Mega Electronics Ltd., Finland)
- EMG Preamplifier Cables, type MT-ME6P or MT-ME8P (Mega Electronics Ltd., Finland)

To analyse the experimental results the following programs were used:

- Matlab R2018b (The MathWorks, Inc., United States of America)
- R (Microsoft, United States of America)

### 2.1.2 Placement of the electrodes

In these experiments, the EMG sensors will be placed over the Biceps Brachii muscle. The choice of the muscle was based on the easiness of assessment and dimension of the muscle's cross-section. Also, when the sensor was being developed and tested there was no certainty to which exoskeleton the sensors were going to be integrated, so, for that reason, they were not tested in a lower limb muscle.

After choosing which muscle to access, it is essential to study the best location to place the EMG sensors, to obtain the best signals.

According to SENIAM project, surface ElectroMyoGraphy for the Non-Invasive Assessment of Muscles (an European concerted action in the Biomedical Health and Research Program of the European Union), the best location to place the EMG sensors to study the biceps brachii muscle is on the line between the medial acromion and the fossa cubit at 1/3 from the fossa cubit, in the direction of the line between the medial acromion and the fossa cubit (Figure 2.2). Regarding the reference or the ground electrode, it should be placed on/around the wrist [65]. In both cases, the ground electrode was an Ag/AgCl electrode.

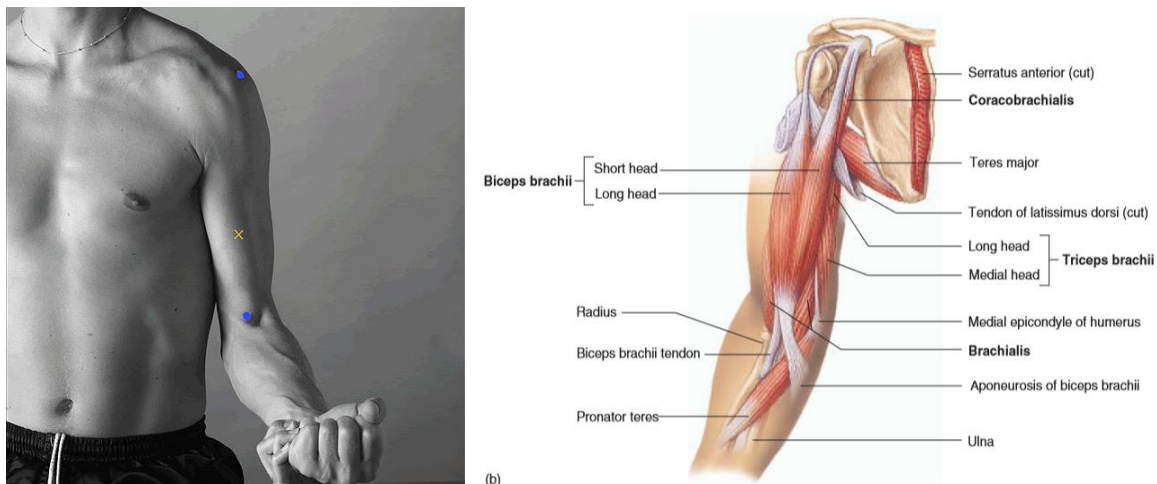


Figure 2.2: (a) Representation of the exact location where the EMG electrodes should be placed (yellow cross) [65]  
(b) Representation of the arm muscles [30]

### 2.1.3 Data collection

The skeletal muscles, which the Biceps Brachii muscle is an example of, can perform two types of voluntary contractions: the isometric, and isotonic contractions. From the Latin, the prefix “iso” means equal, therefore an isometric contraction implies the length of the muscles to remain constant,

while the tension during the contraction process changes. In opposition, the isotonic contraction always maintains the same tension, only the length of the muscle varies [29].

In this study, only the isometric contraction of the biceps brachii muscle is going to be accessed, this choice was based on the amount of information and reported studies on the two types of contractions.

The biceps brachii muscle is responsible for three important movements: the flexion of the shoulder; the elbow; and, the supination of the hand [29]. To better understand the variation in tension of an isometric contraction, the articulations should be “locked”, and the subject’s posture maintained constant throughout the data collection stage.

This experiment was performed in one healthy female subject after giving her informed consent.

According to some specific studies, to correctly access the biceps brachii muscle’s activity, the subject should be laid down on his back, so the shoulder is looked during the measurements. Regarding the arm, it should be horizontal and abducted 90°. The forearm should be at a 120° with the arm [39]. However, it was not possible for the subject to be in this posture while recording the EMG data. For this reason, the subject was seated on a chair, with the arm parallel to the torso and the forearm forming a 90° angle with the arm.

The experiment is divided into two parts: the first part destined to access the subject’s maximal voluntary contraction, MVC, and the second one to evaluate various levels of voluntary contraction when performing isometric contractions.

The first stage was based on the work of N. A. Dimitrova et al. [66], with the following steps:

1. 10 seconds without contracting the arm.
2. 3 seconds in maximal voluntary contraction (of the arm).
3. Rest for 3 minutes.
4. Repeat step 1, 2 and 3 another two times.

The second stage was based on A. Rainoldi and his research team [39]. In their study, the subjects were requested to perform several levels of muscular contraction where each level would correspond to a certain percentage of their MVC. However, in this experiment, the different levels of muscle contraction will be evaluated based on different weights placed on the subject’s hand. The change in the procedure was related to the higher accuracy when performing different measurements when the subject has a weight in his hands, then when asked to contract a certain percentage of his MVC.

1. Place 1 kg weight in the subject’s hand for 30 seconds.
2. Rest for 5 minutes.
3. Place 2 kg weight in the subject’s hand for 30 seconds.
4. Rest for 5 minutes.
5. Place 3 kg weight in the subject’s hand for 30 seconds.
6. Rest for 5 minutes.

#### ***2.1.4 EMG analysis***

After acquiring all the EMG data, the captured signals must be filtered. A high-pass, 3<sup>rd</sup> order Butterworth filter, with a corner frequency of 20 Hz must be applied, so the baseline and movement artefact noises are eliminated from the EMG signals. After, to reject the area of the signal where the amplitude of the noises surpasses the EMG signal, a low-pass, 3<sup>rd</sup> order Butterworth filter, with a corner frequency of 400 Hz is applied. Lastly, a 50 Hz notch filter must be applied to phase out the outer net interference. These frequency values, as well as the type of filters, used to filter the signal were provided by [31], [34].

With the signal filtered, the MNF, MDF and the RMS values of the respective signals must be calculated to allow the comparison between the two types of EMG sensors.

### ***MNF and MDF calculations***

The first step to obtain the MNF and MDF of the collected EMG signals is to divide the signal into different time segments, called epochs, and apply to each epoch a windowing technique. In the study performed by R. Merletti *et al.* and his team [38] with the aim of understanding the effects of the epoch duration and type of windowing on the MNF and MDF calculation, they were able to conclude that, rectangular windowing is preferable to smoother windowing, and the coefficient of variation increases with the decrease of the epoch's duration.

For this reason, it was chosen a rectangular non-overlapping window, with an epoch of 1 second. The non-overlapping window was chosen because the application of an overlapping window can be considered as the equivalent of smoothing the spectrum [39].

From the divided signal, a frequency spectrum analysis must be executed, which can be achieved by the application of a 512-points' short term Fourier transform (STFT) for each epoch of the filtered EMG signals [36], [41]. With the power spectral density,  $P(f)$ , calculated, the MNF and MDF can be computed, for each epoch, by the application of the following equations [41]:

$$MNF = \frac{\int_0^{f_0} f P(f) df}{\int_0^{f_0} P(f) df} \quad [3.1]$$

$$\int_0^{MDF} P(f) df = \int_{MDF}^{f_0} P(f) df \quad [3.2]$$

Where  $f_0$  is the upper limit frequency of the  $P(f)$ , which corresponds to half of the sampling rate.

### ***RMS calculation***

To calculate the signals' RMS, the filtered signal has to be divided the same way it is divided to calculate the MNF and MDF, which means divide the signal into 1 second epochs with a non-overlapping rectangular windowing technique applied to each epoch.

With the epochs defined, the RMS is calculated for each epoch by the application of the following equation [42]:

$$RMS = \sqrt{\frac{1}{N} \sum_{i=1}^N x_i^2} \quad [3.3]$$

Where  $x_i$  is the  $i^{\text{th}}$  sample of a signal and  $N$  is the number of samples in each epoch.

## **2.2 Experimental Results**

After acquiring the EMG signals of the different experimental stages and filtering them, the MNF, MDF and RMS were computed.

As previously reported, the spectral features only access the muscles' fatigue and not the variation of the diverse levels of muscle contraction, for this reason, the MNF and MDF values were only

calculated for the EMG records acquired in the second stage of the experiment. The results are displayed in Figure 2.3, for the MDF values, and Figure 2.4, for the MNF values. In both figures, the EMG signals, obtained with the commercial sensors, are represented in blue, and the EMG signals, obtained with the 3D printed sensors, in orange. Each value is represented along with the respective associated error.

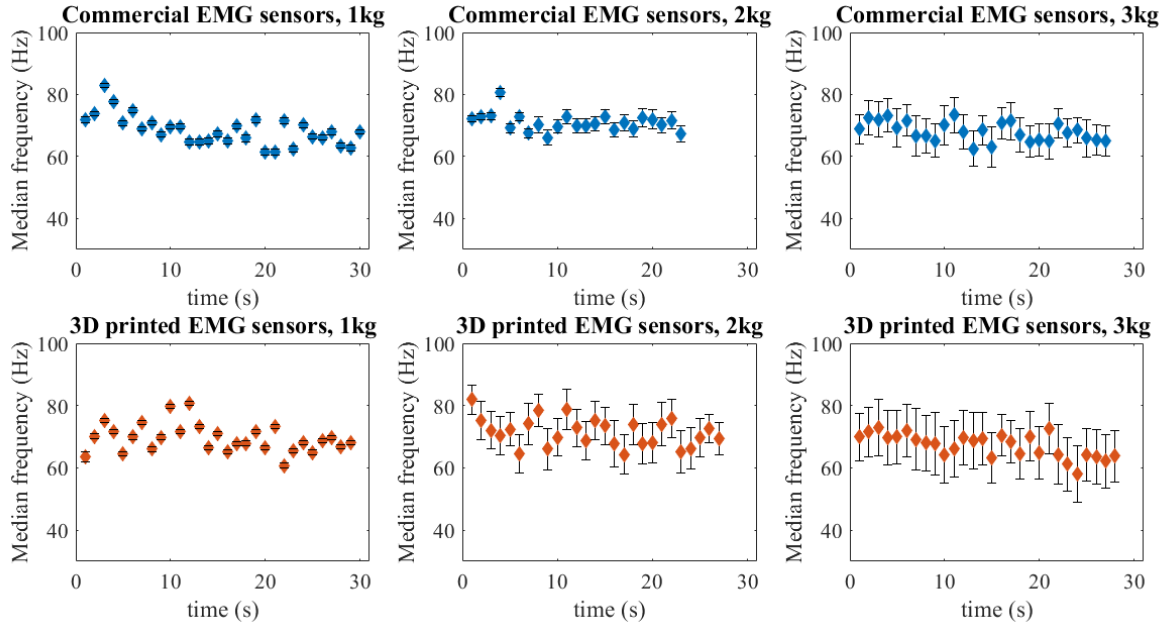


Figure 2.4: MDF calculations for EMG records corresponding to different levels of contractions, induced by the support of different weights, 1kg, 2kg and 3kg. The MDF values represented in blue correspond to the measures performed with the commercial EMG sensors and the MDF values represented in orange to the measures performed with the 3D printed EMG sensors.

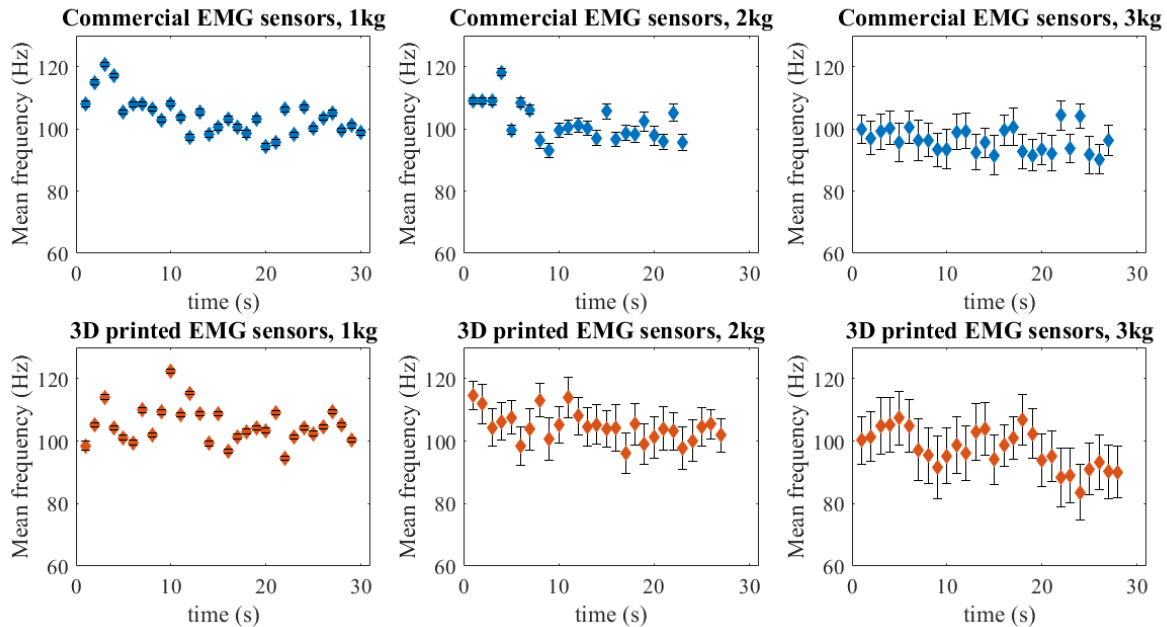


Figure 2.3: MNF calculations for EMG records corresponding to different levels of contractions, induced by the support of different weights, 1kg, 2kg and 3kg. The MNF values represented in blue correspond to the measures performed with the commercial EMG sensors and the MNF values represented in orange to the measures performed with the 3D printed EMG sensors.

According to the formulated hypothesis, in the previous chapters, the MNF and MDF values, should have a tendency to decrease with the increase of fatigue, hence, with the increase of the supported weight, by the subject, the accentuation of the decrease, should also increase. Therefore, when analysing Figure 2.4 and Figure 2.3, a linear tendency should be spotted, specially for the records registered when the subject was holding the 3kg weight, however the tendency to decrease is only evident for the values registered with the 3D printed EMG sensors.

To confirm if there is indeed a tendency for the MNF and MDF values to decrease with the increase of fatigue, a linearization of the values was calculated. The results are presented in Table 2.2.

Table 2.2: Linearization of the MNF and MDF values calculated for the EMG recording of the second experiment

Experiments		MNF values			MDF values		
		Equation	R <sup>2</sup>	p-value	Equation	R <sup>2</sup>	p-value
Commercial sensors	1 kg weight	$y = -0.43x + 110.70$	0.39	<0.001	$y = -0.34x + 73.71$	0.38	<0.001
	2 kg weight	$y = -0.50x + 107.93$	0.32	0.004	$y = -0.13x + 72.52$	0.09	0.150
	3 kg weight	$y = -0.13x + 98.17$	0.07	0.180	$y = -0.18x + 70.70$	0.23	0.010
3D printed sensor	1 kg weight	$y = -0.13x + 107.02$	0.03	0.330	$y = -0.14x + 71.56$	0.07	0.150
	2 kg weight	$y = -0.30x + 108.86$	0.26	0.0071	$y = -0.20x + 74.20$	0.12	0.078
	3 kg weight	$y = -0.50x + 104.50$	0.42	<0.001	$y = -0.31x + 71.68$	0.47	<0.001

It is possible to understand from Table 2.2, that only half of the results present a linear tendency (all the results with R<sup>2</sup> above 0.2). This was the expected behaviour since for the readings were the subject was carrying the lightest weight there was almost no fatigue. Hence, it is reasonable not to present a linear trend, and then, with the weight increase, a linear tendency would appear, decreasing the slope of the linear equation. This behaviour was registered for the EMG data, collected with the 3D printed sensors, not for the commercial sensors, which showed the opposite expected behaviour.

Different phenomenon may justify the opposite results between the records acquired with commercial sensors and 3D printed sensors. The first aspect to have in consideration is the position of the arm not being identical for every experiment, resulting in a difference in the level of muscular contraction for the same carried weight. The second factor to have in consideration is the shoulder not being locked, which may also influence the level of contraction of the muscles, resulting in a difference in the fatigue level. Finally, it is important to mention that the readings with the commercial sensors were the first ones to be acquired and only after the recordings obtained with the 3D printed sensors, so the muscles of the subject were at different levels of fatigue, influencing once more the final results. Also, there is the possibility of the values of the weights, or the time the weights are carried by the subject, to not induce enough fatigue into the muscles to significantly alter the MDF and MNF results.

Besides the described circumstances, it is also important to refer that the sensors were not in the same conditions since it is impossible to place them in the exact location where the previous sensors were. Also, factors like sweatiness of the skin and the electrodes' position shifting through the experiment may influence the results and induce various levels of noise.

Lastly, it is also important to mention that it was considered a good result a linear fit with an  $R^2$  above 0.2 because it is not supposed for the values to present a linear behaviour but a tendency to decrease and for that reason, the  $R^2$  does not have to be extremely high.

Regarding the amplitude analysis, as explained previously, the EMG signals' amplitude is mainly affected by the intensity of the muscles' contractions, in opposition to the muscles' fatigue over time, which is almost neglectable. For this reason, after calculating the RMS values for each epoch, the mean of the RMS values was calculated for each record, including the MVC records.

Since the variation in amplitude is mainly due to the variation in the muscles' contraction intensity, all the values from the second stage experiment are going to be normalized with reference to the highest MVC's RMS recorded value. The results are presented in Figure 2.5. The RMS values in blue correspond to the records registered with the commercial EMG sensors, and the orange values to the 3D printed EMG sensors.

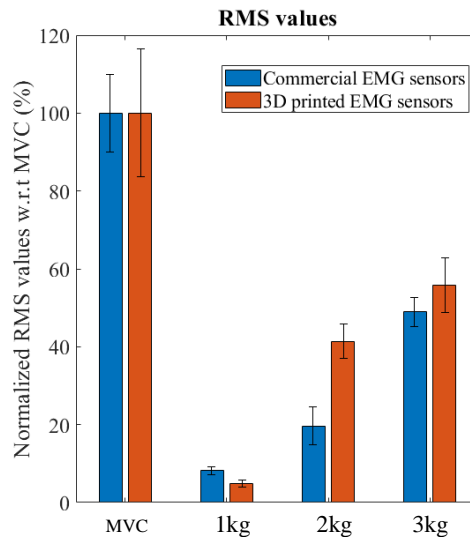


Figure 2.5: RMS mean calculations for EMG records corresponding to different levels of contractions, induced by the support of different weights, 1kg, 2kg and 3kg, and by the MVC. The RMS values represented in blue correspond to the measures performed with the commercial EMG sensors and the RMS values represented in orange to the measures performed with the 3D printed EMG sensors.

Analysing the RMS values, reported in Figure 2.5, it is possible to understand from Figure 2.5, there is a clear difference between the MVC values and the values from the remaining contractions. Also, the RMS values increase with the increase of the weight the subject had to support, which was the expected behaviour (described in the “Introduction” chapter).

Comparing the RMS results for the two types of sensors, they are similar, when the subject was supporting 1 and 3 kg, on the contrary, the values for the 2-kg supported weight differ substantially. This particular result may also be justified by the phenomenon described previously to explain the different outcomes for the MNF and MDF values. However, although there was a significant difference between the two RMS values, they were still higher than the corresponding 1 kg RMS value and lower than the 3 kg RMS value, which was the expected.

## 2.3 Conclusion

From the presented results, it is possible to give a response to the first of the three questions, presented in the “1.8 Aim” subchapter, to which this project intended to find an answer for. Therefore, for the question: “Is it possible to produce working 3D printed EMG sensors?”, the answer is yes, it is possible to 3D printed EMG sensors that indeed work as EMG sensors.

Nonetheless, only one subject was tested, so in future work, these sensors should be tested in a higher number of subjects, to understand which types of limitations they have. Also, for the same subject, the same experiment has to be performed at least three times to improve the result’s accuracy.

Another crucial factor to be understood, in future work, is how the sensor’s efficiency varies with the variation of external factors like room temperature and humidity. Also understand how the sensors’ output changes with the change in subjects, more precisely, if the percentage of fat tissue between the skin and the muscles influences the readings, the sweatiness of the skin, and also if it is possible to measure the EMG signals from smaller muscles.

In conclusion, it is necessary to perform an intensive characterisation of these 3D printed EMG sensors, before implementing them into an exoskeleton.



# Chapter 3

## DEVELOPMENT OF 3D PRINTED FORCE SENSORS

In regard to the information presented in the “Introduction” chapter, monitoring the user’s comfort, while maintaining him safe, could be a strategy to maximise the exoskeleton’s efficiency. This can be achieved by the incorporation of 3D printed force sensors into the exoskeleton’s interface.

Therefore, the goal of this section is to produce, and access 3D printed capacitance-based force sensors to be integrated into an exoskeletons’ interface. The evaluation of the printed sensors will consist on registering and analysing the sensor’s output, when a force is applied. Besides developing the printed sensor, it is also necessary to develop an electronic system, to capture the capacitance variations of the sensor and send the information to a computer, where the signal can be analysed.

This chapter is divided into three parts: the development of the sensor’s reading system, the production and characterization of the 3D printed sensor, and the testing of the sensor with the developed set-up reading system.

### 3.1 Development of the sensor’s reading system

When a capacitor is in series with a resistor, as it is represented in Figure 3.1, it is possible to calculate the capacitor’s voltage in time,  $v(t)$ , by the application of the following equation:

$$v(t) = V_S + (V_0 - V_S)e^{-\frac{t}{RC}} \quad [3.1]$$

Where,  $V_S$ , corresponds to the value of a constant dc voltage source, that is feeding the circuit,  $V_0$ , to the initial voltage on the capacitor, and  $R$  and  $C$ , to the resistance and capacitance of the circuit, respectively. Because the goal of this experiment is to determine the capacitance of an unknown capacitor, Equation 3.1 can be rewritten:

$$C = -\frac{t}{\ln\left(\frac{v(t) - V_S}{V_0 - V_S}\right)R} \quad [3.2]$$

If  $V_S$ ,  $V_0$ ,  $v(t)$ , and  $R$ , are set to be constant, the capacitor’s capacitance will only depend on the time,  $t$ , it takes for the capacitor to reach the pre-specified voltage,  $v(t)$ .

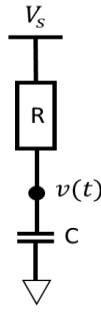


Figure 3.1: Resistor in series with a capacitor

Based on this concept and in the set up developed by [67], an Arduino code was written, and an electronic set up system developed. The idea is to use an Op-Amp to work as a comparator. In a comparator, two different analogue voltages are presented to the non-inverting and inverting terminals of the Op-Amp. The output signal will reflect the highest voltage value registered by the two.

If a constant voltage,  $V_{REF}$ , is connected to the inverting terminal, which can be achieved by a voltage divider, and an RC circuit to the non-inverting terminal, every time the capacitor's voltage surpasses the reference voltage the output signal changes from a smaller value to a higher one.

Knowing that when  $t = 0s$  the capacitor is discharged,  $V_0 = 0V$ , it is possible, with the help of an Arduino, to register the time it takes for the capacitor to charge until it reaches the reference voltage, due to the change in the output's voltage, which will allow the calculation of the capacitor's capacitance.

When designing this type of circuit, there are two key factors to have in consideration: the resistor's value,  $R$ , and the voltage reference,  $v(t)$ . Both parameters will influence the time it will take for the capacitor to reach the desired voltage, and since the Arduino has a limited sampling rate, the longer it takes for the capacitor to charge or to reach the desired voltage, the more accurate the measurement will be.

With this concept in mind the resistor chosen for the RC circuit was  $1M\Omega$  and the voltage reference  $3.5V$  which was achieved by a voltage divider formed by two different resistors:  $4.7\text{ k}\Omega$  and  $2.2\text{ k}\Omega$ .

The electronic set up is represented in Figure 3.2.

To make shore the capacitor is completely discharged, before every measurement, pin 11 from the Arduino is set as a ground and pin 9 switch from "input" mode to "output" mode. When the Arduino pins are set to work in the "input" mode, a  $10\text{ M}\Omega$  resistance is associated to them, so the amount of current that enters the pin is neglectable, not interfering with the voltage measurements. On the contrary, when the Arduino pins are set to "output" mode, the pin presents almost no resistance to the current's passage, making the majority of the current passing through the pin, enabling the capacitor to discharge.

After the discharging process, the charging process begins. Pin 11 from the Arduino is set to be a  $5V$  dc source supply and the capacitor starts charging until it reaches its maximum, after a certain period of time the discharging process starts again.

To calculate the capacitance, when pin 11 changes from  $0V$  to  $5V$  a timer starts counting the time. An interrupt function is attached to pin 3 so when the output of the set-up changes from  $-VCC$  to  $+VCC$  (due to the voltage of the capacitor surpassing the reference voltage) the timer stops counting. With the application of the equation 4.2 it is possible to finally deduce the unknown capacitor's capacitance.

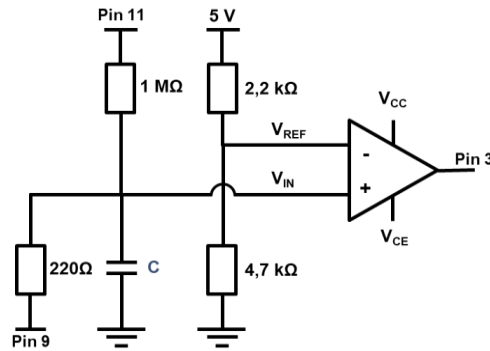


Figure 3.2: Electronic system responsible for connecting the sensor to the reading system.

### 3.1.1 Experimental Protocol

In the following section, the experimental protocol will be exposed, this includes the materials required to build the set-up system, the methods to test the presented measurement system and which type of analysis must be done to the records to validate the correct functionality of the entire system.

#### *Data collection and materials to use*

To build the measurement system, it is necessary:

- Arduino Uno (Arduino, Italy)
- USB cable
- Computer (320-15ISK Laptop (ideapad) (Lenovo Group Ltd, China))
- CoolTerm program [70]
- 4.7 kΩ Resistor (Velleman, Belgium)
- 2.2 kΩ Resistor (Velleman, Belgium)
- 1M Ω (Velleman, Belgium)
- 220 Ω Resistor (Velleman, Belgium)
- Op-Amp LM324N
- Breadboard

To validate the set up described in the previous section, several capacitors, with different capacitances are going to be measured for 30 seconds each, in 3 separated times, with the described set up. The capacitors that will be used are:

- 0.006 nF capacitor
- 0.008 nF capacitor
- 0.012 nF capacitor
- 0.020 nF capacitor
- 0.030 nF capacitor
- 0.040 nF capacitor
- 0.063 nF capacitor

To analyse the experimental results the following programs were used:

- Matlab R2018b (The MathWorks, Inc., United States of America)
- R (Microsoft, United States of America)

### Set-up analysis

From Equation 3.2, it is expected for the time readings, to increase linearly with the increase of the capacitor's capacitance. Also, it is expected for the readings to be the same if the capacitance is not changed.

To validate the presented hypotheses, the first statistical analysis should be to determine if there is a significant difference between the readings obtained with the same capacitor. Therefore, for every three measurements of each capacitor a Kruskal-Wallis test will be performed.

After understanding if the readings for the same capacitor are significantly different or not, a linearization of all the values should be performed to understand if indeed the capacitor's charging time changes linearly with the capacitor's capacitance.

### 3.1.2 Results

Before measuring the capacitance with the set-up system, described in the previous section, all the components, as well as the parameters present in Equation 3.2,  $V_S$  and  $v(t)$ , were measured with a multimeter. The results are exposed in the following table, Table 3.1:

Table 3.1: Measurement of the parameters.

Measurement	Resistor 1 (k $\Omega$ )	Resistor 2 (k $\Omega$ )	Resistor 3 (k $\Omega$ )	Resistor 4 (k $\Omega$ )	$V_S$ (V)	$v(t)$ (V)
1 <sup>st</sup>	2.180 $\pm$ 0.001	4.647 $\pm$ 0.001	990 $\pm$ 1	0.2193 $\pm$ 0.0001	5.067 $\pm$ 0.001	3.433 $\pm$ 0.001
2 <sup>nd</sup>	2.180 $\pm$ 0.001	4.650 $\pm$ 0.001	990 $\pm$ 1	0.2192 $\pm$ 0.0001	5.068 $\pm$ 0.001	4.434 $\pm$ 0.001
3 <sup>rd</sup>	2.179 $\pm$ 0.001	4.648 $\pm$ 0.001	990 $\pm$ 1	0.2192 $\pm$ 0.0001	5.068 $\pm$ 0.001	3.433 $\pm$ 0.001
Mean	2.180 $\pm$ 0.001	4.648 $\pm$ 0.002	990 $\pm$ 1	0.2192 $\pm$ 0.0001	5.068 $\pm$ 0.001	3.433 $\pm$ 0.001

After measuring the parameters, presented in Table 3.1, with the developed set-up system, the charging time of each capacitor was registered. With the registered values, the Kruskal-Wallis test was applied to the three measurements of each capacitor. From the test it was possible to concluded that at a significant level of 99% the results are not significantly different from each other (in respect to the median of each sample), which was the expected results, since for the same capacitor, the same capacitance should be read.

After the Kruskal-Wallis test, a linear regression test is performed, to access the linear correlation between all the obtained values. From this test was possible to conclude that there is indeed a positive linear relation between the values ( $y = 1.05 \times 10^3 x + 77.56$ ;  $R^2 = 0.98$ ;  $p < .0001$ ), which was again the expected result.

With the statistical analysis completed, the mean capacitance of each measurement can be calculated, along with the associated error. The capacitance was determined by the application of the Equation 3.2, and the associated error by the following equations (3.3 - 3.7). The results are summarized in Table 3.2 and showcased in Figure 3.3.

$$\Delta C = \left| \frac{\partial C}{\partial t} \right| \Delta t + \left| \frac{\partial C}{\partial R} \right| \Delta R + \left| \frac{\partial C}{\partial v(t)} \right| \Delta v(t) + \left| \frac{\partial C}{\partial V_s} \right| \Delta V_s \quad [3.3]$$

$$\frac{\partial C}{\partial t} = - \frac{1}{\ln \left( \frac{v(t) - V_s}{V_0 - V_s} \right) R} \quad [3.4]$$

$$\frac{\partial C}{\partial R} = \frac{t}{\ln\left(\frac{v(t) - V_s}{V_0 - V_s}\right) R^2} \quad [3.5]$$

$$\frac{\partial C}{\partial v(t)} = \frac{t}{(v(t) - V_s) \times \left(\ln\left(\frac{v(t) - V_s}{V_0 - V_s}\right)\right)^2 \times R} \quad [3.6]$$

$$\frac{\partial C}{\partial V_s} = -\frac{t \times (v(t) + V_0)}{(v(t) - V_s) \times (V_0 - V_s) \times \left(\ln\left(\frac{v(t) - V_s}{V_0 - V_s}\right)\right)^2 \times R} \quad [3.7]$$

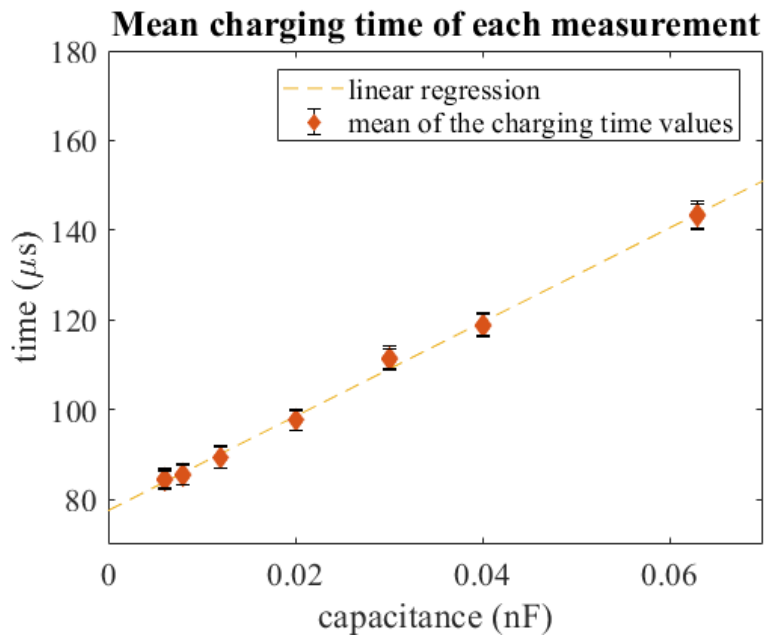


Figure 3.3: Representation of the mean charging time values in respect to the capacitor's capacitance in conjunction with the linear tendency of the values

Table 3.2: Experimental results for the capacitance

Theoretical Capacitance (pF)	Trial	Time ( $\mu$ s)	Capacitance (pF)	Capacitance (pF)
6	1 <sup>st</sup>	$84.50 \pm 2.11$	$74.76 \pm 1.82$	$74.80 \pm 1.83$
	2 <sup>nd</sup>	$84.72 \pm 2.22$	$74.96 \pm 1.92$	
	3 <sup>rd</sup>	$84.42 \pm 2.03$	$74.69 \pm 1.75$	
8	1 <sup>st</sup>	$85.37 \pm 2.14$	$75.52 \pm 1.85$	$75.62 \pm 1.91$
	2 <sup>nd</sup>	$85.68 \pm 2.32$	$75.81 \pm 2.00$	
	3 <sup>rd</sup>	$84.36 \pm 2.17$	$75.52 \pm 1.87$	
12	1 <sup>st</sup>	$89.40 \pm 2.47$	$79.10 \pm 2.13$	$79.05 \pm 2.06$
	2 <sup>nd</sup>	$89.42 \pm 2.36$	$79.11 \pm 2.04$	
	3 <sup>rd</sup>	$89.23 \pm 2.34$	$78.95 \pm 2.02$	
20	1 <sup>st</sup>	$97.81 \pm 2.43$	$86.54 \pm 2.09$	$86.46 \pm 2.03$
	2 <sup>nd</sup>	$97.61 \pm 2.29$	$86.36 \pm 1.97$	
	3 <sup>rd</sup>	$97.75 \pm 2.34$	$86.48 \pm 2.01$	
30	1 <sup>st</sup>	$111.34 \pm 2.33$	$98.51 \pm 2.00$	$98.59 \pm 2.04$
	2 <sup>nd</sup>	$111.67 \pm 2.51$	$98.80 \pm 2.15$	
	3 <sup>rd</sup>	$111.30 \pm 2.29$	$98.47 \pm 1.96$	
40	1 <sup>st</sup>	$118.72 \pm 2.46$	$105.04 \pm 2.11$	$105.13 \pm 2.14$
	2 <sup>nd</sup>	$119.00 \pm 2.54$	$105.29 \pm 2.18$	
	3 <sup>rd</sup>	$118.76 \pm 2.48$	$105.07 \pm 2.12$	
63	1 <sup>st</sup>	$143.16 \pm 2.78$	$126.66 \pm 2.38$	$126.84 \pm 2.53$
	2 <sup>nd</sup>	$143.34 \pm 3.05$	$126.82 \pm 2.62$	
	3 <sup>rd</sup>	$143.61 \pm 3.01$	$127.05 \pm 2.58$	

### 3.1.3 Conclusion

It is possible to understand, from the values presented in the previous sections, that the capacitance obtained by experimental methods is not identical to the theoretical capacitance values, suggested by the manufactures. However, from the statistical analyses it was possible to conclude that the charging time of the capacitors changed linearly with the variation in capacitance, and for all the measurements performed with the same capacitor, the charging time was almost identical, as it was suggested in the “Development of the sensor’s reading system” subsection. These results indicate that the absolute values are only different, from the theoretical values, due to some factors, that influence the measurements, that are not being considered in the equations presented above.

One of the factors that is not being considered in the equations and influences the results is the resistance associated to pin 9 not being infinite when the pin is set as input. Typically, the resistance is considered to be infinite because the resistors usually used have low values, when compared to the input resistance (10 M $\Omega$ ). However, because the resistor used in the RC circuit is 1 M $\Omega$ , the electrical current that passes through this resistance does not go in totality to the capacitor, it is divided by the capacitor and the input resistance, influencing the charging time of the capacitor.

Also, besides the resistance, there is a capacitance associated to the Arduino that is usually neglectable. However, because the capacitors that are being measured by the set-up have a capacitance in the order of pF, it can also not be ignored when calculating the capacitor’s capacitance.

Another crucial factor to have in consideration is the Op-Amp configurations. The Op-Amp used in this experiment was an LM324N, this Op-Amp has an input offset voltage of 2 mV [68], when ideally

should be 0. This means that the comparator does not change its output when the capacitor's voltage surpasses the reference voltage, it changes when there is a 2mV difference between the two inputs, leading to a measurement error.

Besides the input offset voltage, it is also essential to have in consideration the response time of the Op-Amp. Ideally, when there is a voltage change in the Op-Amp's input, the output should change instantaneously, however, in reality, it does not happen. In this case, it takes 5  $\mu$ s to change the outputs' voltage from the initial value to the final value [68], which leads as well to an error in the charging time of the capacitor.

Finally, the capacitance that was considered to be the real measurement it is not, since there is a difference between the value indicated by the manufacturer and the actual value.

In conclusion, although there are considerable factors that influence the calculation of the capacitance, the set-up, presented in this experiment, indeed measures the changes in capacitance and, with an initial calibration, it is possible to predict the value of an unknown capacitance.

## **3.2 Construction of the 3D printed sensor**

As it was described in the "Theoretical framework" chapter, a capacitance-based force sensor is formed by three layers, one flexible non-conductive layer, the dielectric, that separates two conductive plates. Because the dielectric is flexible, when a force is applied to the sensor, the distance between the two plates will diminish. This variation will be inversely proportional to the variation in capacitance, Equation 2.2, allowing, with the proper measurement system, the force, that is being applied to the sensor, to be calculated.

Based on the previous information, to 3D print a capacitive sensor, it is necessary two types of materials: a conductive material and a non-conductive, flexible material. However, with the filaments currently on the market, it is impossible to 3D print a conductive material, the only option is to print a semi-conductive material.

To the author's knowledge there are only four semi-conductive materials on the market: PI-ETPU 95-250 Carbon Black (Palmiga Innovation, Sweden), Electrifi Conductive Filament (Multi3D, USA), Conductive Graphene PLA Filament (Black Magic 3D, USA) and Proto-pasta conductive PLA (Protoplant, Inc., USA). Therefore, the choice of the semi-conductive material, to print the two conductive plates will be between the four indicated filaments.

Considering Equation 2.2, the capacitance of the sensor is directly proportional to its surface area. Because the measurement system has a reading range and the presented filaments are not perfect conductors, the sensors must have a minimal area. Since the final goal of the project is to incorporate the capacitive sensors into a cuff of an exoskeleton, and the sensor's dimensions cannot be as small as possible, it is necessary for the conductive plates, as for the dielectric, to be flexible to easily adapt to the cuff. With this imposition, bought Conductive Graphene PLA Filament and Proto-pasta conductive PLA are not suitable for the purpose of this project since they are not flexible.

Regarding the first two semi-conductive filaments the second one is the most conductive one, however, according to the critics, the first one is easier to print, and, for that reason, the chosen filament for this project, and used to 3D print the capacitive sensors, was the PI-ETPU 95-250 Carbon Black.

After selecting the filament to 3D print the conductive plates, it is necessary to choose which filament to use to 3D print the dielectric. In the next section, several filaments with different infill percentages, will be tested as dielectrics to understand which one is the most suitable for the construction of a capacitive sensor.

### 3.2.1 Assessment of non-conductive 3D printing filaments to be used as dielectric

To assess the potential of the non-conductive filaments as the sensor's dielectric, they were tested as part of a capacitance-based force sensor, in other words, for each tested non-conductive filament a force sensor was 3D printed. To make sure all the filaments were accessed evenly, all the sensors produced in this stage had the same dimensions, regardless of the type of materials used for the dielectric, Figure 3.4. Besides the 3D printed force sensors, a sensor with silicone as dielectric was also produced with different heights to better understand how the dielectric's height and flexibility would influence the variation in capacitance with the application of a force.

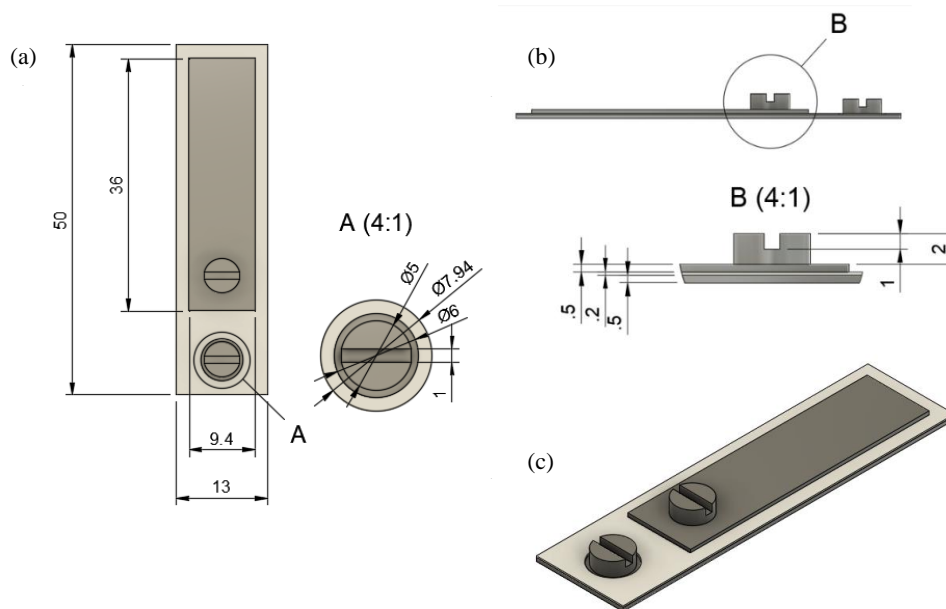


Figure 3.4: (a) Top view of the 3D printed sensor, (b) side view of the 3D printed sensor, (c) representation of the 3D printed sensor

All the sensors were designed in the Fusion 360 (Autodesk Ink., United States of America) program and printed with an Ultimaker 3 (Ultimaker B.V., The Netherlands). To import the sensor's design into the printer and to define how the printer is going to 3D print the sensors, the Ultimaker Cura 4.1.0 (Ultimaker B.V., The Netherlands) was used. To establish the connection between the sensor and breadboard, two jumper wires were welded to each prominence of the sensor.

The evaluation of the sensors was performed with the application of different weights over the sensors. To register the capacitance, the same set up described in the previous experiment was used, however, instead of using the timer of the Arduino, an oscilloscope was used to calculate the capacitor's charging time.

Since the testing of the non-conductive filaments was conducted through an extended period of time, the chosen weights to test the sensors, as well as the experimental protocol, suffered some alterations. For the first three accessed filaments it was used 1kg, and 2kg weights and their placement was not sequential, meaning that there was a resting time between the application of the loads. In the tests

that followed, the weights were changed to 0.5kg and 1kg, and the sensors were tested sequentially, without any breaks in between the application or removal of the weights. Although there were some variations, they did not influence the final conclusions.

To simplify the reading of the report, in the following sections only the conclusions of the sensor’s experiments are going to be described. The order of the materials that are going to be presented, was based on the time sequence they were evaluated, meaning the first material to be described was the first one to be tested and so on, until the last presented one.

### **Ultimaker TPU 95A**

The Ultimaker TPU 95A filament was the first one to be used and accessed as a capacitor’s dielectric. TPU stands for thermoplastic polyurethane, which the Alliance for Polyurethane Industry (API) describes as the “bridging gap between rubbers and plastics”, since it combines the high elasticity of the rubbers with high abrasion resistance, characteristic of the plastics [69].

The important mechanical properties of Ultimaker TPU 95A are presented in the next table, Table 3.3 [70]:

Table 3.3: Mechanical properties of Ultimaker TPU 95A

Tensile Modulus	Elongation at yield	Hardness
26 Mpa	55%	95 (Shore A)

After producing and testing the sensor with Ultimaker TPU95A as dielectric, Figure 3.5, and registering the charging time of the sensor in the different pressure circumstances, it was concluded that the captured values changed randomly, not existing a clear dependence on the sensor’s output with the applied weights.

One simple justification for this phenomenon is the possibility of this material, Ultimaker TPU 95A, not being flexible enough to significantly deform with the pressures that are being applied, not causing a variation in capacitance. To test this theory, a second sensor was produced, but instead of using the Ultimaker TPU 95A as dielectric, a silicone layer was used.

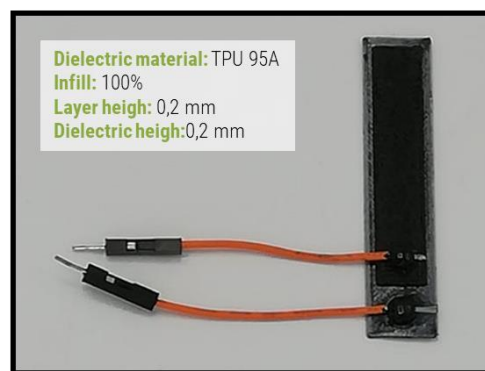


Figure 3.5: Capacitance-based sensor with Ultimaker TPU 95A as dielectric

### **Silicone**

In opposition to all the other sensors, the capacitive sensor with silicone as dielectric was not produced with a multi-material printing technique, but through a hybrid approach. In this 3D printing technique, printed and non-printed parts are combined to form the desired object [50]. In this case, the

two conducting plates were 3D printed separately and the silicone layer produced with 3D printed moulds.

Besides changing the fabrication process, the height of the dielectric in this sensor was also adjusted. Three different silicone dielectrics with three different heights, 0.5, 1 and 2 mm, were produced and tested. The reason, for the change in the dielectric's height was the impossibility to produce silicone sheets of 0.2 mm height from 3D printed moulds. Regarding the three different dielectrics, they were produced to test the influence of the dielectric's height into the variation in capacitance due to a variation of an applied force.

In this experiment, in opposition to the values registered in the previous experiment, with Ultimaker TPU 95A as dielectric, there were clear differences between applying and not applying the weights to the sensor, and it was even possible to distinguish when applying a weight of one kilo or two kilos. Also, the sensor that showed the best results was the sensor with the dielectric with 0.5 mm height, Figure 3.6.

With the results from this trial, the hypothesis suggested in the previous section was confirmed, indeed the inefficiency of the previous sensor was related to its dielectric flexibility.

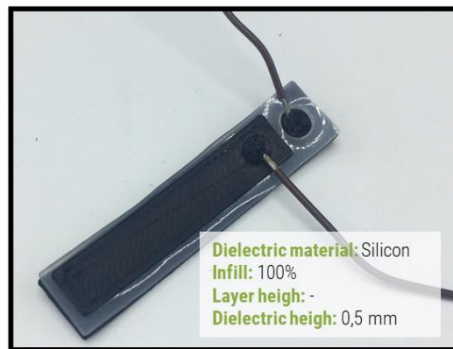


Figure 3.6: Capacitance-based sensor with silicone as dielectric

### ***NinjaFlex 85A***

From the results of the two previous experiments, it was possible to come to the conclusion that the flexibility of the sensor's dielectric is a key factor to its proper functioning, and the hardness of the Ultimaker TPU 95A is not suitable for the goal of this project.

Therefore, the solution for the lack of flexibility of the dielectric was to use another type of material, a material more flexible and with a lower associated hardness to 3D print the sensor's dielectric. The chosen material was the NinjaFlex 85A.

The NinjaFlex 85A, like the Ultimaker TPU 95A, is a TPU, however, it has a slightly lower hardness, of 85 (shore A), the mechanical properties of this material are presented in Table 3.4 [71].

Table 3.4: Mechanical properties of NinjaFlex 85A

Tensile Modulus	Elongation at yield	Hardness
12 MPa	65%	85 (Shore A)

Although the NinjaFlex 85A is a more flexible material, when compared to the Ultimaker TPU 95A, the results were similar, it was not possible to distinguish when a weight was being applied or not to the sensor. In conclusion, the NinjaFlex 85A was not suitable for the purpose of the project.

## ***REC RUBBER***

In recapitulation, the Ultimaker TPU 95A and the NinjaFlex 85A were tested in the previous trials and were considered not suitable for the purpose of the project, since the sensors produced with these materials were not able to distinguish different applied pressures. However, the solution to the problem was kept the same: use another type of material, to 3D print the sensor's dielectric, a material more flexible and with a lower associated hardness.

The third chosen material to be 3D printed as the sensor's dielectric was the REC RUBBER. Its mechanical properties are presented in Table 3.5 [72].

Table 3.5: Mechanical properties of REC RUBBER

Tensile Modulus	Elongation at yield	Hardness
?	?	60 (Shore A)

Although the strategy used to increase the dielectric's flexibility, by choosing materials more flexible than the ones previously tested, was a good strategy, it was not possible to print the filament. One reasonable justification is the material being too flexible for the 3D printer. The printer used in this experiment was a boudin cable printer, and it is difficult to print flexible materials with this type of 3D printers.

Since it is not possible to print with materials that have a hardness below 85 (shore A), and all the materials with a hardness equal or superior to 85 (shore A) were tested as dielectrics and were not suitable, the only solution is to change the printing settings of the materials, in order to make the dielectric as flexible as possible.

### ***NinjaFlex 85A (different infill percentage)***

The idea in this new section was to use the most flexible material, between the materials that were possible to print in the previous experiments and change the printing settings to achieve a more flexible dielectric. As a result, the chosen material was the NinjaFlex 85A.

In the previous sections, the dielectric was only printed with layers configured as "bottom layers". The "bottom layers" are thicker, less flexible, layers, when compared to regular layers, since they are configured to assure that there is a correct barrier between the two materials that are being printed. Also, as the setting default, the Ultimaker Cura 4.1.0 program sets the walls to be formed by four lines, these lines are also thicker than the standard lines, to keep the structure in the desired shape.

Since the intension with this project is to deform the shape of the sensor's dielectric, the number of lines defining the wall can be reduced from four to one (it is not possible to print without any "line wall", because of the infill attachment).

Regarding the "bottom layers", it is required to have at least two of them. One of the layers attached to the conductive electrode on the bottom and the other to the conductive electrode on the top. This requirement is essential for both layers to be isolated from each other, so the capacitance behaviour is guaranteed. However, this constitutes the 0.2 mm height of the dielectric that was used in the previous experiments. Therefore, the solution is to increase the dielectric's height from 0.2 to 1 mm and change the inside infill to make it more flexible.

Regarding the infill, several configurations were accessed to understand which one was the most convenient for this project. All the changes in the printing settings are presented in Table 3.6. All the printed sensors used in this section are presented in Figure 3.7. There was also a sensor printed with 100% infill to serve as a reference.

Table 3.6: Comparison between the old printing settings, used to print the previous sensors, with the new printing settings, also the printing settings used to print the two conductive electrodes.

	Previous sensors	New sensors (NinjaFlex 85A)	PI-ETPU 95-250 Carbon Black
Layer height	0.2 mm	0.2 mm	0.2 mm
Wall line count	4	1	3
Top layer	2	1	0
Bottom layer	2	1	“9999999”*
Infill density	100%	50% ; 30%	100%
Infill Pattern	-	Concentric Cross 3D Gyroid	-
*It means that every printed layer is assumed to be a bottom layer.			

After testing all the sensors, it was possible to conclude that all the sensors, in exception to the sensor with the 100% infill dielectric registered a variation in capacitance in response to a pressure variation. This behaviour validates the hypothesis of the influence of the printing settings in the dielectric’s flexibility.

Comparing the three sensors with 50% infill, the sensor that showed higher variations to the different applied forces, was the sensor with the concentric infill, and, for that reason, the most suitable

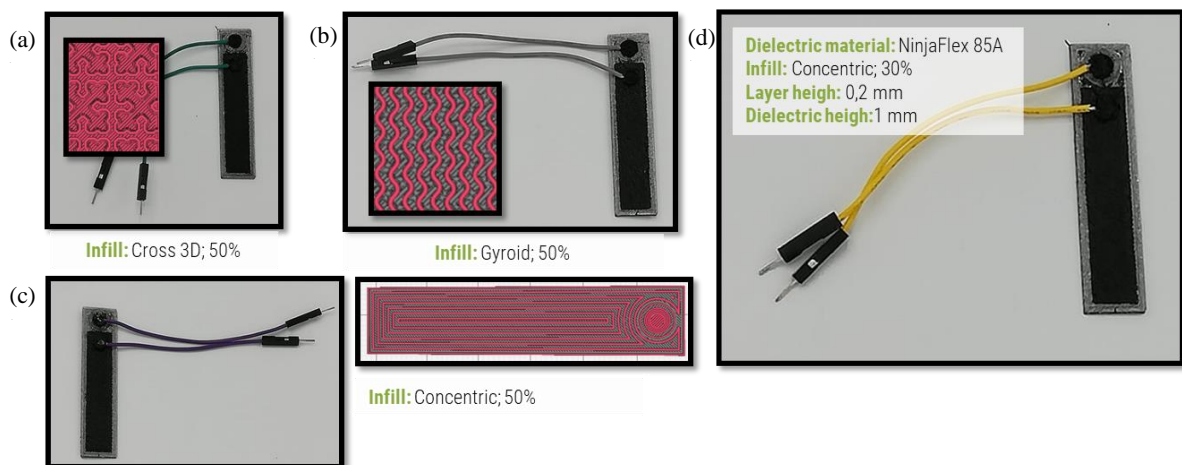


Figure 3.7: Capacitance-based sensor with NinjaFlex 85A as dielectric. (a) Capacitive sensor with 50% cross 3D dielectric’s infill. (b) Capacitive sensor with 50% gyroid dielectric’s infill. (c) Capacitive sensor with 50% concentric dielectric’s infill. (d) Capacitive sensor with 30% concentric dielectric’s infill.

for this project. However, it is important to mention that although it showed the higher variations, it also showed the highest hysteresis when compared to the other two sensors.

When the infill percentage was reduced from 50% to 30%, the sensor did not improve its response. This leads to the conclusion that the best option to 3D print a capacitance-based sensor is with NinjaFlex 85A as dielectric with a 50% concentric infill.

### ***3.2.2 Conclusion***

From the several experiments that were performed and described previously, it is possible to conclude that the best materials to 3D print a capacitance-based force sensor is the PI-ETPU 95-250 Carbon Black for the electrodes and the NinjaFlex 85A for the dielectric, with the following dimensions: the bottom electrode with 50x50x36 mm, the dielectric with 50x13x1 mm and the top electrode with 36x9.4x0.5 mm.

Regarding the printing settings, the electrodes should be printed as “Bottom layers” and the dielectric should be printed with a 50% concentric infill, in exception to the top and bottom layers that should be defined as “Bottom layers”. Also, the walls of the dielectric should be formed by only one line.

## **3.3 Test the 3D printed sensor with the developed reading system**

After developing a reading system able to register, in real time, the capacitance of a parallel plate capacitor, and achieving the configurations of a working 3D printed capacitance-based force sensor, it is now essential to test them together, and understand if they are indeed a reliable measurement system to measure, in real time, the force variations applied by an exoskeleton’s cuff to the user.

### ***3.3.1 Experimental Protocol***

#### ***Materials***

To design and produce the sensor, it was necessary:

- Semi-conductive filament: PI-ETPU 95-250 Carbon Black (Palmiga Innovation, Sweden)
- Non-conductive filament: NinjaFlex 85A (Fenner Inc., USA)
- 3D printer: Ultimaker 3 (Ultimaker B.V., The Netherlands)
- Fusion 360 (Autodesk Ink., United States of America)
- Ultimaker Cura 4.1.0 (Ultimaker B.V., The Netherlands)

To allow the connection between the sensors a breadboard, it is also necessary:

- Jumperwires (sold to the prominences of the sensor)
- The final sensor is showed in Figure 3.7 example c, the printing settings required to print the sensor are presented in Table 3.7

Extra material:

- Multimeter AN8009
- Two 0.5 kg weight

Table 3.7: Printing settings to 3D print the capacitance-based force sensor

	Ninja Flex 85A	PI-ETPU 95-250 Carbon Black
Layer height	0.2 mm	0.2 mm
Wall line count	1	3
Top layer	1	0
Bottom layer	1	“9999999”*
Infill density	50% ; 30%	100%
Infill Pattern	Concentric	-
Printing temperature	230 °C	230 °C
Build plate temperature	45 °C	45 °C
Print speed	15 mm/s	15 mm/s
Fan speed	100%	100%
Prime Blob	Enabled	Enabled
Build plate adhesion type	Skirt	Skirt
Prime tower	Enabled	Enabled
Nozzle type	AA 0,4	BB 0,4
*It means that every printed layer is assumed to be a bottom layer.		

To capture the sensor’s output the reading system developed in the “Development of the sensor’s reading system” subchapter was used. The program used to register the Arduino’s output was the CoolTerm program [73] and the program used to filter and analyse the captured signals was the Matlab R2018b (The MathWorks, Inc., United States of America) program.

### **Data Collection**

To test the 3D printed sensor, as it was executed in the previous experiments, different weights were placed over the sensor to register the capacitance variation due to the variation of the applied forces. The choice of the weights was based on the PDT ( $16.3 \pm 11.2$  to  $34.1 \pm 21.0$  kPa), in conjugation with the ones available in the laboratory, that had approximately the same surface area as the sensors.

Knowing the pressure,  $P$ , is directly proportional to the applied force,  $F$ , and inversely proportional to the area,  $A$ , that same force is being applied, Equation 4.8, and the surface area of the sensor where the weights can be placed is  $\approx 376 \text{ mm}^2$ , the chosen weights were 0.5 kg and 1kg.

$$P = \frac{F}{A} \quad [4.8]$$

The following steps will describe the experimental protocol to collect the required data:

1. Connect the sensor to the electronic set up. Record the time it takes to perform all the steps between step 2 and 12.
2. Turn on the electronic reading system and start recording the Arduino's output.
3. Wait 30 seconds without any weight applied to the sensor (1<sup>st</sup> stage).
4. Without disconnecting the sensor from the electronic reading system, put one of the 0.5 kg weight over the sensor (the sensor must be isolated if the weight is made from a conductive material).
5. Wait 30 seconds (2<sup>nd</sup> stage).
6. Without disconnecting the sensor from the electronic reading system, put the other 0.5 kg weight over the already placed 0.5 kg weight over the sensor.
7. Wait 30 seconds (3<sup>rd</sup> stage).
8. Without disconnecting the sensor from the electronic reading system, take the first 0.5 kg weight over the already placed 0.5 kg weight over the sensor.
9. Wait 30 seconds (4<sup>th</sup> stage).
10. Finally, without disconnecting the sensor from the electronic reading system, take the last 0.5 kg weight over the sensor.
11. Wait 30 seconds (5<sup>th</sup> stage).
12. Stop the recordings and disconnect the sensor from the electronic reading system.
13. Repeat all the steps another two times.

### 3.3.2 Results

Before testing the sensor, it is essential to measure all the important components required to perform this experiment. To achieve the desired weights, 0.5 and 1 kg, several weights were combined. All the important measurements are present in Table 3.1, and Table 3.8.

Table 3.8: Weight's measurement

	1 <sup>st</sup> weight (g)	2 <sup>nd</sup> weight (g)	3 <sup>rd</sup> weight (g)	4 <sup>th</sup> weight (g)	5 <sup>th</sup> weight (g)	6 <sup>th</sup> weight (g)
1 <sup>st</sup> trial	115.2 ± 0.1	141.8 ± 0.1	143.2 ± 0.1	144.3 ± 0.1	384.2 ± 0.1	121.2 ± 0.1
2 <sup>nd</sup> trial	115.2 ± 0.1	141.8 ± 0.1	143.2 ± 0.1	144.3 ± 0.1	384.1 ± 0.1	121.3 ± 0.1
3 <sup>rd</sup> trial	115.2 ± 0.1	141.8 ± 0.1	143.2 ± 0.1	144.3 ± 0.1	384.1 ± 0.1	121.2 ± 0.1
mean	115.2 ± 0.1	141.8 ± 0.1	143.2 ± 0.1	144.3 ± 0.1	384.1 ± 0.1	121.2 ± 0.1
Final weight	1 <sup>st</sup> "weight" (g)				2 <sup>nd</sup> "weight" (g)	
	544.5 ± 0.4				505.3 ± 0.2	
	1049.8 ± 0.6					

After performing all the experiments, the recorded signals must be filtered before being analysed. To filter the signal, a lowpass, 2<sup>nd</sup> order Butterworth filter was applied.

To decide which normalised cut off frequency,  $w_n$ , to use it is first necessary to calculate the sampling rate of the signal,  $f_s$ , which corresponds to the division of the number of samples, taken in the

experiment, by the time of the entire trial. To obtain the normalized cut off frequency, the cut off frequency,  $f_c$ , in hertz, is divided by half of the sampling rate, Equation 3.9.

$$w_n = \frac{f_c}{f_s/2} \quad [3.9]$$

The cut off frequency chosen for this experiment was 0.06 Hz. The charging time of the capacitor, already filtered, from the three experiments is represented in Figure 3.8.

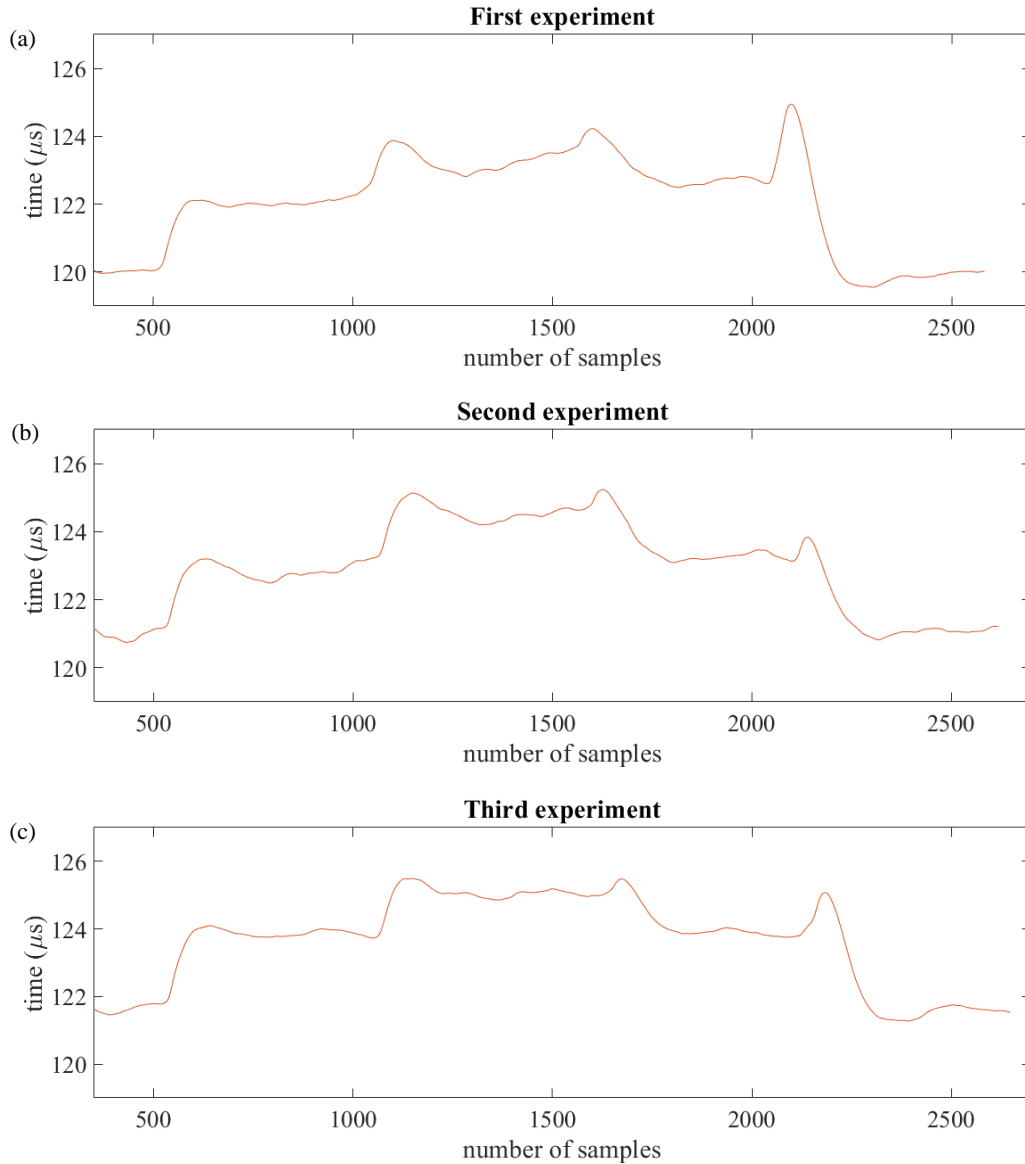


Figure 3.8: Filtered signal with a lowpass, 2nd order butterworth filter with a cut off frequency of 0.06Hz. (a) Signal from the first experiment. (b) Signal from the second experiment. (c) Signal from the third experiment.

To calculate the capacitance variation due to the change of the weights applied to the sensor, Equation 3.2 was used, and the mean capacitance of each stage calculated (without taking into consideration the peaks). The associated errors were calculated using the Equations 3.3-3.7, described in “3.1.2 Results” section. The results are presented in the next table,

Table 3.9:

Table 3.9: Mean capacitance in each stage of the experiment

Trial	1 <sup>st</sup> stage (pF)	2 <sup>nd</sup> stage (pF)	3 <sup>rd</sup> stage (pF)	4 <sup>th</sup> stage (pF)	5 <sup>th</sup> stage (pF)
1 <sup>st</sup>	106.650 ± 0.630	108.010 ± 0.002	108.960 ± 0.110	108.590 ± 0.050	106.040 ± 0.120
2 <sup>nd</sup>	107.400 ± 0.500	108.660 ± 0.010	110.120 ± 0.060	109.100 ± 0.030	107.150 ± 0.060
3 <sup>rd</sup>	107.940 ± 0.420	109.610 ± 0.004	110.650 ± 0.010	109.660 ± 0.0030	107.580 ± 0.130

To better understand the changes in capacitance, the relative difference between the 1<sup>st</sup> stage and all the other stages was calculated and presented in Table 3.10.

Table 3.10 - Relative difference, in percentage, between the 1<sup>st</sup> stage and the other stages. The results in this table are colorized according to their value in comparison to all the other values in the table. The colour blue corresponds to the lowest values and the colour red to the highest values.

Trial	$\Delta$ (1-2) (%)	$\Delta$ (2-3) (%)	$\Delta$ (3-4) (%)	$\Delta$ (4-5) (%)
1 <sup>st</sup>	1.27	2.16	1.82	-0.57
2 <sup>nd</sup>	1.16	2.53	1.58	-0.24
3 <sup>rd</sup>	1.55	2.51	1.6	-0.34

After calculating the capacitance by the application of the theoretical equations, the mean capacitance was calculated by the application of the equation obtained in the “3.1.3 Results” subsection, that establishes a linear relation between the capacitance and the capacitor’s charging time, expressed in Figure 3.3. The results are presented in the following table, Table 3.11.

Table 3.11 - Mean capacitance in each stage of the experiment, calculated by the equation presented in figure 4 obtained in the calculus section of the set up development experiment.

Trial	1 <sup>st</sup> stage (pF)	2 <sup>nd</sup> stage (pF)	3 <sup>rd</sup> stage (pF)	4 <sup>th</sup> stage (pF)	5 <sup>th</sup> stage (pF)
1 <sup>st</sup>	40.91	42.37	43.39	42.99	40.25
2 <sup>nd</sup>	41.71	43.07	44.64	43.53	41.44
3 <sup>rd</sup>	42.29	44.09	45.21	44.14	41.90

### 3.3.3 Conclusion

From the three graphics, Figure 3.8, it is possible to observe that the first stage has a smaller time duration than the other stages. This happens because the filters’ output depends on its input, as well as, its past input(s) and past output(s) [74]. For this reason, the first part of the signal was cut off since it does not represent the reality.

The four peaks, present in the three graphics, correspond to artefact noises due to the exact moment when the weights were put on or taken off the sensor. These peaks could be removed by decreasing the cut off frequency, however, the time between the start of the experiment and the time where the signal corresponds to the real values would increase, making it impossible to calculate the capacitance in the first stage. Without the mean capacitance from the first stage, the reference capacitance would be lost, leading to a loss of information, so, for the next experiments, it is important to consider this factor.

From the graphics presented in Figure 3.8, and the mean capacitance values given in the Table 3.10 and Table 3.11, it is possible to recognize the different stages, and verify that the capacitance indeed increases with the increase of pressure and decreases with the decrease in pressure. However, it is important to mention that the variation in capacitance, when the weights are added, is not equal to the variation when the weights are taken off. This phenomenon may be associated to the properties of the sensor's material, since it is made from TPU, and the thermoplastic polyurethanes exhibit strong hysteresis, rate dependence and cyclic softening [69].

Although the deformation of the sensor is not instantaneous, nor constant, from the results, it is possible to determine the weights' value that were placed over the sensor, which leads to the conclusion that this reading method can be used to register a force applied to a 3D-printed sensor in real-time, with a certain associated error.

### **3.4 Additional tests**

After testing the sensor with the specified configurations, some other tests were performed in an attempt to optimize the effectiveness of the sensor's readings.

The first idea was to increase the number of samples for the same period of time, which in theory would lead to a more accurate signal.

To make sure the capacitor discharges completely, the Arduino code, was written to wait 30ms between each measuring cycles, however the actual discharging time is smaller, so one way to increase the number of samples, while keeping the same period of time, is to reduce the waiting time. In this case the time was reduced from 30ms to 20ms and 10ms.

In opposition to the authors thoughts, reducing the waiting time, increasing the number of samples, did not increase the accuracy of the signal, and for this reason the waiting time was kept the same.

Another important tested aspect was the dependence of the Arduino's output with the time the sensor is connected to the electronic set up. To test it, the Arduino was connected to the sensor 30 s, 1 min., 2 min., 4 min. and 8 min. without any weight applied. The results from this experiment did not vary significantly so the drift was not considered in the final capacitance calculations.

### **3.5 Final conclusions and Future work**

From the three performed experiments, it was possible to fabricate and test the setup system, constituted by a 3D printed capacitance-based sensor, associated with an electronic measurement system, able to register force variations applied to the sensor. Therefore, the second question presented in the "Aim" subchapter: "Is it possible to produce working 3D printed force sensors?" can be answered affirmatively.

Although it was possible to measure force variations, the measurements had a significant error associated. In following experiments, this error could be reduced by choosing a better and most-suited

Op-Amp with a lower input offset voltage associated. Also, by increasing the resistance associated to pin 9's input, the results would be closer to the real values.

Regarding the sensor's fabrication process, some changes could be done to optimise its performance. One option to reduce its hysteresis and time-dependence, maybe by changing its materials, choosing other material more suitable. Another option is, instead of changing the material, modulate the sensor's response to the TPU behaviour, changing from a linear equation to an equation more appropriate.

Although this reading method showed great promises, all the filtering was done after the signal was registered, it was not tested in real-time. In future work, it would be interesting to filter the values in real-time and understand if it would still be able to recognise the different forces applied to the sensor.

After testing the sensor in real-time, the sensor should be integrated into an exoskeleton's cuff, and tested. From the recordings an assessment should be done to understand if indeed the integration of force sensors into the exoskeletons, more precisely, the application of its readings into the exoskeletons' control, would improve the comfort and safety of the exoskeleton.



# Chapter 4

## STUDY OF THE DEFORMATION OF THE LOWER LIMB MUSCLES

In the previous sections, efficient 3D printed EMG and force sensors were developed, leading to the following and last step, before designing the 3D printed exoskeleton's cuff with 3D printed sensors incorporated, the study of the lower limb muscles, more precisely, the understanding of the optimal locations to place the sensors and how these optimal locations deform through the gait cycle.

To study the lower limb muscles' deformation, three scans will be performed during three distinct positions of the gait cycle: the mid stance, heel strike and heel off positions. These scans will be transversely segmented, in the most preeminent part of each muscle, chosen in the "1.6.2 Integration of the 3D printed sensors into the exoskeleton's cuff" subchapter, which will correspond to the locations where the EMG sensors will be placed.

The muscles that are going to be accessed in this project are: the Tibialis anterior, and the Lateral and Medial Gastrocnemius, of the left leg (the 3D printed interface, developed by K. Langlois *et al.* for the exoskeleton, developed in the BioMot project [14], [64], was developed for the left leg). The algorithm used to correctly segment the scans along with the respective results and conclusions from the segments will be presented in this chapter.

### 4.1 Experimental Protocol

In the following subchapter the experimental protocol, describing how to correctly scan the subjects' leg, as well as the algorithm to analyse these same scans, along with the materials required to perform this experiment, will be described.

#### 4.1.1 Materials

To mark the important locations of the leg and scan them, it is necessary:

- 9 spheres
- Double side tape
- Structure sensor mark II (Occipital, Inc., United States of America)

To analyse the scans, the following programs will be required:

- Autodesk Meshmixer (Autodesk, Inc., United States of America)
- ZBrush 2019 (Pixologic, Inc., United States of America)
- Matlab R2018b (The MathWorks, Inc., United States of America)

### 4.1.2 Data Collection

To facilitate the scan's analyses, the most preeminent parts of each muscle will be marked with the spheres to simplify its identification. These spheres will be labelled as markers.

The following procedure will describe the method to properly scan the leg:

1. With the double side tape, glue, to the subjects' skin, 3 markers, in random locations of the tibia. These markers will be labelled as:
  - a. Tibia Down, TD, marker, which will correspond to the marker closest to the ground (Figure 4.1 example a).
  - b. Tibia Middle, TM, marker, which will correspond to the second closest marker of the tibia to the ground (Figure 4.1 example a).
  - c. Tibia Up, TU, marker, which will correspond to the highest marker from the tibia's markers set (Figure 4.1 example a).
2. With the double side tape, fixe to the subjects' skin, 2 spheres for each muscle, as they were each an EMG transducer (3 cm spaced). The locations, were the markers should be placed, are based on the SENIAM project's recommendations, however it is important to refer that it is only a guideline, the ideal location varies from subject to subject:
  - a. Tibialis anterior: 1/3 on the line between the tip of the fibula and the tip of the medial malleolus, the two electrodes should be placed over this line [65]. These two markers will be labelled as:
    - i. Tibialis Anterior Down, TiD, marker, which will correspond to the marker, between the two, that is closest to the ground (Figure 4.1 example a).
    - ii. Tibialis Anterior Up, TiU, marker, which will correspond to the marker, between the two, that is further away from the ground (Figure 4.1 example a).
  - b. Lateral Gastrocnemius: 1/3 of the line between the head of the fibula and the heel, the two electrodes should be placed over this line [65]. These two markers will be labelled as:
    - i. Lateral Gastrocnemius Down, LGD, marker, which will correspond to the marker, between the two, that is closest to the ground (Figure 4.1 example b).
    - ii. Lateral Gastrocnemius Up, LGU, marker, which will correspond to the marker, between the two, that is further away from the ground (Figure 4.1 example b).
  - c. Medial Gastrocnemius: Most prominent bulge of the muscle, both in the direction of the leg [65]. These two markers will be labelled as:
    - i. Medial Gastrocnemius Down, MGD, marker, which will correspond to the marker, between the two, that is closest to the ground (Figure 4.1 example b).
    - ii. Medial Gastrocnemius Up, MGU, marker, which will correspond to the marker, between the two, that is further away from the ground.
  - d. The conjugation of the six markers will be named as EMG markers.
3. Scan the leg in three distinct positions: mid stance, heel off and heel strike (Figure 4.1 example b).

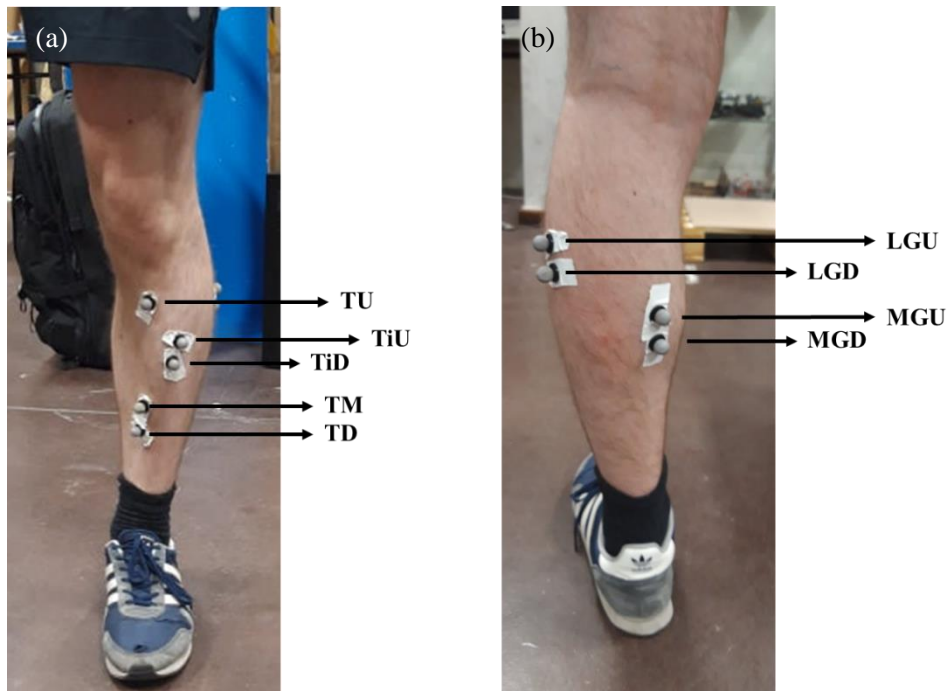


Figure 4.1 Markers' ideal locations, for subject number 4, each marker has its respective label. (a) Anterior view (b) Posterior view.

In this experiment, the left leg of five healthy subjects, one female and four males, was scanned as previously described, after giving their informed consent. The subjects will be address by numbers, from one to five, randomly assigned.

### 4.1.3 Scan's treatment

After scanning the leg, the scans have to be treated, more specifically, the important parts that are going to be analysed have to be isolated from the rest of the scans, and the mesh (which the scan is made of) must be resized in order to uniform all scans.

The following procedure will describe how the scans should be treated:

1. Import the scans to the Autodesk Meshmixer program. (Figure 4.2, example a)
2. Cut of all the unnecessary parts, leaving just the part of the leg with the markers.
3. Aligned the scan with the Z-axis.
4. Filled the holes that may exist and save the scan as an STL file. The result is shown in Figure 4.2, example b.
5. Import the previous STL file to the ZBrush 2019.
6. Resize the scan's mesh by changing the following properties:
  - a. Target Polygon Count: 30.50951
  - b. Adaptative Size: 0
7. Save the scan as an STL file.

The final result is represented in Figure 4.2, example c.

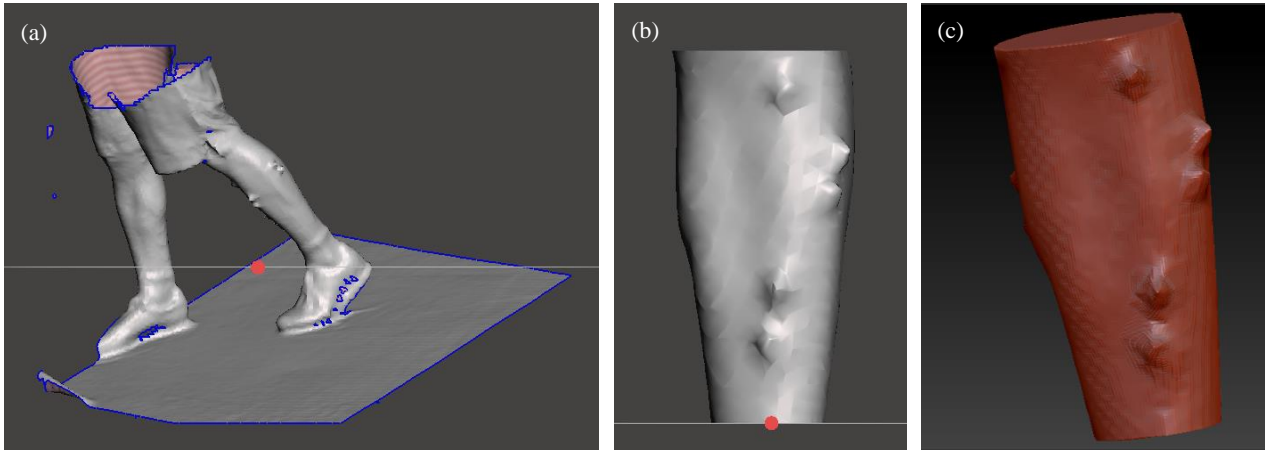


Figure 4.2: (a) Scan, from subject number one, imported to Autodesk Meshmixer program. (b) Scan, from subject number one, after the “cleaning”, in the Autodesk Meshmixer program. (c) Scan results, from subject number one, after resizing the scan’s mesh in the ZBrush 2019 program.

#### 4.1.4 Markers’ Identification algorithm

After taking the leg’s scans, with the markers placed in the ideal spots, and treat them only to have the valuable information, the scans are ready to be analysed.

As it was described previously, the project’s goal is to access the variation, in geometry, of the chosen lower limb muscles, in three distinct positions of the gait cycle, by transversely segment the leg in specific places. As it was explained in the Data Collection sub-chapter, the preeminent part of each muscle is marked with a pair of EMG markers, so the transverse planes will correspond to the plane in between the two markers of each muscle.

The first step to achieve the final goal is to write an algorithm, able to identify the markers in the scans. This algorithm is going to be described in this section.

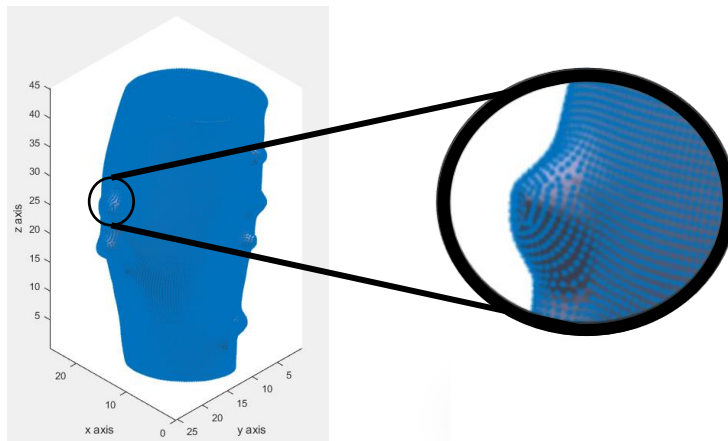


Figure 4.3: Vertices’ representation of the STL file, from subject number one.

As it was explained previously, the scans are saved as STL files, so, to open them, it is necessary a special function, in this case, the `stlread` function, which has to be downloaded and imported to MATLAB [75]. One of the outputs of this function is a matrix with the coordinates of every vertex of the mesh, which the scan is formed, see Figure 4.4. However, the vertices are arbitrarily ordered, so, the first course of action is to re-order the vertices in the XYZ plane.

## Organisation of the Vertices

The vertices' organisation starts by initially organising the vertices in the z-axis direction, from the vertex with the lowest z-coordinate to the vertex with the highest z-coordinate. Also, the vertices will be separated into consecutive groups. The first group will include all the vertices that have their z-coordinate in between the lowest z-coordinate and the lowest z-coordinate + 0.5 units of measure, u.m; the next group will start with the lowest z-coordinate + 0.5 u.m and end with the z-coordinate + 1 u.m and so on until the vertex with highest z-coordinate is reached.

The groups that were formed will be referred as segments, and, for the next stages, only the segments formed by 200 vertices or more will be considered. The threshold's choice was based on que segments' quality, which to the authors opinion, below this threshold, is not enough to take proper conclusions. The vertices of each segment will be organised in a counter clockwise direction, Figure 4.4.

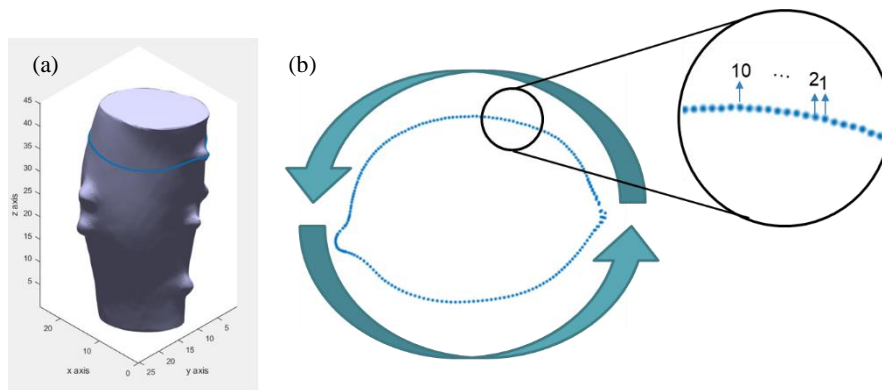


Figure 4.4: (a) One of the defined segments of the scan from subject number one, (b) Schematic of the organization of the vertices, in one segment, in a counter clockwise direction.

The first step, required to organise the vertices in a counter-clockwise direction, is to arrange them in the x-axis direction, therefore, for each segment, the vertices will be organized from the vertex with the lowest x-coordinate to the vertex with the highest x-coordinate. After the first arrangement, the vertices must be organised according to their y-coordinate, while maintaining the x-coordinates organization. To do that, the y-coordinate of the first element of each segment is registered and will function as a threshold. This threshold will be used to separate the segment into two groups: a group formed by the vertices that have their y-coordinate above the threshold and the other with the y-coordinate below the threshold.

The group with the y-coordinate below the threshold is registered first, from the value with the lowest x-coordinate to the value with the highest x-coordinate. After recording the first group, the second group is registered, but in the reverse order, from the vertex with the highest x-coordinate to the vertex with the lowest x-coordinate value.

From the application of these three methods, a matrix with all the vertices separated into different segments, where each segment has its vertices organized in a counter clockwise direction, was achieved. This matrix will be called *organized vertices' matrix*.

With the vertices organised into a matrix, the markers identification process is set to begin. In the following stages, several identification methods are going to be applied and combined to achieve this first goal of the algorithm.

### ***First Identification Method***

The principle behind the first identification method was: the identification of each segment's centroid, and, from there, the calculation of the distance between the centroid and each vertex of the corresponding segment.

A centroid can be defined as the arithmetic mean position of all the points, in this case vertices, of a geometrical figure, in this case the segments.

Usually, when the mean of a considerable number of samples is calculated, the outliers of the group will almost not influence the final calculation. Since the centroids are the average of the xy-coordinates of all points, and the number of vertices defining the markers is much smaller than the number of vertices representing the leg, the centroid's value will be almost the same with or without the marker. So, in theory, when the distance between each vertex of the segment and the centroid is calculated, the distance will be greater between the markers and the centroid than between the vertices of the leg and the centroid, enabling the identification of the markers.

There are several ways to calculate the centroid of a geometrical figure. In this case, the segments were considered as non-self-intersecting polygons, constituted by  $n$  vertices  $(x_0, y_0), (x_1, y_1), \dots, (x_{n-1}, y_{n-1})$ , (it was assumed that every vertex in each segments had the same z-coordinate), and for this reason, the centroids' coordinates,  $(C_x, C_y)$ , can be calculated by application of the following equations:

$$C_x = \frac{1}{6A} \sum_{i=0}^{n-1} (x_i + x_{i+1})(x_i y_{i+1} - x_{i+1} y_i) \quad [4.1]$$

$$C_y = \frac{1}{6A} \sum_{i=0}^{n-1} (y_i + y_{i+1})(x_i y_{i+1} - x_{i+1} y_i) \quad [4.2]$$

$$A = \frac{1}{2} \sum_{i=0}^{n-1} (x_i y_{i+1} - x_{i+1} y_i) \quad [4.3]$$

Where  $A$  is the area of the segment.

After obtaining the centroids' coordinates of every segment, the distance between the centroid and the vertices was calculated and registered in a matrix, the *centroid-vertex distance's matrix*.

To help the identification of the markers in the following stages, a smooth filter, more specifically a moving average filter, was applied to the data in the *centroid-vertex distance's matrix*.

To identify a potential marker, a comparison is made between every vertex' distance to the centroid to the following distance of the following vertex to the centroid. The variations that are positive, meaning the distance of the following vertex is higher than the distance of the previous one, are added up and the number of vertices counted, until the variation becomes negative. When the variation becomes negative, if the next variation is positive the sum of the distances, and the count of the number of vertices continues, if not, the sum of the distances, as well as the vertices counting function are set to 0 and the process will only restart when a positive variation appears again.

After the sum of the distances is made, if the result is higher than 0.75 u.m, and the number of vertices counted, higher than 20, a marker is assumed to be found, and the coordinates of the last vertex, to be counted, are registered in a new matrix, along with the coordinates of previous and following vertices, this matrix will be called *potential marker's matrix*.

The results of this identification system are presented in the next figure, Figure 4.5.

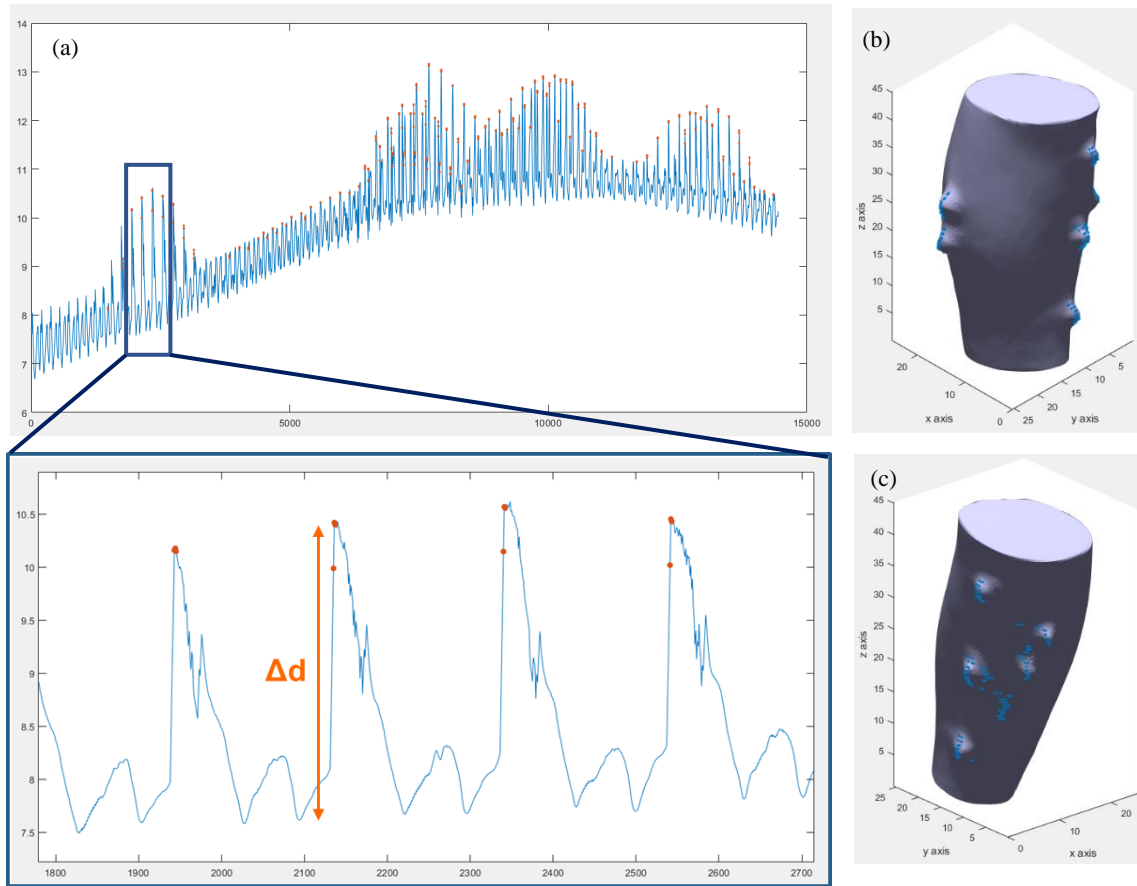


Figure 4.5: (a) Distance of every vertex to the centroid of the segment they belong to, after filtering, from a scan, the orange spots correspond to possible markers that were identified by the first identification method. (b) and (c) Identified markers of a part of the scan, from subject number one.

### ***Second Identification Method***

In this new identification method, the results obtained in the previous method were used and adapted to achieve a better classification system.

As it was explained previously, to every potential marker, its vertex' coordinates and distance to the centroid, as well as the distance and coordinates of the previous and following vertices, were registered in the *potential marker's matrix*. With this information, two different angles were calculated.

To measure the first angle, the distance to the centroid and the index to which each vertex corresponds in the *organised vertices' matrix*, are considered to be coordinates. The three vertices that define a possible marker form two vectors, both with their tails being the vertex that theoretically corresponds to the marker and the heads one being the previous vertex and the other one being the following vertex. The first angle will correspond to the angle formed by these two vectors.

Regarding the second angle, the coordinates used to form the two vectors were actually the xy-coordinates each vertex, but instead of using the previous and following vertices as the heads of the vectors, it was used the vertex before the previous vertex and the vertex after the following vertex. The second angle corresponds to the angle formed by these new vectors, Figure 4.6 example a.

From the information given by the two angles, a vertex was defined to be a marker, if its first angle was lower than  $165^\circ$ , and its second angle lower than  $170^\circ$  and higher than  $15^\circ$ . The results are shown in Figure 4.6, example b, where the blue dots correspond to the markers identified using the first identification method, and the orange dots, the markers determined by the second identification method. The coordinates of the identified markers are saved in the *angle-markers' matrix*.

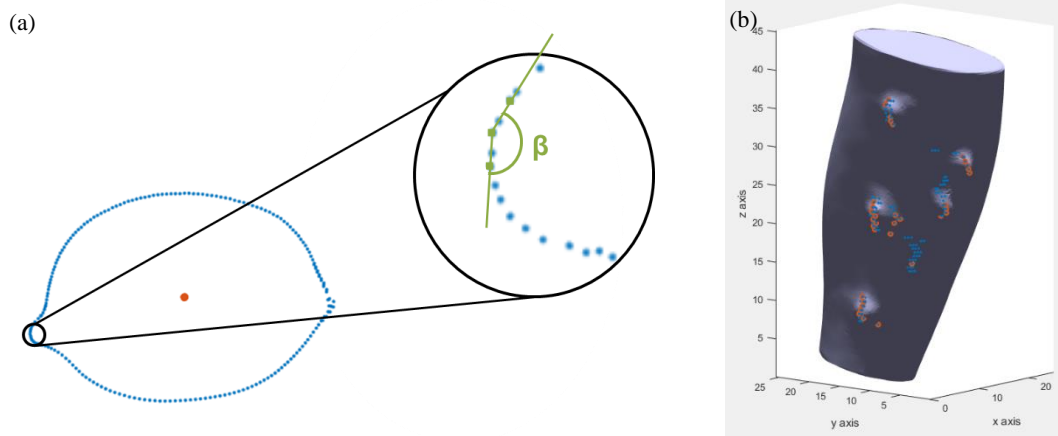


Figure 4.6: (a) Schematics of the second angle. (b) Identified markers of a part of the scan, from subject number one. The blue dots correspond to the markers identified by the first identification method and the orange dots the markers identified by the second identification method.

It is clear, from Figure 4.6, example b, that there is an increase in the accuracy of the marker's detection, from the first identification method to the second. However, there is still a considerable number of markers incorrectly identified.

### ***Third Identification Method***

In the third identification method, instead of using the segment's centroid as reference, the approximated ellipse of each segment was calculated and used as starting point to identify the coordinates of possible markers.

The idea behind this third identification method is to approximate each segment to an ellipse. Since the markers are irregular shapes of the segments, that have much fewer vertices defining them than the actual leg, they will stand out, having a greater distance between its vertices and the ellipse, than the leg's vertices.

An ellipse can be defined by the following equation:

$$ax^2 + bxy + cy^2 + dx + ey + f = 0 \quad [4.4]$$

Where  $x$  and  $y$  are variables and  $a$ ,  $b$ ,  $c$ ,  $d$ ,  $e$  and  $f$  are the ellipse's parameters. To calculate the parameters of the ellipses, a function was written based on the script created by Nikolai Chernov [76].

After calculating the fitting ellipse for each segment, the distance between the ellipse and every vertex of each segment was calculated. To compute this distance, it is first necessary to deduce the linear function that connects the centroid of the segment, to each constituting vertex. After the previous step, the intersection between the linear functions and the ellipse must be found, to allow the distance between the ellipse and each vertex of the segment to be calculated, Figure 4.7 example a.

From the calculated distances, a potential marker is identified if it fulfils two specifications. The first specification is to the vertex of the segment to be further away from the centroid than the interception of the linear equation with the ellipse. The second specification is to be separated from the ellipse at least 0.75 u.m. The results are saved in the *ellipse-markers' matrix*.

As it is possible to observe from Figure 4.7, example b and c, this third identification method shows great promises but still has some associated identification errors.

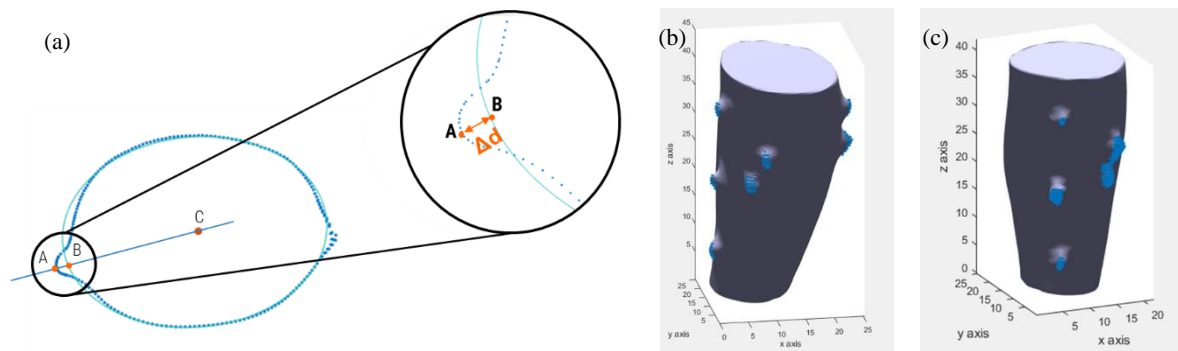


Figure 4.7: (a) Schematics of the fundamentals the third identification method is based on. (b) and (c) Results of the application of the third identification method, being the blue spots, the vertices identified as possible markers (scan from subject number one).

### Fourth Identification Method

In the previous sections, three identification methods, to identify the markers in a scan, were presented, all correctly identifying the markers but, with a significant associated error. For this reason, the fourth identification method will be the conjugation of the last two identification methods (second and third identification method).

In this method, the vertices identified as possible markers by the second method are considered to be the reference points. If the vertices determined as potential markers by the third method are closer than 1.5  $\mu\text{m}$  to one of the reference points, than they are considered to be markers and saved in a new matrix, Figure 4.8, example a.

From this new matrix, the identified markers are associated in groups if the distance between each other is smaller than 5  $\mu\text{m}$ . For each group, the mean of the vertices' xyz-coordinates is calculated. Since the mean does not correspond to a vertex of the scan, the coordinates of the final markers will be the coordinates of the vertex that is closer to the mean coordinates, Figure 4.8, example b and c. The identified markers are saved in the *final markers' matrix*.

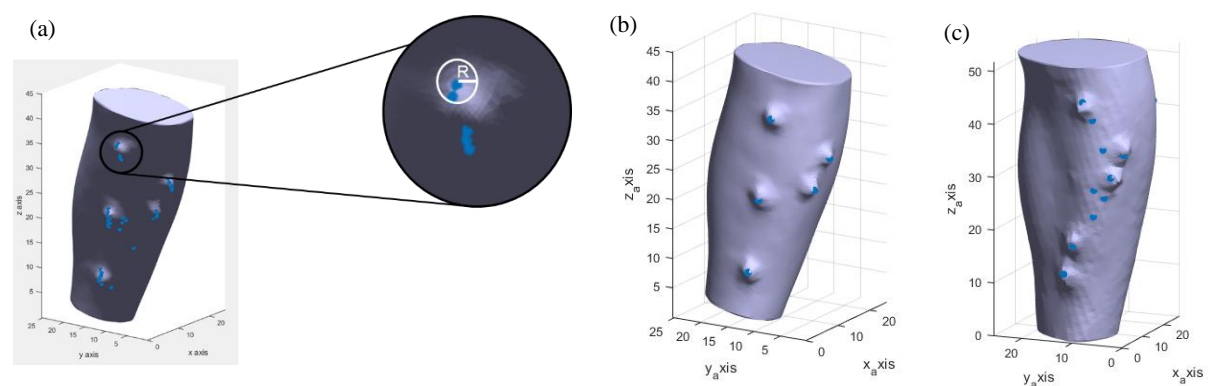


Figure 4.8: (a) Schematics of the fundamentals the fourth identification method is based on. (b) and (c) Results of the application of the fourth identification method, being the blue spots, the vertices identified as possible markers (scans from subject number one).

With this identification code, almost all the markers are identified. However, there is still some identified markers that are not in fact markers, also there are other markers that are being identified by

several points, instead of only one. In the next step, the objective will be to eliminate the falsely marked markers and to assign one point, which means only one set of coordinates, per marker.

### ***False markers elimination method***

To eliminate the markers from the *final markers' matrix*, that do not correspond to the real markers, two vectors will be created, for each identified marker. The tails of the vectors will correspond to the coordinates of the markers. The heads will correspond to the coordinates of the vertices that have the closest XY-coordinates of the marker but are located two segments above, for one of the vectors, and two segments below for the other. If the angle formed by the two vectors is greater than  $170^\circ$ , it is not a marker, and it is deleted from the *final markers' matrix*. The threshold value was achieved by testing which angle showed best results.

Regarding the markers that are being identified for more than one set of coordinates, the first step towards their elimination is to identify them. This identification is made based on the distance between the markers. If the vertices that are being recognized as possible markers are less than 4 u.m apart, it means they are spotting the same marker. From this identification, it is possible to treat the data in two separate ways.

If the vertices are separated by a distance smaller than 1.5 u.m in the XY-plane (not considering the z-coordinate), in theory, it means they are in the sides of the marker, equally distant to the middle of the marker. For this reason, a mean between the two is made, and the vertex, from the *organised vertices' matrix*, that is closest to this mean is identified as marker.

If the distance is greater than 1.5 u.m, in theory, one of the points is closest to the centre of the marker than the other, which means further away from the centroid, so the vertex that is going to be considered as marker, will be the one, between the two, the one that is further away from the respective centroid.

To make sure all the markers are correctly identified, the script asks the user if all the markers are correctly placed and if there is any marker missing. If the answer is positive, then it gives the liberty for the user to insert what is missing or delete what is poorly marked, in the markers' matrix.

### ***Efficiency analysis***

The marker's identification algorithm was applied to every scan to understand if it was an efficient method to identify the markers correctly. In the case of some subjects, for the same position, their leg was scanned twice, so there were 18 analysed scans instead of 15, leading to a total of 162 markers.

From the 162 markers, 89.51% were identified as a marker. Also, there were vertices identified as markers that were not indeed markers. From the 162 markers plus 13 vertices defined incorrectly as markers, 82.86% were correctly identified, the rest were either not detected either misplaced.

The markers' identification efficiency could be improved with an improvement of the quality of the scans and also with all the scans being in the same position, preferably aligned with the z-axis.

### ***4.1.5 Alignment of the scans***

After identifying all the markers, it is necessary to align the scans. This alignment will be done based on the position of the tibia's markers. For this reason, the first thing to do is to identify which markers correspond to the tibia's markers and calculate the plane formed by the three.

### ***Tibia's markers identification and respective plane calculation***

As it was explained in the previous chapter, more specifically in the “Organisation of the Vertices” sub-chapter, the vertices that form the 3D shape of the leg are organized in segments based on their z-coordinates, being the first segment the segment with the lowest z-coordinate and the last segment the segment with the highest z-coordinate.

Knowing the lowest marker is one of the tibia's markers, then the first marker in the markers' matrix must be a marker of the tibia, the TD marker. Because the tibia is more or less straight, and the tibia is approximately perpendicular to the XY-plane, the other two markers, TM and TU, will be the ones that have the smallest distance to TD in the XY-plane, without taking into consideration the z-coordinate.

After recognising the three tibia markers, the next step is to compute the plane's parameters of the plane formed by the three. A plane can be defined by the following equation:

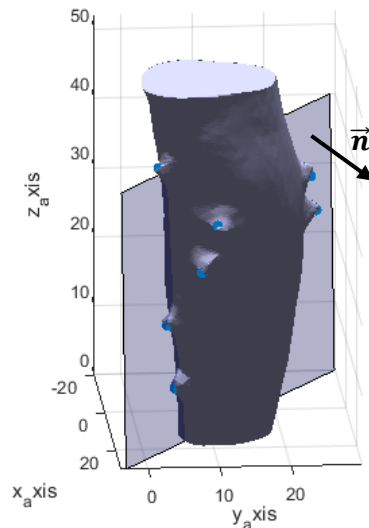


Figure 4.9: Representation of a plane formed by the three tibia markers and respective normal vector (scan from subject number one).

$$ax + by + cz + d = 0 \quad [4.5]$$

Where  $x$ ,  $y$  and  $z$  are variables and  $a$ ,  $b$ ,  $c$  and  $d$  are the plane's parameters,  $a$ ,  $b$  and  $c$  correspond as well to the coordinates of the plane's normal vector,  $\vec{n}$ . A representation of a plane formed by the three markers of the tibia, with the respective normal vector is represented in Figure 4.9.

After defining the *Tibia's plane*, the following step is to overlap the tibia's markers from the three scans.

### ***Alignment of the tibia markers***

Before aligning the markers of the tibia, the distance between TD and TU is measured in the three scans. Based on these distances, the scans from the heel off position and the heel strike position are rescaled in order to assure the markers of the tibia are equally spaced, since, in theory, the tibia's markers maintain their distance regardless of the movement.

After rescaling the scans, the alignment process begins. First, the scans from the heel off and mid stance positions are aligned, and only after, the scan from the heel strike position is aligned with the two previous scans. To align the first two scans, the interception line, between the two respective

tibia planes, must be calculated. The interception line's equation, will be written as the following expression:

$$\frac{x - x_0}{a} = \frac{y - y_0}{b} = \frac{z - z_0}{c} \quad [4.6]$$

Where  $x$ ,  $y$  and  $z$  are variables,  $x_0$ ,  $y_0$  and  $z_0$  are the coordinates of a random point that belongs to the interception line, and last  $a$ ,  $b$  and  $c$  are the coordinates of the line's direction vector,  $\vec{u}$ , that is orthogonal to the two normal vectors that define the two planes that are being intersected. Therefore,  $\vec{u}$ ,  $x_0$ ,  $y_0$  and  $z_0$ , must be calculated to obtain the interception line.

It is important to refer that, since  $\vec{u}$ , is orthogonal to the two normal vectors that define the two intersecting planes,  $\vec{n}_1$  and  $\vec{n}_2$ , then  $\vec{u} = \vec{n}_1 \times \vec{n}_2$ .

With the interception line defined, both scans are shifted according to a translation vector that has its tail designated to be the TU marker and the head a point in the interception line (the head is the same for both translation vectors).

After both shifts are performed, both TU markers from the two different scans have the same coordinates. However, the same does not happen to the other markers of the tibia, so they need to be shifted without shifting the TU markers. This can be achieved by rotating the scans, around the TU coordinates.

To rotate the vertices of the scan it is required first to calculate the rotation matrix,  $R$ , which is given by:

$$R = \begin{bmatrix} \cos \theta + v_x^2(1 - \cos \theta) & v_y v_x(1 - \cos \theta) - v_z \sin \theta & v_z v_x(1 - \cos \theta) + v_y \sin \theta \\ v_y v_x(1 - \cos \theta) + v_z \sin \theta & \cos \theta + v_y^2(1 - \cos \theta) & v_y v_z(1 - \cos \theta) - v_x \sin \theta \\ v_x v_z(1 - \cos \theta) - v_y \sin \theta & v_z v_y(1 - \cos \theta) + v_x \sin \theta & \cos \theta + v_z^2(1 - \cos \theta) \end{bmatrix} \quad [4.7]$$

Where  $\theta$  is the rotation angle and  $\vec{v} = (v_x, v_y, v_z)$ , the rotation axis,  $\vec{v}$  is a unit vector ( $v_x^2 + v_y^2 + v_z^2 = 1$ ).

The goal of this rotation is to bring all the tibia's markers into the intersection line (Figure 4.10), so the first step is to calculate the coordinates of the final point, FP, where the TD will be, after the rotation, which will correspond to the distance,  $L$ , between TU and TD. After calculating the FP, the distance,  $D$ , between FP and TD is computed and the rotation angle is given by:

$$\theta = 2 \sin^{-1} \left( \frac{D}{2L} \right) \quad [4.8]$$

The rotation axis will be the normal vector of each tibia plane, the unit vector can be computed by:

$$\vec{v} = \frac{\vec{v}_{tibia\ plane}}{|\vec{v}_{tibia\ plane}|} \quad [4.9]$$

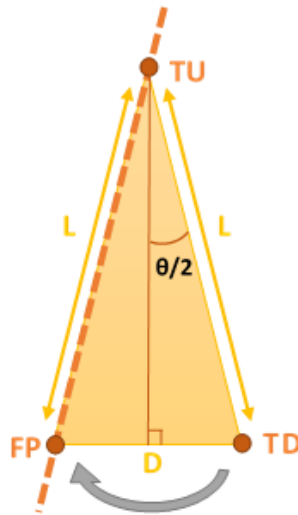


Figure 4.10: Schematic of the rotation angle,  $\theta$ .

With the rotation matrix calculated, the last step is to multiply R by the organised vertices' matrix. To rotate around TU, the z-coordinate of TU must be defined as 0.

The described procedure is performed for all the heel off and mid stance position's vertices. With these two matrixes already rotated, the same process is applied to the heel strike position matrix where the other two matrixes (the heel of and mid stance vertices' matrix) are the same matrix.

With all the tibia markers aligned, the second stage begins. The aim is to correctly align the three scans. The idea is similar to the first rotation but, instead of overlapping the tibia markers, overlapping the centre of the scans.

### ***Alignment of the scans***

Similar to the last sub-section, the scans from the heel off and mid stance positions are firstly aligned, and only after, the scan from the heel strike position is aligned with the other two scans.

As it was previously mentioned, the strategy that will be used, in this section, to align the scans is to overlap the centres of the scans. The centre of the scans will be considered to be the centroid of the segment where the TU is inserted. The centroids can be calculated by the application of the Equations 5.1, 5.2 and 5.3 presented in the "First Identification Method" sub-section.

To overlap the centroids, a rotation matrix, R, Equation 5.7, will be used and multiplied by the *organised vertices matrix*. As described in the last section, to define a rotation matrix it is necessary to define first the rotation angle and rotation axis.

To calculate the rotation angle, two linear equations are computed, each one connecting the centroid and the TU of each segment (only the XY-coordinates are taken into consideration), the rotation angle,  $\gamma$ , will be the angle formed by the two equations, Figure 4.11:

$$y = m_1x + b_1 \quad [4.10]$$

$$y = m_2x + b_2 \quad [4.11]$$

$$\gamma = \tan^{-1} \left( \frac{m_1 - m_2}{1 + m_1m_2} \right) \quad [4.12]$$

Where  $m_1$  and  $m_2$  are the slopes of each equation.

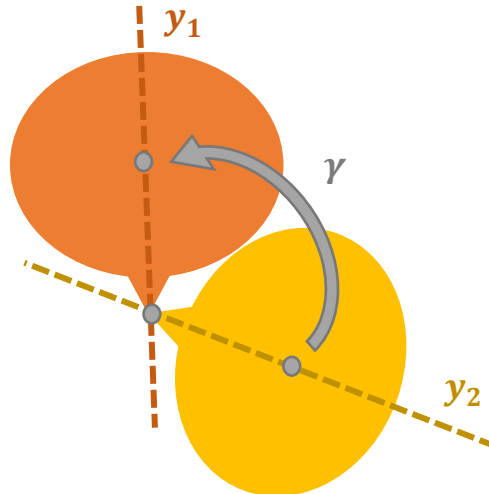


Figure 4.11: Schematic of the rotation angle,  $\gamma$ .

Since the goal is to align the scans, the rotation will be around the tibia markers, so the rotation vector,  $\vec{v}$ , will have its tail in TD and its head in TU.

After calculating the rotation matrix, the matrix is multiplied by the *organised vertices matrix* of the heel off position scan. The same procedure is applied to the heel strike position scan, finalising the alignment stage. With the conclusion of this stage, the scans are in the optimal position to be segmented, by a transverse plane, to better understand the variation in geometry, of the chosen lower limb muscles, and achieve the ultimate goal of this project.

#### 4.1.6 Segmentation of the lower limb

With all the scans aligned, there is only one last stage required to complete the project, which consists on transversely segment the scans on the most preeminent part of the tibialis anterior, the lateral gastrocnemius and the medial gastrocnemius muscles, in the different gait cycle positions. As referred previously, these areas are marked by the EMG markers, so this section aims to identify which marker corresponds to which muscles and segment the scan in between each pair of EMG markers.

To associate each marker to its respective muscle, the same technique presented in the “Tibia’s markers identification and respective plane calculation” sub-section, in the “

The markers’ identification efficiency could be improved with an improvement of the quality of the scans and also with all the scans being in the same position, preferably aligned with the z-axis.

Alignment of the scans” chapter was used. The distance in the XY-plane between the first identified marker, which corresponds to the TD marker, and all the other markers is calculated, and the results ordered in an ascending order.

In a new matrix, the *organised markers’ matrix*, the coordinates of the four markers with the lowest distances are registered, being the first three the tibia’s markers, TD, TM and TU, and the last one an EMG marker. Since the tibialis anterior, between the three muscles that are being accessed, is the closest muscle to the tibia, the 4<sup>th</sup> identified marker must be a tibialis anterior marker, TiD or TiU.

With the last marker registered, the same method is applied, the distance between the 4<sup>th</sup> registered marker and all the other markers is calculated. The two markers with the lowest distance are registered in the new organised matrix. The markers with the smallest distance, the 5<sup>th</sup> marker in the *organised markers matrix*, is the other tibialis anterior marker. Since the lateral gastrocnemius is closest to the

tibialis anterior muscle then the medial gastrocnemius, the 6<sup>th</sup> marker must be one of the lateral gastrocnemius markers.

The procedure described in the paragraph above is performed once again to find the other lateral gastrocnemius' marker, once found, is registered in the new matrix. The two markers that are missing from the *organised markers' matrix* are registered and assumed to be the medial gastrocnemius' pair of EMG markers.

With the EMG markers organised in pairs, the last task is to calculate the mean of the z-coordinates of each pair, which will be used to define the final segments of interest.

Since the goal of this project is to study the lower limb muscles, when their activity is at the highest peak, the final leg's segments, will correspond to the segments with the z-coordinate equal to the pair of the EMG markers of leg's position where the muscles have their highest activity. In the case of the tibialis anterior, the heel strike position and in the case of both gastrocnemii, the heel off position. The segments will be formed with all the points that have the chosen z-coordinate 0.25 u.m above or below the calculated z-coordinate mean.

### ***Efficiency analysis***

From all the scans' combination, meaning the alignment of the scans in the mid stance, heel strike and heel off positions, only one combination was not correctly aligned. This misalignment was due to one of the scans being in an oblique direction, and for that reason one of the tibia markers was miss identified leading to a miss calculation of the tibia plane, which influenced all the following rotations.

Another aspect needed to be referred is, although the scans were rescaled, so they would have all the same dimensions, step described in the "Alignment of the tibia markers" chapter, in the majority of the cases there was still a disproportion between the segment's size. This disproportion may be associated to the scanner's associated error, which increases with the subject's motion (the subject cannot maintain the same position through all the scanning time, there is always some small movements). This change in dimensions may limit the analysis of the segments (Figure 4.12 example a)).

Besides the disproportions of the scans, the markers did not remain in the same position through all the three scans, which can be associated to the muscle's movement and to the scan's associated error. This changes in position by the markers resulted in most of the segments having parts of the markers, limiting the possible assessment, and therefore conclusions, of the study.

Also, the scans were aligned with each other, which leads to a misalignment with the z-axis. This misalignment may also influence the final geometry of the scans and therefore, the end results (Figure 4.12 example b), c) and d)).

Although there was a disproportion of the scans, a shift in the markers' position and a misalignment of the scans with the z-axis, it was possible to understand, from visual assessment only, that the significant muscle deformations of both gastrocnemii are in the muscles' limits, and not on the most prominent part of the muscles (where the EMG sensors should be placed). Also, from a mere visual evaluation, there were no significant deformations in the tibialis anterior muscle.

Therefore, the goal of the following step is to understand if these deformations are indeed deformations and, if they are originated by the changes of the gait cycle positions. Hence, the deformations must be quantified, for matters of comparison for this project, and to serve as reference point in future work.

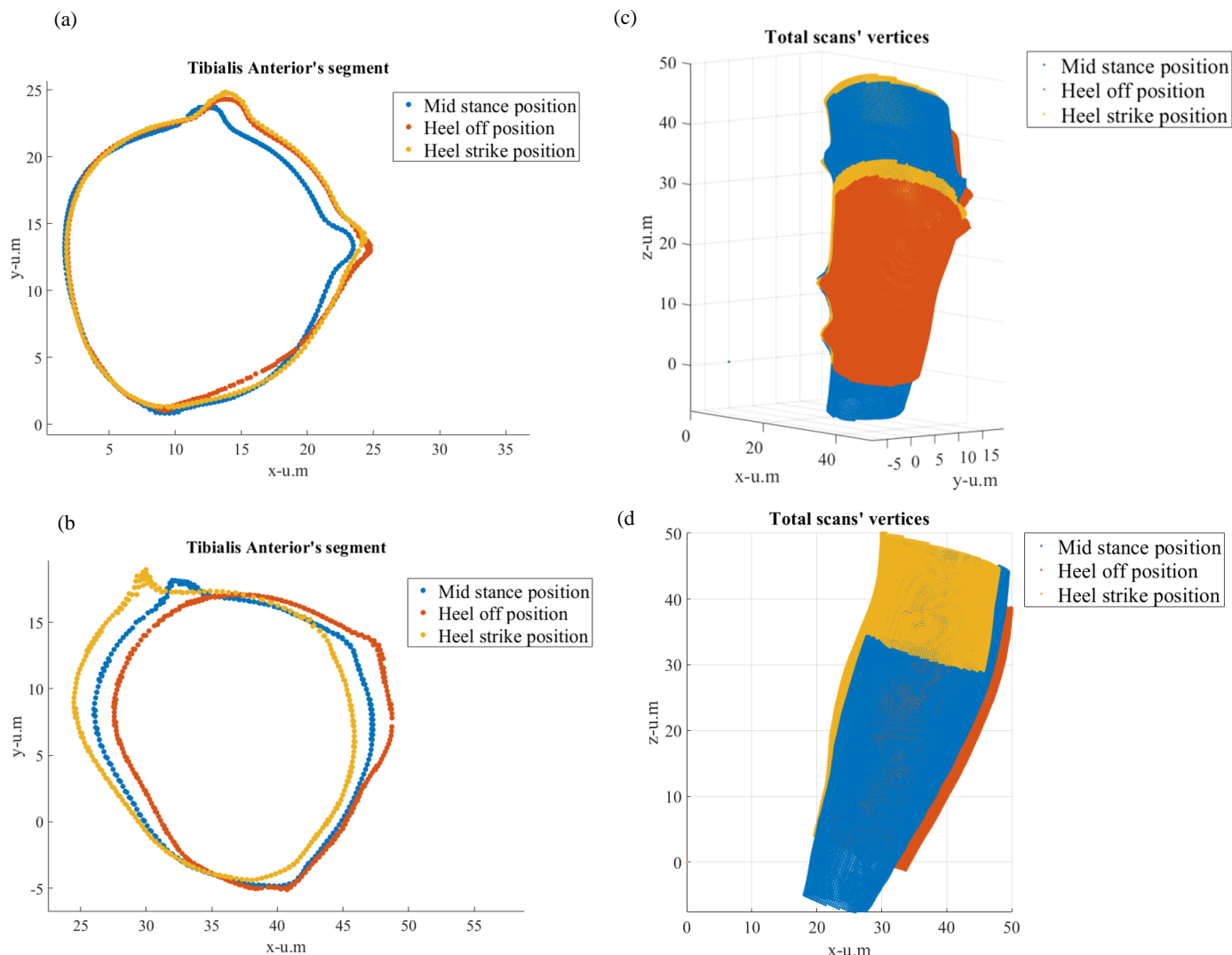


Figure 4.12: a) Example of the result of the disproportion between the scans of the same subject in the three different positions (segments from the scans of subject 1). b); c) and d) Example of the result of the misalignment of the scans with the z-axis (segments from the scans of subject 2).

### 4.1.7 Data Analysis

After identifying the markers, aligning the scans, and segmenting the leg scans in the regions of interest, the segments must be analysed. As referred in the previous subchapter, the segments were not proportional to each other, therefore the variation in geometry cannot be compared based on the segments' area variations. One alternative is to calculate the distance between the centroid of each segment and the respective vertices. The assessment would be based on the variation of these distances.

To calculate the centroids of each segment and from there the distance between the centroid and the respective vertices, the same algorithm used in the "First Identification Method" subchapter was applied. Every set of distances will be treated as a function, *distances' function*, where the independent variable corresponds to the number of samples corresponding to each vertex, and the dependent variable the distances. To calculate the variation of this function, the rate of change,  $T$ , is calculated for every sample in respect to the next sample based on the following equation, Equation. 4.13:

$$T = \frac{f(a) - f(b)}{a - b} \quad [4.13]$$

Where  $T$  is the rate of change of the  $f(x)$ , in this case the *distances' function*, with respect to the interval  $[a, b]$ , where  $a$  is one vertex and  $b$  the vertex that follows. The conjugation of every rate of change is the equivalent of calculating the 1<sup>st</sup> derivative of the *distances' function*.

From the 1<sup>st</sup> derivative of the function, it is possible to calculate the maximums and minimums of the *distances' function*, since they correspond to the zeros of the 1<sup>st</sup> derivative function.

Furthermore, if the same principle used for the *distances' function* is used for the 1<sup>st</sup> derivative function, (the calculation of the rate of change of the 1<sup>st</sup> derivative function) the 2<sup>nd</sup> derivative function is achieved, where the zeros of this new function, correspond to the changes in concavity of the *distances' function*.

In theory, if the maximums, minimums and changes in concavity of the *distance's function* are known, then if there is a change in a muscle's geometry for example a depression or a bump, there will be a change either in the signal of the 1<sup>st</sup> derivative function, either in the signal of 2<sup>nd</sup> derivative function, leading to a zero in, at least, one of the functions. In conclusion, the zeros from the 1<sup>st</sup> and 2<sup>nd</sup> derivative function will correspond to potential deformation locations (Figure 4.13).

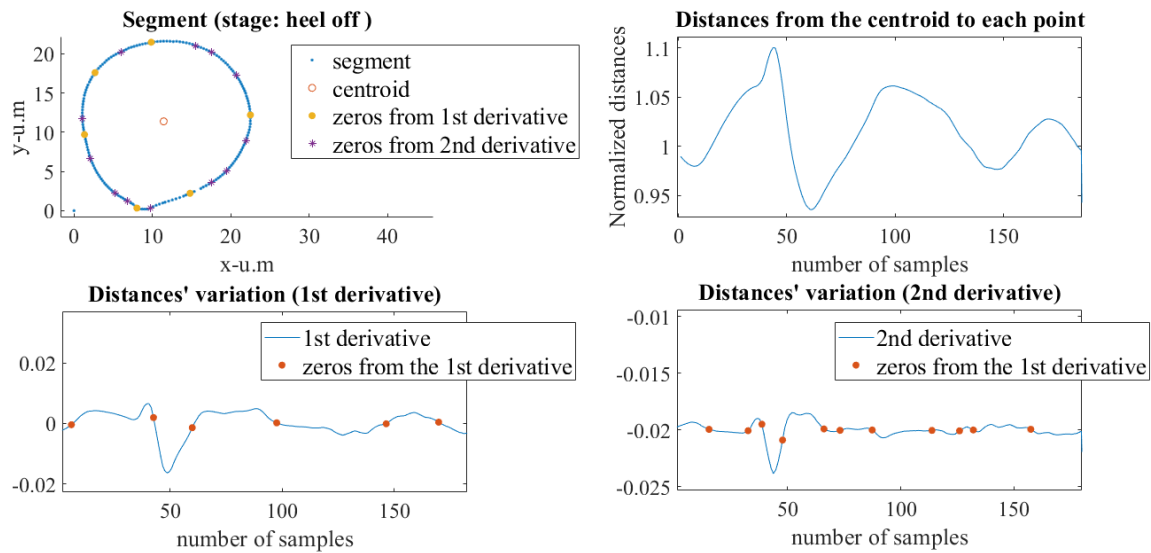


Figure 4.13: Schematics of the algorithm used to identify potential deformation locations (scan from subject 1)

After marking the potential locations where the potential variations may occur, it is required to find a measurement unit to allow the comparison of the scan's deformations between the three different gait cycle phases. The chosen measurement unit was the radius of curvature. For purposes of simplicity, the radius of curvature was computed by the application of the following function: *fit\_circle\_through\_3\_points* [77]. In this function, developed by Danylo Malyuta, from three points, the radius of a circle can be computed. Therefore, to calculate the radius of curvature, besides the marked locations, two other points must be selected. The other two points will be the points corresponding to 5 vertices before and after the marked spots.

Due to time containments, instead of writing an algorithm that would compare all the marked locations in each segment with the corresponding locations in the other two segments, of the other two gait cycle phases, the locations were chosen by hand. Some of the selected points corresponded to zeros of the first derivative, others to zeros from the second derivative, and others chosen without any identified zeros. The locations that were analysed are signaled in Figure 4.14. Also, the radius of curvature of the tibia in each segment was measured to serve as a reference value.

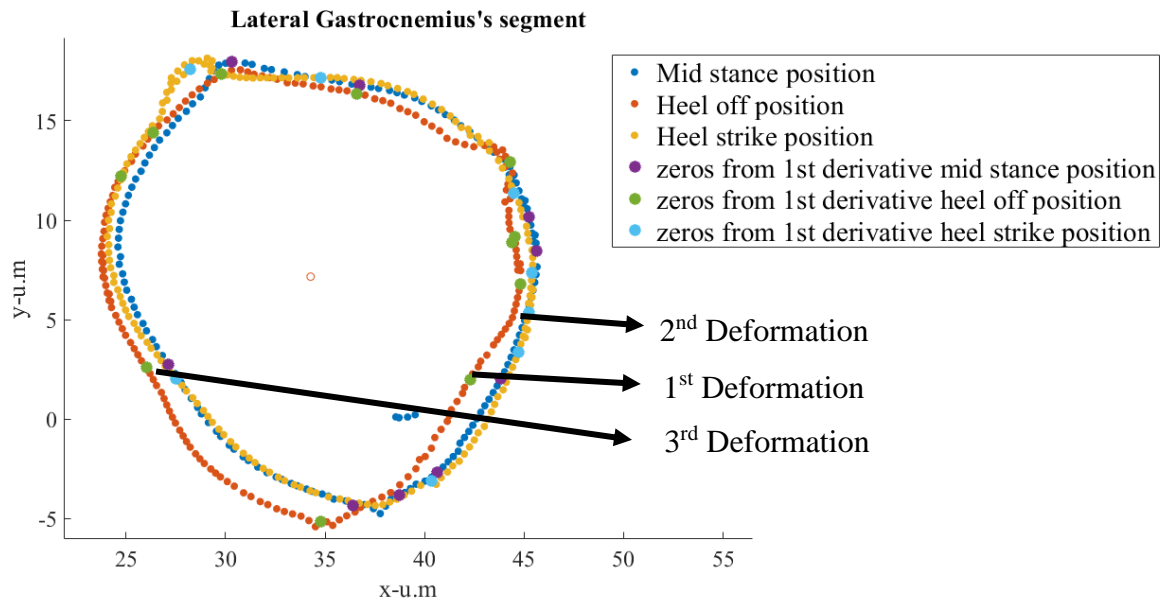


Figure 4.14: Example of the deformations that are going to be analysed (segments from the scans of subject 2)

To confirm the existence of significant differences between the marked spots in the different segments, a statistical analysis, more precisely a Kruskal-Wallis test, will be performed. The populations will be separated according to the gait cycle phases.

## 4.2 Results

As previously referred, five subjects participated on this experiment, however only four from the five set of scans were analysed, since the scans from the last subject were not properly aligned with each other.

The first step, required to analyse the segments, was to calculate the zeros from the 1<sup>st</sup> and 2<sup>nd</sup> derivative of the *distances' function*, and associate the zeros to the respective vertices of the segments. Some of the results, from this stage, are shown in Figure 4.15 and Figure 4.16.

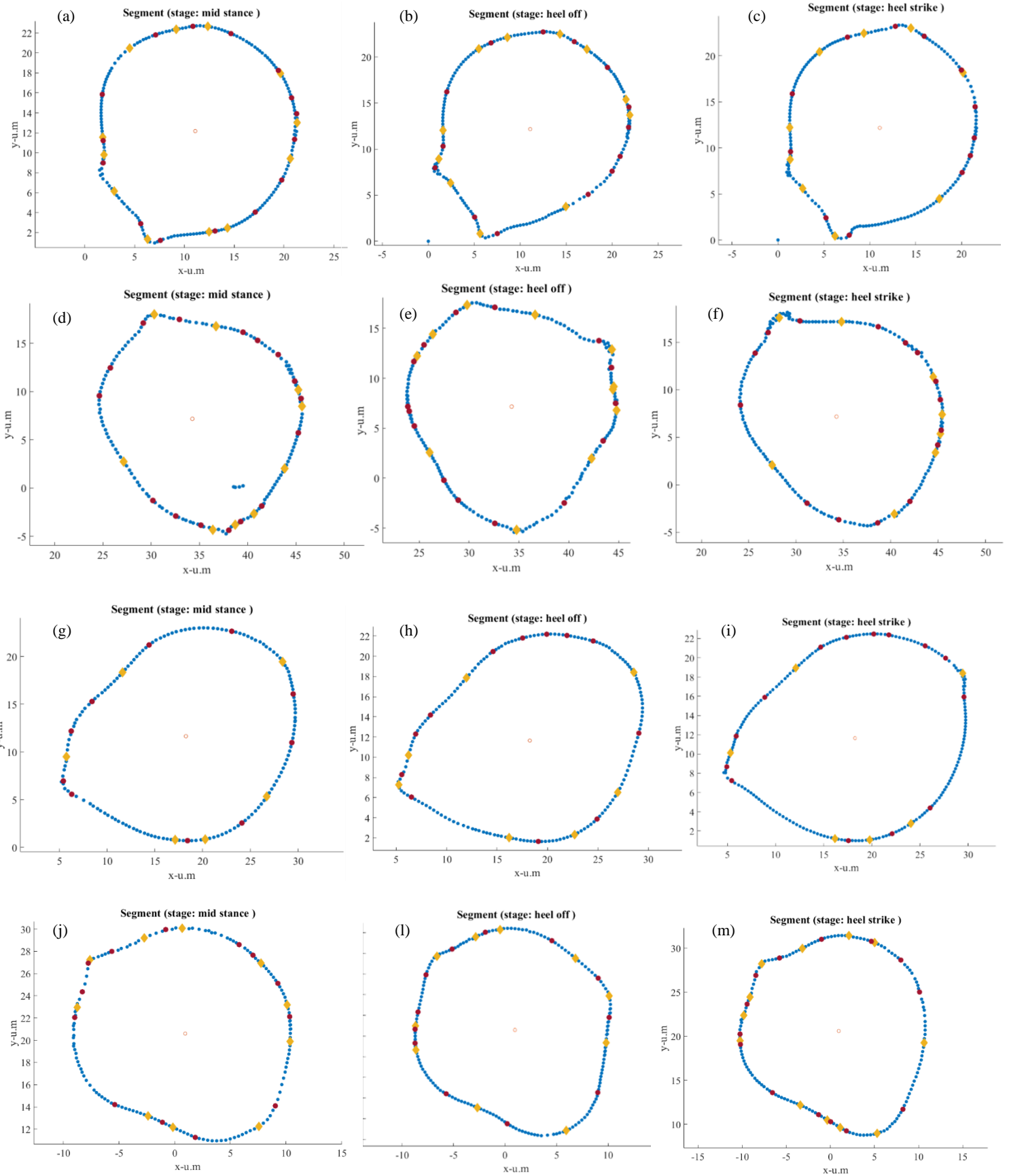


Figure 4.15: Segments at the lateral gastrocnemius markers' height from the different gait cycle phases. The yellow dots correspond to the zeros of the 1<sup>st</sup> derivative function and the red ones to the zeros of the 2<sup>nd</sup> derivative function. a); b) and c) segments from the scans of subject 1. d); e) and f) segments from the scans of subject 2. g); h) and i) segments from the scans of subject 3. j); l) and m) segments from the scans of subject 4.

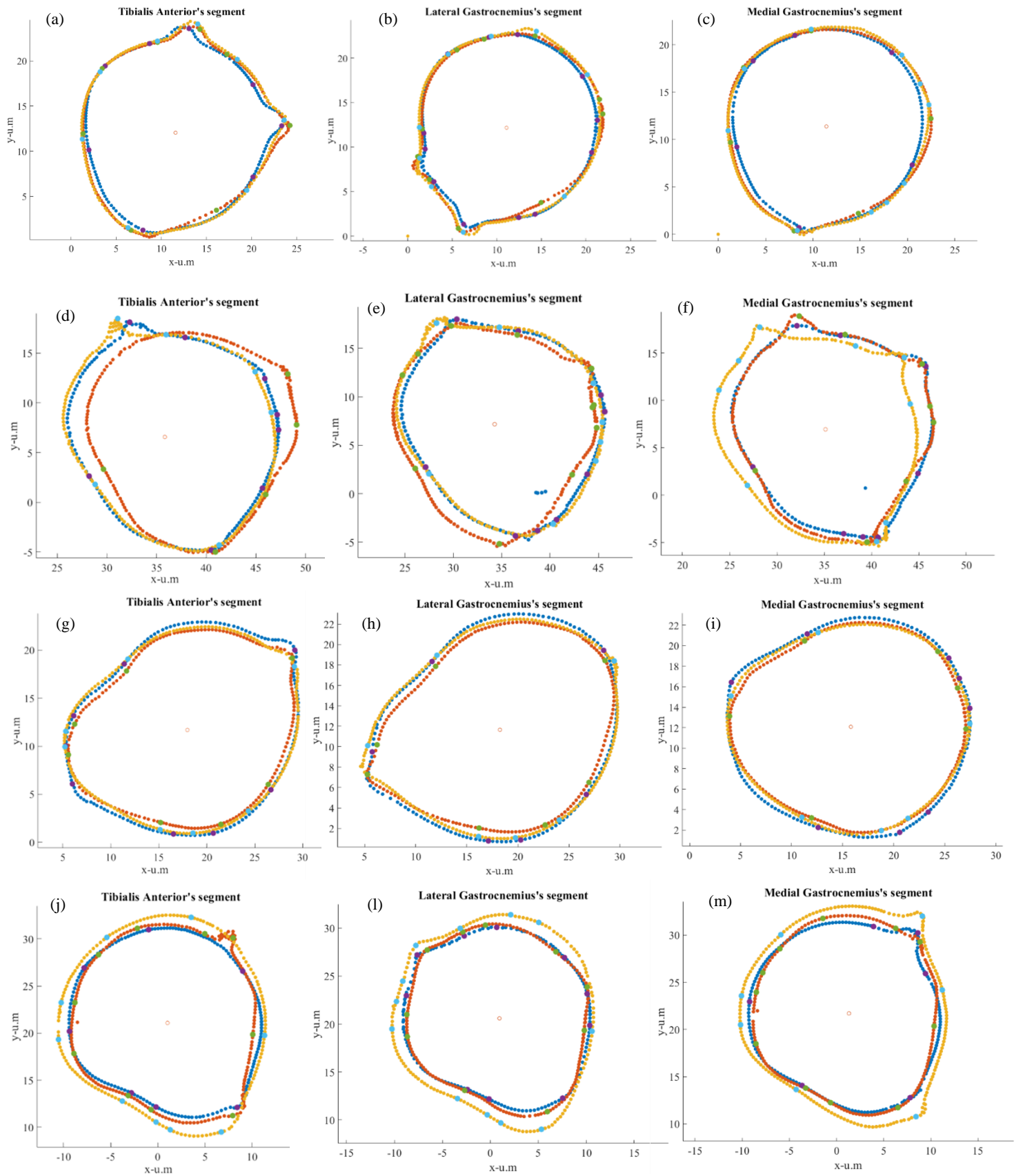


Figure 4.16: Segments at the three markers' height from the three different gait cycle phases ( the blue segments corresponds to the mid stance phase, the orange segments to the heel off position and the yellow ones to the heel strike position). The blue dots correspond to the zeros from the 1<sup>st</sup> derivative of the heel strike position distances' function, the greens to the zeros from the 1<sup>st</sup> derivative of the heel off position distances' function and the purples to the zeros from the 1<sup>st</sup> derivative of the mid stance position distances' function (the segments were aligned by the respective centroids). a); b) and c) segments from the scans of subject 1. d); e) and f) segments from the scans of subject 2. g); h) and i) segments from the scans of subject 3. j); l) and m) segments from the scans of subject 4

Table 4.1 Radius of curvature of the location where the three chosen deformation were. For every segment, the p-value from the Kruskal-Wallis test is presented. For every subject nine segments were analysed, three for each gait cycle position, and three for each marker. The results in this table are colored according to their value in comparison to all the other values in the table. The colour red corresponds to the lowest values and the colour green to the highest values.

Markers	1st Deformation			2nd Deformation			3rd Deformation			Tibia			
	M.S position	H. O position	H.S position	p-value	M.S position	H. O position	H.S position	p-value	M.S position	H. O position	H.S position	p-value	
Subject 1	Ti	12.13	37.56	13.29		11.40	11.04	8.11		x	x	x	
	LG	8.28	83.89	10.00	0.06	10.84	7.95	11.65	0.39	x	x	x	x
	MG	10.74	29.24	10.99		11.62	9.28	9.20		x	x	x	
Subject 2	Ti	21.07	14.22	27.87		8.60	5.14	17.43		416.40	68.29	1551.50	
	LG	14.44	13.86	19.99	0.25	8.48	4.54	11.11	0.04	67.74	25.50	56.40	0.29
	MG	20.52	25.75	260.38		11.60	4.28	19.94		64.20	32.35	92.70	
Subject 3	Ti	74.95	28.00	93.77		13.22	7.69	9.98		40.71	19.33	254.59	
	LG	25.75	13.52	23.68	0.96	11.96	11.85	9.50	0.30	45.58	71.21	46.55	0.96
	MG	19.64	64.11	17.07		8.90	7.51	7.47		73.89	237.52	14.31	
Subject 4	Ti	10.50	43.01	16.65		14.76	4.69	16.64		18.48	10.18	30.78	
	LG	11.44	33.75	17.85	0.03	7.23	3.40	17.85	0.04	21.27	10.20	37.47	0.03
	MG	11.60	473.27	11.95		9.69	5.05	12.01		23.59	16.39	32.11	

EJ

With the function's zeros calculated, the radius of curvature of each deformation was computed. The results are presented in Table 4.1.

For each subject's leg deformation, a Kruskal-Wallis test was applied to understand if the values obtained would significantly differ from population to population. The populations were defined based on the gait cycle positions (M.S – mid stance; H.O – heel off; H.S – heel strike), and the goal was to understand if there were significant differences between the radius of curvature, in the different gait cycle positions, for the prespecified locations. The results of the statistical tests (the p-values) are also presented in Table 4.1.

From the p-value results, it is possible to understand that in half of the cases, the radius of curvature does not significantly differ from position to position. However, this information also implies that in the other half of the results, at least in one of the locations, the radius of curvature significantly differs from the same location in another segment of a different gait cycle position (at a level of significance of 10%).

Therefore, for the results that presented a p-value inferior to 0.1 a multiple comparisons test must be performed to understand which gait cycle position's locations have radius of curvature that significantly differ from each other. The results are presented in Table 4.2

Table 4.2: Results from the multiple comparison test (at a level of significant of 10%). The values in green represent the populations that present values significantly different from each other, the values in orange represent the opposite.

	MS-HO positions	MS-HS positions	HS-HO positions	MS-HO positions	MS-HS positions	HS-HO positions	MS-HO positions	MS-HS positions	HS-HO positions
Subject 1	True	False	False	-	-	-	-	-	-
Subject 2	-	-	-	False	False	True	-	-	-
Subject 3	-	-	-	-	-	-	-	-	-
Subject 4	True	False	False	False	False	True	False	False	True

With the information acquired from Table 4.2, one may conclude that all the values, from the different gait cycle positions, that significantly differ from each other, always corresponded to values from the heel off position regarding one of the other two gait cycle positions (at a level of significance of 10%). This was the expected result since the chosen deformations are associated to the gastrocnemii muscles and their highest activity moment corresponds to the heel off phase, therefore the radius of curvature should change.

Also, when comparing the values from the mid stance position with the heel strike position no significant differences were found, which was also expected from the outcome of the statistical tests.

Furthermore, it is important to mention that one of the subjects (subject 3) did not present any pattern regarding the changes in the radius of curvature due to the changes of the gait cycle positions. In opposition, subject 4 presented a clear changing pattern regarding the radius of curvature values in every deformation.

Regarding the radius of curvature of the tibia, in exception to subject 2, the collected values did not significantly differ from position to position, which was the expected outcome. In the case of subject

2, the difference in the radius of curvature may be associated to the choice of the tibia's location not corresponding to the actual tibia location.

Analysing the actual values of the radius of curvature, one may conclude that it is expected, when both gastrocnemius contract concentrically, which corresponds to the heel off position moment, to increase in the location of the 1<sup>st</sup> deformation, to decrease in the location of the second, and decrease as well in the location of the 3<sup>rd</sup> deformation, although it is not as clear, in this location, the expected behaviour. Note that the first and second deformations are associated with the lateral gastrocnemius activity and the third deformation to the medial gastrocnemius activity.

The previous information, in combination with the statistical analysis, corroborates the hypothesis of existing indeed geometry changes in the muscles' limits due to the changes of the gait cycle phases.

Regarding subject 1, it was not possible to collect data for the third deformation since it matched the first vertices of the segments, and for that reason, it was not possible to calculate the radius of curvature with 5 vertices separating each point. In the tibia's case, no values were collected due to a lack of clarity regarding the tibia's location.

### **4.3 Conclusion**

In this experiment, an algorithm to study different scans from the same leg, in different gait cycle positions, was developed. This algorithm was configured to help the understanding of the lower limb muscles' deformation, with the final goal of using its output to design an efficient exoskeleton's cuff.

The results obtained with this algorithm revealed the possibility, with a certain amount of development, for it to become a potential tool, capable of bringing useful information for the orthosis development. But first, some adjustment must be done to improve the algorithm's output.

Firstly, one of the goals, when the algorithm was developed, was to study the deformation of the muscles where the EMG sensors should be placed, to help designing an interface that would guarantee a constant contact between the sensors and the user's skin.

By a visual assessment of the segments, the most relevant deformations of both gastrocnemii were not where the EMG sensors should be placed (the most prominent part of the muscles), but in the muscles' limits, also it appears that there were no relevant deformations in the tibialis anterior region.

Although it was not possible to test the presented hypothesis, it was concluded, from the algorithm's outputs, that there were indeed geometry variations on the muscle's limits. The locations where the sensors should be placed were not accessed due to the existence of markers in the segments, limiting the assessment areas. Therefore, in future work, two sets of scans should be performed: one set in the same conditions the scans from this experiment were taken, and another set only with the tibia markers. The existence of the two sets of scans would guarantee the evaluation of the hole segment, keeping the information of the ideal sensor's location.

Another problem, in this study, was the disproportion of the scans with respect to each other. One plausible reason for this disproportion may be the scanner's associated error. One solution to rectify this disproportion is to use cameras from the Vicon Motion Systems' company, tracking the markers, while the subject's lower limb is scanned (the markers used in this study are the markers used by the Vicon Motion Systems). The combination of the two systems' outputs could potentially decrease the associated error.

Another detail, that should be fixed in future work, is the alignment of the scans with the z-axis.

Lastly, regarding the data analysis, the goal would be to define the possible deformation locations, by the calculation of the zeros of the 1<sup>st</sup> and 2<sup>nd</sup> derivative of the *distances' function*, and from the function's output, compare the marked locations with their homonymous in the other two scans, instead of doing it by hand and selecting only a few specific locations. So, in future work, this improvement could be developed.

Also, another possibility, to analyse the scans deformations, is to calculate the radius of curvature in between the spots marked by the 1<sup>st</sup> and 2<sup>nd</sup> derivative of the *distances' function*. This change would provide a new set of information, for example, it would provide the possibility to calculate the radius of curvature of the 2<sup>nd</sup> deformation, without having to choose the location by hand.

Besides changing the assessment locations, the method used to calculate the radius of curvature could also be altered. One possibility would be to approximate each segment, defined by two zeros from the derivative functions, to a parametrically function, and from there, calculate the radius of curvature by the application of the respective formula. The results with this new calculation method would probably be more reliable, and every point of the segment would have a known radius of curvature, creating a new function: the *radius of curvature function*.

In addition, all the segments could be analysed, not only the three segments defined by the markers. By analysing all the segments and calculating the *radius of curvature function* for each segment, the exoskeleton's interface could be designed based on the functions' output. The areas where the radius of curvature remained constant, through the several segments, would correspond to the places where the rigid parts should be placed. The zones with higher changing rates of the radius of curvature would correspond to the places where more flexible parts should be placed to guarantee the constant contact of interfaces with the user.

The ultimate goal would be to scan the subject's lower limb, in the three positions, and from there have the algorithm designing the perfect cuff, with the sensors already in place, in the most suited locations, ready to be 3D printed.

In conclusion, in spite of all the changes that could be done to improve the algorithm, it was able to detect possible locations where a deformation could appear, and with the help of the developer, measure the radius of curvature of that same locations, in order to understand if it varies with the variation of the gait cycle position. Also, with this algorithm, it was possible to prove that some of the geometrical variations happen indeed in the muscles' limits. With the formulated conclusions for the performance of this algorithm, one can assume that the answer to the following question: "Does the development of an algorithm, to study the deformation of the lower limb muscles, during the gait cycle, will help redesign the 3D printed exoskeleton's cuff?" is an affirmative one.

# Chapter 5

## CONCLUSION AND FUTURE WORK

In recapitulation, the goal of this project was to give an answer to three important questions: if it was possible to produce working EMG sensors; if it was possible to produce working force sensors; and, lastly, if the development of an algorithm, to study the deformation of the lower limb muscles, during the gait cycle, would help redesign the 3D printed exoskeleton's cuff, already developed by K. Langlois *et al.*

Starting with the EMG sensor, it was proven, in this project, that it is possible to 3D print a working EMG sensor by using an FDM, multi-material printing technique, more precisely, it was possible to fully print an EMG sensor using only two types of 3D printing filaments, a semi-conductive and a non-conductive filament. Although the developed sensor registered EMG signals, in future work, some tests are going to be required to fully comprehend what is to expect from the sensor's output, if it can be used to predict, in real-time, the subject's intentions and what are the sensor's limitations.

Furthermore, it was also proven that changing the design of the sensor from two thick, smaller transducers, transversely parallel to each other and isolated by a non-conductive material, to two thinner and larger transducers, also isolated by a flexible, non-conductive material, but instead of being transversely parallel, being on top of each other, a capacitance-based force sensor can also be achieved. Note that the two sensors were printed with different materials, so, in future work, it would be interesting to develop and test the EMG sensor with the force sensor's materials, since the inverse is not suitable for the purpose of this project.

Also, regarding the materials' choice, in future work, one may think of incorporate self-healing materials, instead of TPU materials, into the exoskeletons' interfaces. This type of materials are just now taking their first steps in the research world, and as the name implies, are materials that can recover completely from macroscopic damage, like cuts, scratches and ruptures, plus they are being developed to be 3D printed by FDM printers [78], [79]. Therefore, it would be interesting to test them as materials of the exoskeletons' interfaces.

To test the 3D printed force sensor, it was also required the development of a data acquisition system, which, although with some recommended improvements and changes of the circuitry elements, was an efficient one, able to properly read the changes in capacitance with the changes in the applied force.

Regarding the development of the 3D printed capacitance-based force sensor, it was not as straight forward as the development of the 3D printed EMG sensor. A study had to be conducted to understand which type of non-conductive flexible materials the force sensor's dielectric should be printed with, and with which type of printing settings. From all the evaluated materials (Ultimaker TPU 95A, REC RUBBER, silicon and NinjaFlex 85A) the material that originated the most flexible dielectric when an FDM, multi-material printing technique was used, was the NinjaFlex 85A, printed with a 50% concentric infill, in exception to the top and bottom layers that were defined as "Bottom layers", i.e., thicker layers printed with 100% infill.

As the EMG sensors, the 3D printed force sensor should go under an intensive study to understand how the sensor's output changes with the time use, load history and other environmental factors like temperature or humidity. Also, understand if the output of this type of sensors, in conjugation with the developed reading system, can be used to measure in real time the interaction forces between the exoskeleton's interface and the subject.

Regarding the algorithm developed to understand the changes in geometry of the lower limb muscles, it was able to detect the markers, which were signaling the tibia and the places where the EMG sensors should be placed, align the three scans and detect the possible locations where the deformations could appear. Also, with the help of the developer, it was able to measure the radius of curvature of that same locations and understand if it varies with the variation of the gait cycle position. In the end, with this algorithm, it was possible to prove that some of the geometrical variations happen indeed in the muscles' limits, which will certainly help the redesign the exoskeleton's cuff.

Although, the three questions, this project proposed to answer were respond, the main question, the one that started this scientific question, is still to answer (the question was: Is it possible to produce a 3D printed orthosis, embedded with 3D printed EMG and force sensors? And, will it improve the exoskeletons' performance?).

Therefore, in future work, an orthosis, embedded with EMG and force sensors, should be designed based on the information provided by the algorithm developed in this project. After designing the orthosis, it should be printed and tested to understand if it is a viable idea.

Furthermore, the sensors' output should be analysed to understand if it mirrors the user's intentions, in the case of the EMG sensors, and the interaction forces, in the case of the capacitance-based sensors. If indeed the sensors' output are tuned with the actual physical phenomenons, they should be incorporated into the exoskeletons' control and comprehend if they truly improve the exoskeleton's performance.

# Chapter 6

## BIBLIOGRAPHY

- [1] A. J. Young and D. P. Ferris, "State of the art and future directions for lower limb robotic exoskeletons," *IEEE Trans. Neural Syst. Rehabil. Eng.*, vol. 25, no. 2, pp. 171–182, 2017.
- [2] Y. Ni, R. Ji, K. Long, T. Bu, K. Chen, and S. Zhuang, "A review of 3D-printed sensors," *Appl. Spectrosc. Rev.*, vol. 52, no. 7, pp. 623–652, 2017.
- [3] H. Kawamoto and Y. Sankai, "Power assist method based on Phase Sequence and muscle force condition for HAL," *Adv. Robot.*, vol. 19, no. 7, pp. 717–734, 2005.
- [4] A. T. Asbeck, S. M. M. De Rossi, K. G. Holt, and C. J. Walsh, "A biologically inspired soft exosuit for walking assistance," *Int. J. Rob. Res.*, vol. Vol. 34, no. 6, pp. 744–762, 2015.
- [5] "EksoVest - Exoskeleton Shoulder Support for Overhead Work | Ekso Bionics", Ekso Bionics, 2020. [Online]. Available: <https://eksobionics.com/eksoworks/eksovest/>. [Accessed: 10- Jan- 2020]
- [6] "ReWalk™ Personal 6.0 - ReWalk – More Than Walking", ReWalk – More Than Walking, 2020. [Online]. Available: <https://rewalk.com/rewalk-personal-3/>. [Accessed: 10- Jan- 2020]
- [7] R. R. Fabrizio Margheritini, *Orthopedic Sports Medicine*, vol. 53, no. 9. 2013.
- [8] M. Mulas, Mi. Folgheraiter, and G. Gini, "An EMG-controlled Exoskeleton for hand rehabilitation," *Proc. 2005 IEEE, 9th Int. Conf. Rehabil. Robot.*
- [9] W. Meng, Q. Liu, Z. Zhou, Q. Ai, B. Sheng, and S. S. Xie, "Recent development of mechanisms and control strategies for robot-assisted lower limb rehabilitation," *Mechatronics*, vol. 31, pp. 132–145, 2015.
- [10] I. Díaz, J. J. Gil, and E. Sánchez, "Lower-Limb Robotic Rehabilitation: Literature Review and Challenges," *J. Robot.*, vol. 2011, no. i, pp. 1–11, 2011.
- [11] E. Akdoğan and M. A. Adli, "The design and control of a therapeutic exercise robot for lower limb rehabilitation: Physiotherobot," *Mechatronics*, vol. 21, no. 3, pp. 509–522, 2011.
- [12] "Lokomat®", Hocoma, 2020. [Online]. Available: <https://www.hocoma.com/solutions/lokomat/#intro>. [Accessed: 10- Jan- 2020]
- [13] K. Junius *et al.*, "Mechatronic design of a sit-to-stance exoskeleton," *5th IEEE RAS/EMBS Int. Conf. Biomed. Robot. Biomechatronics*, pp. 945–950, 2014.
- [14] K. Langlois, M. Moltedo, T. Bacek, C. Rodriguez-Guerrero, B. Vanderborght, and D. Lefebvre, "Design and Development of Customized Physical Interfaces to Reduce Relative Motion between the User and a Powered Ankle Foot Exoskeleton," *Proc. IEEE RAS EMBS Int. Conf. Biomed. Robot. Biomechatronics*, vol. 2018–August, pp. 1083–1088, 2018.
- [15] M. B. Yandell, B. T. Quinlivan, D. Popov, C. Walsh, and K. E. Zelik, "Physical interface dynamics alter how robotic exosuits augment human movement: implications for optimizing wearable assistive devices," *J. Neuroeng. Rehabil.*, vol. 14, no. 1, pp. 1–11, 2017.
- [16] A. Schiele, "Ergonomics of Exoskeletons: Objective Performance Metrics," *Third Jt. Eurohaptics Conf. Symp. Haptic Interfaces Virtual Environ. Teleoperator Syst.*, pp. 103–108.

- [17] J. L. Pons, *Wearable robotics: Biomechatronic Exoskeletons*. Chichester: Wiley, 2008.
- [18] A. Schiele, "An Explicit Model to Predict and Interpret Constraint Force Creation in pHRI with Exoskeletons," *2008 IEEE Int. Conf. Robot. Autom.*, pp. 1324–1330.
- [19] T. Kermavnar, V. Power, A. De Eyto, and L. O. Sullivan, "Computerized Cuff Pressure Algometry as Guidance for Circumferential Tissue Compression for Wearable Soft Robotic Applications: A Systematic Review," *SOFT Robot.*, vol. 5, no. 1, 2018.
- [20] S. M. M. de Rossi *et al.*, "Sensing pressure distribution on a lower-limb exoskeleton physical human-machine interface," *Sensors*, vol. 11, no. 1, pp. 207–227, 2011.
- [21] K. Kiguchi and Y. Hayashi, "An EMG-Based Control for an Upper-Limb," *IEEE Trans. Syst. Man, Cybern. Part B Cybern.*, vol. 42, no. 4, pp. 1064–1071, 2012.
- [22] Y. H. Yin, Y. J. Fan, and L. D. Xu, "{EMG} and {EPP}-integrated human-machine interface between the paralyzed and rehabilitation exoskeleton," *IEEE Trans. Inf. Technol. Biomed.*, vol. 16, no. 4, pp. 542–549, 2012.
- [23] N. S. K. Ho *et al.*, "An EMG-driven Exoskeleton Hand Robotic Training Device on Chronic Stroke Subjects," *Int. Conf. Rehabil. Robot.*, vol. 2011, 2011.
- [24] "HAL THERAPY", [Online]. Available: <https://www.cyberdyne.jp/english/services/HALTherapy.html> [Accessed: 10- Jan- 2020]
- [25] A. Chortos, J. Liu, and Z. Bao, "Pursuing prosthetic electronic skin," *Nat. Mater.*, vol. 15, no. 9, pp. 937–950, 2016.
- [26] X. Wang, L. Dong, H. Zhang, R. Yu, C. Pan, and Z. L. Wang, "Recent Progress in Electronic Skin," *Adv. Sci.*, vol. 2, no. 10, pp. 1–21, 2015.
- [27] A. P. Gerratt, H. O. Michaud, and S. P. Lacour, "Elastomeric electronic skin for prosthetic tactile sensation," *Adv. Funct. Mater.*, vol. 25, no. 15, pp. 2287–2295, 2015.
- [28] S. Yao and Y. Zhu, "Wearable multifunctional sensors using printed stretchable conductors made of silver nanowires," *R. Soc. Chem.*, 2014.
- [29] R. ( U. E. de I. Seeley, T. (Universidade E. de I. Stephens, and Tate Philip (Universidade Estatal de Ihado), "Anatomia e fisiologia - Seeley.pdf." 2005.
- [30] A. J. Vander, J. Sherman, and D. Luciano, "Human physiology." McGraw-Hill, Boston, 2001.
- [31] R. Merletti, *Electromyography: physiology, Engineering and noninvasive applications*. Piscataway, NJ, 2010.
- [32] F. Hardalaç and R. Canal, "EMG circuit design and AR analysis of EMG signs," *J. Med. Syst.*, vol. 28, no. 6, pp. 633–642, 2004.
- [33] S. Xing and X. Zhang, "EMG-driven computer game for post-stroke rehabilitation," *2010 IEEE Conf. Robot. Autom. Mechatronics, RAM 2010*, pp. 32–36, 2010.
- [34] C. J. De Luca, L. Donald Gilmore, M. Kuznetsov, and S. H. Roy, "Filtering the surface EMG signal: Movement artifact and baseline noise contamination," *J. Biomech.*, vol. 43, no. 8, pp. 1573–1579, 2010.
- [35] M. Asghari Oskoei and H. Hu, "Myoelectric control systems-A survey," *Biomed. Signal Process. Control*, vol. 2, no. 4, pp. 275–294, 2007.
- [36] J. Hussain, K. Sundaraj, I. D. Subramaniam, and C. K. Lam, "Analysis of fatigue in the three heads of the triceps brachii during isometric contractions at various effort levels," *J. Musculoskelet. Neuronal Interact.*, pp. 1–10, 2019.
- [37] J. D. E. Luca, M. Knaflitz, C. J. De, and L. Myoelectric, "Myoelectric manifestations of fatigue in voluntary and electrically elicited contractions," *Am. Physiol. Soc.*, pp. 1810–1820, 1990.
- [38] D. I. P. D. I. Elettronica, G. Balestrat, D. I. P. Di, and A. E. Informatica, "EFFECT OF FFT

- BASED ALGORITHMS ON ESTIMATION OF MYOELECTRIC SIGNAL SPECTRAL PARAMETERS ‘ I,” *IEEE Eng. Med. L Biol. SOCIETY 11TH Annu. Int. Conf.*, pp. 1–2, 1989.
- [39] A. Rainoldi, G. Galardi, L. Maderna, G. Comi, L. Lo Conte, and R. Merletti, “Repeatability of surface EMG variables during voluntary isometric contractions of the biceps brachii muscle,” *J. Electromyogr. Kinesiol.*, vol. 9, no. 2, pp. 105–119, 1999.
- [40] R. Merletti, “Comparison of algorithms for estimation of EMG variables during voluntary isometric contractions,” *J. Electromyogr. Kinesiol.*, vol. 10, pp. 337–349, 2000.
- [41] W. B. Ming Dong, Wang Xin, Xu Rui, Qiu Shuang, Zhao Xin, Qi Hongzhi, Zhou Peng, Zhang Lixin, “sEMG Feature Analysis on Forearm Muscle Fatigue During Isometric Contractions,” *Tianjin Univ. Springer-Verlag Berlin Heidelb.*, vol. 20, pp. 139–143, 2014.
- [42] M. Cifrek, V. Medved, S. Tonkovic, and S. Ostojic, “surface EMG based muscle fatigue evaluation in biomechanics.pdf.” Elsevier, pp. 327–340, 2009.
- [43] K. Ollivier, P. Portero, O. Mai, and J. Hogrel, “Repeatability of surface EMG parameters at various isometric contraction levels and during fatigue using bipolar and Laplacian electrode configurations,” vol. 15, pp. 466–473, 2005.
- [44] G. Wolterink, R. Sanders, and G. Krijnen, “3D-Printing of soft sEMG sensing structures,” *IEEE*, pp. 1–2, 2017.
- [45] B. Lautrup, *Physics of continuous matter, Second edition*. Hoboken: CRC Press, 2011.
- [46] C. K. Alexander and M. N. O. Sadiku, *Basic Laws, Ohm’s Law*. 2001.
- [47] M. Schouten, R. Sanders, and G. Krijnen, “3D printed flexible capacitive force sensor with a simple micro-controller based readout,” *Proc. IEEE Sensors*, vol. 2017–Decem, no. 3, pp. 1–3, 2017.
- [48] S. J. Leigh, R. J. Bradley, C. P. Purssell, D. R. Billson, and D. A. Hutchins, “A Simple, Low-Cost Conductive Composite Material for 3D Printing of Electronic Sensors,” *PLoS One*, vol. 7, no. 11, pp. 1–6, 2012.
- [49] G. Zhu *et al.*, “Self-powered, ultrasensitive, flexible tactile sensors based on contact electrification,” *Nano Lett.*, vol. 14, no. 6, pp. 3208–3213, 2014.
- [50] A. Dijkshoorn *et al.*, “Embedded sensing: Integrating sensors in 3-D printed structures,” *J. Sensors Sens. Syst.*, vol. 7, no. 1, pp. 169–181, 2018.
- [51] T. Duong *et al.*, “Comparative Study of Functional Grasp and Efficiency between a 3D-Printed and Commercial Myoelectric Transradial Prosthesis Using Able-Bodied Subjects: A Pilot Study,” *J. Prosthetics Orthot.*, vol. 29, no. 3, pp. 112–118, 2017.
- [52] S. M. Peltola, F. P. W. Melchels, D. W. Grijpma, and M. Kellomäki, “A review of rapid prototyping techniques for tissue engineering purposes,” *Ann. Med.*, vol. 40, no. 4, pp. 268–280, 2008.
- [53] P. Laszczak, L. Jiang, D. L. Bader, D. Moser, and S. Zahedi, “Development and validation of a 3D-printed interfacial stress sensor for prosthetic applications,” *Med. Eng. Phys.*, vol. 37, no. 1, pp. 132–137, 2015.
- [54] B. Shih, J. Mayeda, Z. Huo, C. Christianson, and M. T. Tolley, “3D Printed Resistive Soft Sensors,” *IEEE Int. Conf. Soft Robot.*, 2018.
- [55] S. Harada, K. Kanao, Y. Yamamoto, T. Arie, S. Akita, and K. Takei, “Fully printed flexible fingerprint-like three-axis tactile and slip force and temperature sensors for artificial skin,” *ACS Nano*, vol. 8, no. 12, pp. 12851–12857, 2014.
- [56] E. Pritchard, M. Mahfouz, B. Evans, S. Eliza, and M. Haider, “Flexible capacitive sensors for high resolution pressure measurement,” *Proc. IEEE Sensors*, pp. 1484–1487, 2008.
- [57] H. Zhang, M. Y. Wang, J. Li, and J. Zhu, “A soft compressive sensor using dielectric

- elastomers,” *Smart Mater. Struct.*, vol. 25, no. 3, p. 0, 2016.
- [58] M. W. Whittle, H. Court, and J. Hill, “Gait Analysis : An Introduction.”
- [59] J. C. O’Connor, C. L. Vaughan, and B. L. Davis, *Dynamics of human gait*. Cape Town, South Africa: Kiboho Publishers, 1999.
- [60] A. T. Asbeck, S. M. M. De Rossi, K. G. Holt, and C. J. Walsh, “A biologically inspired soft exosuit for walking assistance,” *Int. J. Rob. Res.*, vol. 34, no. 6, pp. 744–762, 2015.
- [61] A. T. Asbeck, R. J. Dyer, A. F. Larusson, and C. J. Walsh, “Biologically-inspired Soft Exosuit,” *2013 IEEE 13th Int. Conf. Rehabil. Robot.*, pp. 1–8, 2013.
- [62] "Improving quality of life through Human-Centered Robotics", 2020. [Online]. Available: <https://www.brubotics.eu/>. [Accessed: 15- May- 2020]
- [63] "Brussels Human Robotics Research Center", 2020. [Online]. Available: <https://www.brubotics.eu/research/renm>. [Accessed: 15- May- 2020]
- [64] T. Bacek *et al.*, “BioMot Exoskeleton - Towards a Smart Wearable Robot for Symbiotic Human-Robot Interaction,” pp. 1666–1671, 2017.
- [65] "Welcome to SENIAM", *Seniam.org*, 2020. [Online]. Available: <http://www.seniam.org/>. [Accessed: 15- Jan- 2020]
- [66] N. A. Dimitrova, T. I. Arabadzhiev, J. Y. Hogrel, and G. V. Dimitrov, “Fatigue analysis of interference EMG signals obtained from biceps brachii during isometric voluntary contraction at various force levels,” *Journal of Electromyography and Kinesiology*, vol. 19, no. 2. pp. 252–258, 2009.
- [67] *Instructables.com*, 2020. [Online]. Available: <https://www.instructables.com/id/Capacitance-meter-with-arduino-and-741-op-amp/>. [Accessed: 18- Nov- 2019]
- [68] D. Information, “LMx24-N , LM2902-N Low-Power , Quad-Operational Amplifiers,” 2015.
- [69] H. J. Qi and M. C. Boyce, “Stress-strain behavior of thermoplastic polyurethanes,” *Mech. Mater.*, vol. 37, no. 8, pp. 817–839, 2005.
- [70] D. S. Tpu *et al.*, “Technical data sheet TPU 95A,” pp. 1–3.
- [71] “NinjaFlex ® 3D Printing Filament Flexible Polyurethane Material for FDM Printers,” p. 8254.
- [72] "REC - safe 3D printer filaments", *Rec3d.ru*, 2020. [Online]. Available: <https://rec3d.ru/en/>. [Accessed: 10- Dec- 2019]
- [73] " Roger Meier's Freeware" 2020. [Online]. Available: <https://freeware.the-meiers.org/>. [Accessed: 13- Dec- 2019]
- [74] L. Tan and J. Jiang, *Digital Signal Processing*. Elsevier, 2008.
- [75] "stlread", *Nl.mathworks.com*, 2020. [Online]. Available: <https://nl.mathworks.com/matlabcentral/fileexchange/6678-stlread>. [Accessed: 14- May- 2019]
- [76] "Ellipse Fit (Direct method)", *Nl.mathworks.com*, 2020. [Online]. Available: <https://nl.mathworks.com/matlabcentral/fileexchange/22684-ellipse-fit-direct-method>. [Accessed: 03- Jun- 2019]
- [77] "Fit circle through 3 points", *Nl.mathworks.com*, 2020. [Online]. Available: <https://nl.mathworks.com/matlabcentral/fileexchange/57668-fit-circle-through-3-points>. [Accessed: 06- Jan- 2020]
- [78] E. Roels, S. Terryn, J. Brancart, R. Verhelle, G. Van Assche, and B. Vanderborght, “Additive manufacturing for self-healing soft robots,” *ResearchGate*, 2020.
- [79] A. Bonds, “Self-Healing and High Interfacial Strength in Multi- Material Soft Pneumatic Robots via Reversible Diels – Alder Bonds,” *Actuators*, vol. 9, no. 34, pp. 1–17, 2020.